UNIVERSITÄT BONN

Dissertation
zur Erlangung des Grades
Doktorin der Agrarwissenschaften (Dr. Agr.)
der Agrar-, Ernährungs- und Ingenieurwissenschaftlichen Fakultät
der Rheinischen Friedrich-Wilhelms-Universität Bonn
Institut für Bio- und Geowissenschaften
Pflanzenwissenschaften (IBG-2), Forschungszentrum Jülich

UAV-based Imaging of Multispectral Reflectance and Solar-Induced Chlorophyll Fluorescence for Crop Monitoring

von

Saja Salattna

aus
Nablus, Palestine

Bonn 2025

Referent:
Prof. Dr. Uwe Rascher, University of Bonn, Germany

Korreferent:
Prof. Dr. Georg Bareth, University of Cologne, Germany

Tag der mündlichen Prüfung: 10.10.2025

Angefertigt mit Genehmigung der Agrar-, Ernährungs- und Ingenieurwissenschaftlichen Fakultät der Universität Bonn

Acknowledgements

To begin with, I would like to extend my deepest gratitude to my doctoral supervisor, Prof. Dr. Uwe Rascher, whose structured guidance, valuable feedback, and supportive enthusiasm have been huge assets throughout this PhD journey. Your lead has not only shaped this research but has also influenced my career path.

With heartfelt appreciation, I extend my gratitude to my supervisor, Dr. Juliane Bendig, who continuously and tirelessly supported me through this journey with her profound knowledge. Your support and guidance have been instrumental in completing this dissertation.

A special thanks go to Dr. Armagan Eibol for his genuine support, discussions, and contributions.

My sincere thanks also go to Bastian Siegmann, Onno Muller, and Christina Kuchendorf for sharing their expertise, feedback, and assistance throughout this study.

Many thanks also go to Caspar Kneer and scientists from other groups I worked with, including Andreas Dering, Hendrik Poorter, and Hanno Scharr, for their valuable insights and contributions.

Thanks to the BMBF program - the Palestinian-German Science Bridge (PGSB), and the Jülich Research Center for the financial support that allowed me to focus on my research and complete this thesis.

Many thanks to my research group, particularly Julie Krämer for acquiring FloX data, Patrick Rademske for acquiring HyPlant imagery, and Erekle Chakhvashvili for his valuable contribution to my study. I further thank Nils Müller for flying the SIfcam on the UAV and the team at Campus Klein-Altendorf (University of Bonn) for growing the experimental crops.

To my friend Hana, this whole journey wouldn't have been the same without you. Thanks for making the challenging moments enjoyable.

This journey was a tough challenge and not possible without the consistent encouragement of my family. Starting with my dad - thanks for always believing in me, challenging me, and standing up for my dreams. Without your interest in my career, my scientific path in Germany would have never started.

To my husband, thanks for your support, for being part of this journey with me, and for bringing light and laughter to even the most stressful days.

To my Mom, this accomplishment is as much yours as mine; if I succeed in anything, it is because of your endless, unconditional love and support. Thanks for never giving up on my dreams, even when I doubted them! Thanks for everything you've done and continue to do—I am endlessly grateful.

Abstract

The agri-food sector is facing significant challenges due to climate change, unpredictable weather, and rapid population growth. The growing demand to embrace advanced agricultural systems that boost productivity while mitigating climate impacts requires accurate and reliable crop monitoring techniques. In this context, site-specific farm management and remote sensing have become indispensable. Remote sensing offers real-time information about crop growth and health throughout the growing season at different scales. UAV-based remote sensing, in particular, offers a cost-effective tool for monitoring crop growth and health with high spatiotemporal resolution that enables response to field-scale issues by driving informed decision-making. Our study contributes to this evolving landscape by exploring the potential of UAV-based multispectral imaging in crop monitoring on the field scale.

In the first study, high-resolution imagery from the DJI Phantom 4 multispectral UAV system was employed to monitor the seasonal development of spelt in a biochar-enriched experiment. A straightforward data processing workflow was developed based on an empirical line method to convert raw UAV data to normalized and comparable reflectance maps and calculate various vegetation indices. Results indicated that EVI was the most effective index in relation to the actual yield, indicating better spelt development over the biochar-enriched plots with a full conventional fertilization amount compared to controls that received the same conventional fertilization.

The second study addressed the retrieval of sun-induced fluorescence, F_{760}, from SIFcam, a dual-camera system prototype mounted on a UAV. A comprehensive overview and advancements of the developed methodology for SIFcam imagery, in addition to a second innovative workflow, were presented. The F_{760} retrieved from the two workflows showed strong correlations with ground-based measurements ($R^2 = 0.92$) and moderate correlations with airborne imaging spectrometer HyPlant ($R^2 = 0.56$, 0.52 for workflows 1 and 2b, respectively). The SIFcam has shown its capability to effectively disentangle the fluorescence signal from canopy reflectance with a moderate level of accuracy and adequate stability in data collection at the field scale, with less than one-pixel variation between spectral channels in both horizontal and vertical directions.

The third study investigated the potential of integrating SIFcam F_{760} alongside UAV-based multispectral VIs to characterize and delineate diverse new and old winter wheat cultivars. SIFcam demonstrated a notable potential in capturing the variability of F_{760} between wheat cultivars with structural and pigment differences. New wheat cultivars generally revealed higher F_{760}, consistent with their higher chlorophyll content, yet old cultivar Banco indicated that canopy architecture could significantly modulate TOC F_{760}, with F_{760} values comparable to or even exceeding those of certain new cultivars. VIs sensitive to chlorophyll content, particularly TCARI/OSAVI (Cohen's d >= 0.5), outperformed structure-related VIs and F_{760} for distinguishing the cultivars. SIFcam proved to be a valuable tool for field plant phenotyping and potentially guiding breeding programs.

Zusammenfassung

Der Agrar- und Ernährungssektor steht aufgrund des Klimawandels, unvorhersehbarer Wetterbedingungen und des schnellen Bevölkerungswachstums vor großen Herausforderungen. Die wachsende Nachfrage nach fortschrittlichen landwirtschaftlichen Systemen, die die Produktivität steigern und gleichzeitig die Auswirkungen des Klimawandels abmildern, erfordert genaue und zuverlässige Techniken zur Überwachung von Pflanzenkulturen. In diesem Zusammenhang sind eine standortbezogene Betriebsführung und die Fernerkundung unverzichtbar geworden. Die Fernerkundung bietet Echtzeitinformationen über das Wachstum und den Gesundheitszustand der Pflanzen während der gesamten Vegetationsperiode auf verschiedenen räumlichen Ebenen. Insbesondere die UAV-gestützte Fernerkundung bietet ein kostengünstiges Instrument zur Überwachung des Wachstums und der Gesundheit von Nutzpflanzen mit hoher räumlicher und zeitlicher Auflösung, das es ermöglicht, auf Probleme im Feld zu reagieren und fundierte Entscheidungen zu treffen. Unsere Studie trägt zu dieser sich entwickelnden Methodenlandschaft bei, indem sie das Potenzial der UAV-gestützten multispektralen Bildgebung bei der Überwachung von Nutzpflanzen im Feldmaßstab untersucht.

In der ersten Studie wurden hochauflösende Bilder des multispektralen UAV-Systems DJI Phantom 4 verwendet, um die saisonale Entwicklung von Dinkel in einem mit Biokohle angereicherten Experiment zu überwachen. Auf der Grundlage einer empirischen Linien Korrekturmethode wurde ein unkomplizierter Datenverarbeitungsprozess entwickelt, um UAV-Rohdaten in normalisierte und vergleichbare Reflexionskarten umzuwandeln und verschiedene Vegetationsindizes zu berechnen. Die Ergebnisse zeigten, dass EVI der effektivste Index in Bezug auf den tatsächlichen Ertrag war, was auf eine bessere Dinkelentwicklung auf den mit Biokohle angereicherten Parzellen bei voller konventioneller Düngung im Vergleich zu den Kontrollen hinwies, die die gleiche konventionelle Düngung erhielten.

Die zweite Studie befasste sich mit der Gewinnung von sonneninduzierter Fluoreszenz, F_{760}, von SIFcam, einem auf einer Drohne montierten Prototyp eines Dual-Kamera-Systems. Es wurden ein umfassender Überblick und Weiterentwicklungen der entwickelten Datenverarbeitungsmethodik für SIFcam-Bilder sowie ein zweiter innovativer Arbeitsablauf vorgestellt. Die aus den beiden Workflows gewonnenen F_{760} zeigten starke Korrelationen mit bodengestützten Messungen (R^2 = 0,92) und mäßige Korrelationen mit dem luftgestützten bildgebenden Spektrometer HyPlant (R^2 = 0,56 bzw. 0,52 für Workflows 1 und 2b). Die SIFcam hat gezeigt, dass sie in der Lage ist, das Fluoreszenzsignal effektiv von der Kronendachreflexion zu trennen, und zwar mit mäßiger Genauigkeit und angemessener Stabilität bei der Datenerfassung auf der Feldskala, mit weniger als einem Pixel Abweichung zwischen den Spektralkanälen in horizontaler und vertikaler Richtung.

Die dritte Studie untersuchte das Potenzial der Integration von SIFcam F_{760} mit UAV-basierten multispektralen VIs zur Charakterisierung und Abgrenzung verschiedener, neuer und alter Winterweizensorten. Die SIFcam zeigte ein beachtliches Potenzial bei der Erfassung der Variabilität von F_{760} zwischen Weizensorten mit Struktur- und Pigmentunterschieden. Neue Weizensorten wiesen im Allgemeinen höhere F_{760}-Werte auf, was mit ihrem höheren Chlorophyllgehalt übereinstimmt. Die alte Sorte Banco zeigte jedoch, dass die Kronendacharchitektur den TOC-Wert F_{760} erheblich beeinflussen kann, wobei die F_{760}-Werte mit denen bestimmter neuer Sorten vergleichbar sind oder diese sogar übertreffen. Die für den Chlorophyllgehalt empfindlichen VIs, insbesondere TCARI/OSAVI (Cohen's d >= 0,5), übertrafen die strukturbezogenen VIs und F_{760} zur Unterscheidung der Sorten. SIFcam erwies sich als wertvolles Instrument für die Phänotypisierung von Pflanzen im Freiland und als mögliche Leittechnologie für Zuchtprogramme.

Abbreviations

UAV	Unmanned Aerial Vehicle
RS	Remote Sensing
PA	Precision Agriculture
SIF	Sun-Induced Fluorescence
F_{760}	Far-Red Sun-Induced Fluorescence
RGB	Red, Green, Blue
OSAVI	Optimized Soil-Adjusted Vegetation Index
DN	Digital Number
ELM	Empirical Line Method
TOC	Top of Canopy
AGL	Above Ground Level
FWHM	Full Width at Half Maximum
SNR	Signal-to-Noise Ratio
RMSE	Root Mean Square Error
MAPE	Mean Absolute Percentage Error
NDRE	Normalized Difference Red Edge Index
IQR	Interquartile Range
TCARI	Transformed Chlorophyll Absorption in Reflectance Index
GNSS	Global Navigation Satellite System
RADAR	Radio Detection and Ranging
MS	Multispectral
NIR	Near Infrared
SWIR	Short Wave Infrared
LAI	Leaf Area Index
FVC	Fractional Vegetation Cover
NDVI	Normalized Difference Vegetation Index
VI	Vegetation Index
SAVI	Soil Adjusted Vegetation Index
EVI	Enhanced Vegetation Index
MSR	Modified Simple Ratio
MTVI2	Modified Triangular Vegetation Index 2
PRI	Photochemical Reflectance Index
ANN	Artificial Neural Network
RTM	Radiative Transfer Model
GPP	Gross Primary Production
GSD	Ground Sampling Distance
DESIS	DLR Earth Sensing Imaging Spectrometer

PRISMA	PRecursore IperSpettrale della Missione Applicativa
HS	Hyperspectral
NPQ	Non-Photochemical Quenching
PS	Photosystem
PAM	Pulse-Amplitude Modulation
LIFT	Laser-Induced Fluorescence Transient
FLD	Fraunhofer Line Discriminator
SFM	Structure from Motion
TROPOMI	TROPOspheric Monitoring Instrument
FLEX	Fluorescence Explorer (satellite mission)
FOV	Field of View
PAR	Photosynthetically Active Radiation
FCVI	Fractional Canopy Vegetation Index
F_{escape}	Fluorescence Escape Factor
LIDAR	Light Detection and Ranging
LLC	Leaf Chlorophyll Content
GCP	Ground Control Point
RTK	Real-Time Kinematic (a satellite navigation technique)
EXIF	Exchangeable Image File Format
XMP	Extensible Metadata Platform
S-CCCI	Simplified Canopy Chlorophyll Content Index
CVI	chlorophyll vegetation index
SD	Standard Deviation
VNIR	Visible and Near Infrared
UTC	Universal Time Coordinated
SIFT	Scale-Invariant Feature Transform
RANSAC	Random Sample Consensus

Contents

List of Figures

Chapter 1

Introduction

1.1 Remote sensing in plant crop agronomy

The agri-food sector is facing significant challenges due to climate change, unpredictable weather, and rapid population growth [1]. As has been declared by the World Summit on Food Security, "The world's population is expected to grow to almost 10 billion by 2050, boosting agricultural demand by approximately 50 % compared to 2013 levels, even under modest economic growth scenarios" [2]. To meet the estimated nutritional needs of the world, it is essential to boost crop production accompanied by sustainable management practices of agricultural lands to stop or at least slow down the negative impacts on the water and soil quality and quantity, land degradation, greenhouse gas emissions, or biodiversity [3]. However, climate change has begun to cause a reduction in crop productivity in terms of quality and quantity [4, 5].

In light of this challenging context for agriculture, there is a strong requirement for monitoring crop growth and status across locations and environmental contexts, with various temporal resolutions, and for different purposes[6]. Monitoring is an ongoing process of tracking the dynamic changes in crop health and condition during the growing season [7]. Traditionally, crop monitoring involves manual human and ground-based assessments. However, this is a labor-intensive, time-consuming, expensive, and error-prone process and is not feasible for large-scale monitoring [8].

To address the abovementioned limitations, and following an earlier remark by the technology executive committee of the United Nations Framework Convention on Climate Change (UNFCCC) (2014) [9] of embracing agricultural technologies that are capable of increasing productivity to meet the growing food demand while minimizing the adverse effects of climate change, there has been an ongoing global campaign to implement precision agriculture (PA) and remote sensing (RS) technology for the mapping and monitoring of agricultural crops [10, 11].

PA is a data-driven procedure that aims to enhance agricultural productivity under different growth conditions while ensuring sustainability [12]. PA employs a site-specific crop management approach that gathers, processes, and analyses spatial and temporal variability in soil, field, and crop properties using accurate and reliable crop monitoring techniques. By delivering the collected information to the farmers and agronomists, they can make informed decisions about resource allocation and optimize inputs by applying spatially variable agronomic inputs, such as irrigation, fertilizers, and pesticides, tailored to the specific conditions and needs of different areas within a field. This approach not only increases the yield but also mitigates environmental impact by reducing unnecessary input use and nutrient losses. One crucial step of PA is large-scale data collection, which is mostly conducted by remote sensing (RS) techniques, which is the primary driver of the entire PA process along with other technologies, such as robotic systems, weather forecasting technology, and global navigation satellite systems(GNSS) [13, 14, 11].

RS is the process of acquiring information about an object or the surface of the Earth from a distance. Agricultural RS is a specialized field that generates a huge data volume that can be used to non-destructively extract accurate and reliable information to support agriculture decisions. A large part of the generated information is image data, which typically involves the measurement of reflected radiation from canopies. In addition to reflectance, transmittance, and absorption, plant leaves can emit energy by fluorescence or thermal emission. The solar reflected radiation in the optical domain (i.e., between 380 and 2500 nm) is commonly used in vegetation studies because most of the diagnostic absorption features of green vegetation are located in this part of the spectrum [15].

Plants' reflectance is inversely related to radiation absorbed by plant pigments and varies across different wavelengths of incident radiation [16]. It is well known that the spectral reflectance of plants changes with plant type, leaf water content, plant crop growth cycles (phenology), and health. It is determined by the morphological and chemical properties of leaves and plant canopies[17, 18].

RS can serve as an essential tool for spatially and temporally monitoring vegetation [19] by repeatedly providing information on crop status throughout the season at different scales [20, 21]. RS can be utilized as a proactive diagnostic system that enables early detection of crop threats at the early stage, allowing the agricultural community to intervene in problems that spread widely and negatively impact crop productivity [22]. RS aids agriculture in a variety of aspects, including:

- identification of new crop varieties with desirable traits such as increased yield, improved quality, more resistance to specific diseases or pest infestation, and tolerance to environmental stress (field phenotyping) [23, 24],

- monitoring of agricultural land use [20, 25]
- forecasting of within-season crop production [26, 27],
- optimization of short-term production (PA) [16].

There are numerous biophysical, physiological, and biochemical crop properties that can be monitored using spectral reflectance data generated by remote/proximal sensing techniques [28]. However, none of these properties can be directly measured by RS instruments. Instead, RS data serve as a proxy from which these properties are estimated [6]. Among the various approaches developed to retrieve agricultural variables from RS data, the computation of vegetation indices (VIs) stands out as the most widely studied and applied method for assessing crop status[29]. This study focuses on two key aspects of crop monitoring: VIs as a representation of a widely used approach (section 1.2), SIF as an innovative RS signal that enables direct insights into the photosynthetic activity of plants (section 1.3)

Agriculture studies can now benefit from various RS data provided by different passive and active RS systems. In active systems, the sensors emit radiation toward the desired target and record the reflected energy. Thus, they can be used anytime under any weather condition. Examples of active sensors are radio detection and ranging (RADAR) and light detection and ranging (LiDAR), which provide topographic information about terrain properties and elevation of ground-based objects. RADAR is also capable of measuring additional surface characteristics, such as soil moisture. On the other hand, passive sensors record the reflected solar energy from objects on the Earth's surface. Examples of passive sensors are different types of cameras, such as RGB, multispectral, and hyperspectral cameras[8], more details in subsection 1.2.1. Most of the existing studies focus on the optical passive systems because they are prevailingly used to study vegetation properties [30]. Another application for passive sensors with specific technical requirements is the study of chlorophyll fluorescence (ChlF); unlike traditional reflectance-based methods, ChlF sensing techniques capture the energy emitted by plant leaves when excited by light. Research of RS techniques for studying ChlF has recently gained increasing interest, as the signal is directly related to the photosynthetic efficiency [31].

Various RS platforms are currently used in agriculture, including handheld, aircraft, and satellite, to collect data at different spatial, temporal, and spectral resolutions [22]. Each has advantages and limitations (subsection 1.2.1). Satellite imagery, while constantly improving, still lacks the spatial resolution needed for PA [14]. Manned aircraft offer an alternative for large-scale crop monitoring with high spatial and spectral resolutions, but the high operational costs and complexity limit their temporal resolution [32, 33]. Ground-based platforms,

with high spatial and temporal resolution measurements, are limited in spatial coverage and can be time-consuming [34].

In this context, Unmanned Aerial vehicles (UAVs) have emerged as flexible, cost-effective, and promising technology to address these gaps. They offer high spatial and temporal resolutions that facilitate detailed crop monitoring and distinction of individual plants in captured images, making them particularly suited for PA applications and high-throughput phenotyping in breeding programs [24]. This thesis approaches UAV-based crop monitoring through a broad overview of UAV sensors utilized in PA, providing a general recap of their capabilities, applications, and processing (section 1.4). Following this, the focus narrows to investigate two specific UAV systems, a low-cost, widely available sensor, DJI Phantom 4 Multispectral (P4 MS) (chapter 2) and the SIFcam (chapter 3), a highly specialized prototype for measuring chlorophyll fluorescence, to evaluate the sensors' effectiveness in crop monitoring applications.

1.2 Reflectance based-crop traits proxies

Over recent decades, there has been growing interest in extracting vegetation biophysical and biochemical properties from remotely sensed reflectance data [29]. RS applications in agriculture are based on the interaction between incident electromagnetic energy with pigments, intercellular air spaces, water within plant leaves, and scattering of reflected energy in the canopy [35]. The leaf reflectance signature is well-understood, and typically, for green and healthy plants, reflectance is low in the visible region (400–700 nm, VIS) due to the strong absorption for photosynthesis by plant pigments located in the mesophyll, such as chlorophyll and xanthophylls. Contrarily, in the near-infrared (700–1300 nm, NIR), electromagnetic radiation is strongly reflected and scattered within the leaf, as the pigments and cellulose are transparent to these wavelengths [36, 37, 38, 39]. Reflectance in the shortwave infrared region (1300–2500 nm, SWIR) is low due to water absorption between 1,300-2,500 nm [38, 17, 40], Figure 1.1.

However, the interpretation of canopy-level reflectance remains challenging due to multiple light interactions between canopy elements and the background. The canopy reflectance is complex and influenced mainly by the leaf properties (e.g., ratio of mesophyll cell surface to intercellular air spaces, leaf thickness), canopy structure, canopy properties (e.g., leaf orientation in a canopy characterized by leaf angle distribution), and the optical properties of the background soil [41, 42]. Therefore, RS methods try to minimize these confounding effects and enhance the sensitivity of reflectance data towards a trait or a property of interest, like the development of VIs.

The computation of VIs is the most widely studied and applied method for

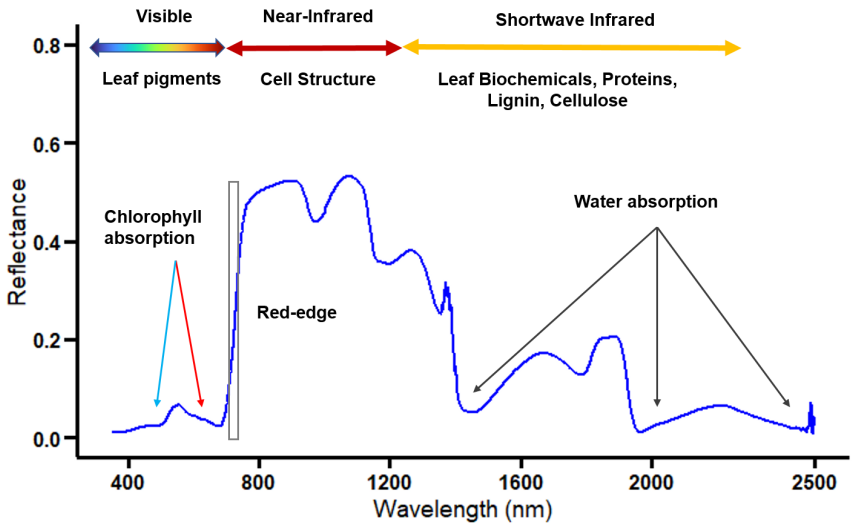

Figure 1.1: Spectral reflectance signatures of grass measured using an ASD FieldSpec Pro (Analytical Spectral Devices) spectroradiometer across visible (400-700 nm), NIR (700-1300 nm), and SWIR (1300-250 nm) wavelengths. The figure highlights key spectral features, including chlorophyll absorption in the visible wavelengths and water absorption bands in the shortwave infrared region.

assessing crop status. Comprehensive recent reviews of VIs have been proposed by [18, 14, 40, 43]. In the following sections, the evolution of the main types of VIs is presented. VIs are simple mathematical transformations/combinations of two or more spectral bands to enhance vegetation spectral signals while minimizing the confounding effects, viewing geometry, and atmospheric conditions [44, 37]. VIs play a vital role in PA and crop monitoring, offering a simple yet effective means of assessing crop condition and health. VIs can also serve as a proxy for vegetation structural, phenological, and biophysical properties, such as leaf area index (LAI), fractional vegetation cover (FVC), biomass, and chlorophyll content [45, 46].

First-generation VIs (red–NIR ratio-based and difference-based VIs), such as the simple ratio (SR), difference vegetation index (DVI), and normalized difference vegetation index (NDVI), were developed to assess vegetation structural properties and quantify vegetation growth. These indices are calculated independently of soil reflectance properties and are based on the sharp contrast in reflectance behavior between the red and NIR portions of the plant spectra [47]. Among these indices, the NDVI is the most widely used VI to quantify vegetation green biomass, LAI, FVC, plant growth, phenology, fraction of absorbed photosynthetically active radiation[48, 49, 29] and properties related to evapotranspiration [50]. However, NDVI is insensitive to densely vegetated areas and

sensitive to confounding effects caused by bright soils, atmosphere, and clouds that may result in erroneous information on crop or plant conditions [51].

Therefore, several improved VIs have been developed in an attempt to address these shortcomings in NDVI. The Soil Adjusted Vegetation Index (SAVI) and its variants were proposed to reduce the effect of soil reflectance [52]. While SAVI is useful in mixed vegetation areas, SAVI may not outperform NDVI in areas with low soil background or where vegetation is not the dominant land cover [53].

The Enhanced Vegetation Index (EVI) has been developed to mitigate the effects of NDVI saturation in areas of dense vegetation. EVI accounts for the non-linear relationship between reflectance and vegetation coverage and integrates blue band reflectance, effectively reducing the atmospheric influence and soil background noise [51, 54]. [55] suggests that compared to NDVI, EVI is more robust for monitoring vegetation health and vigor in areas characterized by significant soil background or atmospheric interference and moderate to high vegetation coverage [46].

The following improvements included the red-edge part of plant spectra. The red edge refers to the sharp transition point in the vegetation reflectance spectrum between the strong chlorophyll absorption in the red band and the high reflectance in the NIR band. [56]. Red edge has been found to have an excellent correlation to chlorophyll content. The shape and position of the red-edge region are strongly influenced by chlorophyll content and LAI; an increase in leaf chlorophyll content causes a shift in the red-edge position towards longer wavelengths. Conversely, low leaf chlorophyll content results in a shift of the red edge towards shorter wavelengths [57]. It has been demonstrated that measures based on the red-edge position or shape are likewise well correlated with biophysical properties at the canopy level but less sensitive to spectral noise caused by the soil background and by atmospheric effects [58]. Red-edge VIs like red-edge chlorophyll index (CIred-edge) and Normalized Difference Red Edge (NDRE) have been widely used for estimating leaf and canopy chlorophyll content [59, 60]. In addition, [61, 57, 62] reported that narrowband red-edge VIs are a powerful alternative to broadband VIs for LAI estimation.

With the advent of hyperspectral sensors, new narrowband VIs have been developed and categorized into three main groups: structure, biochemistry, and plant physiology/stress, as reported by [63]. Structure-related VIs, such as the modified triangular vegetation index (MTVI2) [64] and the Modified Simple Ratio (MSR), are particularly useful for estimating vegetation structure and are less susceptible to saturation in dense canopies. Biochemistry VIs include the Transformed Chlorophyll Absorption in Reflectance (TCARI) [65] for chlorophyll estimation and the Normalized Difference Nitrogen Index (NDNI) for leaf nitrogen content assessment [66]. The Physiology/Stress VIs have expanded beyond

chlorophyll-based metrics to include other pigments crucial for understanding plant responses to environmental conditions. Among these, the Photochemical Reflectance Index (PRI) is related to the xanthophyll cycle [67] and relevant for studying plant photosynthesis. PRI serves as a proxy for photosynthetic light-use efficiency by detecting subtle changes in xanthophyll cycle pigments (carotenoid), which play a key role in photoprotective mechanisms of plants [68, 69].

Narrowband indices have improved the estimations of leaf constituents like chlorophyll and water content [64] and enabled the detection of biochemicals with more subtle spectral absorption features such as protein, lignin, and phosphorus [61].

The estimation of crop properties using VIs is based on empirical relationships between VIs and the variable of interest. Typically, these relationships are established through correlations between VIs and crop traits derived from ground experiment data obtained using destructive methods. Alternative approaches have been developed to build statistical and physical models to describe the relationship between crop traits and reflective RS data[41, 70].

Statistical methods establish a relationship between the vegetation properties and the leaf or canopy spectral reflectance signature, or VI, which are sensitive to the (in-situ) measured variable of interest. These methods rely on spectral, biophysical, and biochemical measurements taken under various field or laboratory conditions across different plant species and growth stages. The accuracy and range of these measurements significantly influence the validity and transferability of the derived relationships [71]. Several statistical models are employed in this context [41]:

1. Linear Regression: The simplest approach is establishing a direct linear relationship between a VI and the trait of interest [72].

2. Multiple Linear Regression: Extends linear regression to include multiple spectral bands or indices as independent variables [72].

3. Stepwise Multiple Linear Regression (SMLR): An iterative process that selects the most relevant spectral bands for predicting the variable of interest. Iteratively adds or removes bands based on their contribution to the model's explanatory power until a satisfactory regression is achieved [72]

4. Partial Least Squares Regression (PLS): iteratively computes factors from linear combinations of multidimensional spectral data, each capturing important patterns in the data, thus separating noise from meaningful correlations and constituting the prediction function [73].

5. Artificial Neural Networks (ANN): A sophisticated non-linear modeling approach that captures complex relationships between spectral data (inputs)

and variables of interest (output). ANN is trained on a learning dataset, where inputs are linked to specific output variables, which allows ANNs to emphasize relevant spectral features while suppressing less significant ones, thereby optimizing the network for the best prediction of variables of interest [74]

Physical approaches use physical radiative transfer models (RTMs) that can accurately simulate the interaction (i.e., scattering, absorption, and transmission) of solar radiation and the canopy from a description of canopy architecture and the optical properties of its constituent elements. RTMs can simulate the spectral reflectance of vegetation at the leaf or canopy scale. RTMs help to study the effects of additional perturbing factors (soil background, non-photosynthetic materials, and observation geometry) on canopy reflectance. Conversely, the canopy variables that fall into the RTM model parameters can be retrieved from RS reflectance, named "inversion mode". This inversion process aims to minimize the cost function between the RTM-simulated signal and the RS-observed signal. By iteratively adjusting model parameters to achieve the best fit between simulated and observed reflectance, RTM inversion enables the estimation of key canopy biophysical properties from RS data [70, 6, 41]. Some properties can be estimated with high accuracy and fidelity, e.g., leaf chlorophyll content, leaf water content, and LAI [30].

Several RTMs were developed from simple 1D models (e.g., SAIL, SCOPE) to complex 3D representations (e.g., DART). 1D RTMs simplify vegetation canopies as horizontally uniform but vertically variable structures and assume vegetation canopy as a turbid medium with randomly distributed leaf clumps and gaps (voids), characterized primarily by LAI and Leaf Angle Distribution [75]. While effective for homogeneous canopies, they may not accurately represent heterogeneous or discontinuous canopies [76]. 3D RTMs offer 3D detailed representations of vegetation structure and use numerous parameters to describe the complex vertical and horizontal distribution of canopy elements, including leaves, trunks, branches, water, soil, and atmosphere. Despite their accuracy in simulating directional reflectance for heterogeneous canopies, the application of these highly parameterized 3D RTMs in vegetation parameter inversion is limited due to challenges in acquiring 3D structural data and high computational demands [77, 78].

Among the RTMs, PROSAIL is one of the most widely used in existing studies. This model is an integration of the PROSPECT leaf-level model and SAIL canopy-level model and enables simulating spectral and directional variation of canopy reflectance based on leaf biochemistry (e.g., chlorophyll and water contents), canopy architecture (e.g., LAI and leaf angle) and soil reflectance [79].

1.2.1 Evolution of optical sensors for remote sensing

The development of VIs has been closely tied to the evolution of satellite technology since the 1970s. Various VIs have been developed based on broad spectral bands, making use of multispectral satellite sensor data. Early VIs were estimated from four VNIR broad spectral bands of Landsat 1 in 1972 at 80 m spatial resolution with bi-weekly revisit times. The advent of broadband Earth-observing satellites, such as Landsat2 and 3 and the advanced very high-resolution spectroradiometer (AVHRR), in the 1970s and 1980s resulted in higher spatial resolution of 30 m and VIs based largely on NIR/visible reflectance [17, 40]. The early 2000s saw a significant leap with The Moderate Resolution Imaging Spectroradiometer (MODIS) aboard Terra and Aqua satellites, with improved spectral resolution and radiometric characteristics as well as a greater number of spectral bands enabling the development of more sophisticated indices like EVI and higher level data products such as LAI, burned area and GPP [51]. Sentinel-2, launched in 2015, further advanced VI and vegetation product capabilities with its ability to calculate red-edge VIs for plant pigments, offering weekly to daily observations at 30 m resolution.

Multispectral data from the above-mentioned satellites have been extensively used in agriculture studies to retrieve various crop and soil properties, such as crop chlorophyll content, biomass, and yield [46]. Yet there are significant limitations associated with the fact that broadband sensors sample only portions of the solar spectrum and at a wide bandwidth that often masks detailed information crucial for understanding subtle changes in vegetation composition, biochemistry, and physiological activity. The sensor's coarse spectral resolution often constrains the accuracy of retrieved VI and variables and hinders the detection of subtle crop stress indicators (e.g., weeds, water, and nutrient deficiencies or excesses) and complex interactions between fallow, forest, and agricultural land. These limitations have motivated the inclusion of hyperspectral sensors onboard the new generation of satellites [80].

Since the 2000s, space-based hyperspectral remote sensing instruments have been launched. The first instrument was the Hyperion [81], launched in 2000 and decommissioned in 2017. The spectrometer provided observations in the visible-SWIR (400-2500nm) with a 30 m GSD. CHRIS (pushbroom Compact High-Resolution Imaging Spectrometer), launched in 2001, offered high spatial resolution (17 m or 34 m) images in the visible and NIR wavelengths and unique multi-angular capabilities for surface reflectance anisotropy characterization [82]. More recent missions include DESIS (Earth Sensing Imaging Spectrometer), which has been installed on the International Space Station in 2018 [83], and PRISMA (PRecursore IperSpettrale della Missione Applicativa) (2019) [84]. However, these two instruments are limited to measuring the visible and near-infrared. The EnMAP

(Environmental Mapping and Analysis Program) satellite, launched in 2022, further expanded capabilities with its prism-based dual-spectrometer system operating in the visible-SWIR across 224 bands, offering high radiometric and spectral accuracy and stability [85]. Copernicus Hyperspectral Imaging Mission for the Environment (CHIME) is expected after 2025 [86] and will also measure in the Visible-SWIR with a high spectral resolution.

Several techniques were developed to evaluate the instrument performance for satellite-based spectral imaging; the most common way is to use in-situ measurements of validation networks, such as those provided by RadCalNet and HYPERNETS, to characterize both surface reflectance and atmospheric properties. Challenges persist in relating satellite pixels to limited ground sampling areas of a few meters. To address this issue, high-resolution airborne imaging spectroscopy or satellite data from dedicated surveys can provide spatially distributed spectra, enhancing satellite performance assessments [84].

Spectroscopy from aircraft has rapidly evolved in the last few decades, with over a dozen operational airborne imaging spectrometers currently in use. Most of these are limited to measuring the visible and near-infrared spectrum (400 to 1000 nm). Yet, a few airborne imagers have expanded this range to cover 400 to 2500 nm, like NASA's Airborne Visible/Infrared Imaging Spectrometer (AVIRIS), the commercial HyMap, developed by Integrated Spectronics Corporation, and the high-performance airborne imaging spectrometer (HyPlant) developed by the Forschungszentrum Jülich in cooperation with SPECIM Spectral Imaging Ltd (Finland) [87].

Despite its outstanding performance, the applicability of hyperspectral imaging in operational agriculture is limited due to limited spatio-temporal coverage of satellite data, the high cost of the sensors, the complexity of the data acquisition process, and various technical challenges such as high dimensionality, and large data volumes that require more complex data analyses[85, 88].

Satellite-based multi- and hyperspectral sensors have confirmed good performance in agricultural studies, but their widespread application in PA faces several challenges, including spatial and temporal resolution. Most satellite-based hyperspectral sensors offer only medium spatial resolutions (e.g., 30 m for sensors like PRISMA, EnMAP, and DESIS) [89]. However, many PA applications, such as crop biomass and yield estimation, typically require high spatial resolution (1-3 m) [16], while weed mapping demands resolution that is finer than the weed patches (e.g., 0.05-0.5 m) [90]. Another constraint is the temporal resolution. The typical two-week revisit cycle of most satellite-based sensors and unfavorable weather conditions may hinder the early detection of crop stress, such as disease or pest.

To fully utilize the rich spectral information provided by HS images and im-

prove their spatial resolution, data fusion techniques such as pansharpening have been developed t. This method combines low-resolution HS images with high-resolution multispectral images or panchromatic images, resulting in images with both detailed spatial and spectral information. This approach can also be used to enhance the temporal resolution, like transplanting the temporal repetition capability of Sentinel-2 MS data into the spectral resolution of HS data to obtain many fused HS observations with only a few original HS datasets [91, 92].

Although ground-based hyperspectral data can be quickly acquired using spectroradiometers (e.g., ASD FieldSpec, Malvern Panalytical, Malvern, UK) and have been widely employed for observing canopy and leaf-level spectral features, these measurements are confined to a few numbers of field sites due to their limited spatial coverage [93, 89]. In contrast, hyperspectral imaging sensors are more suitable to acquire spatial variations of spectral data over a region. The recent development of compact and lightweight-setup sensors that can be mounted on UAVs has further enhanced Hyperspectral applicability and versatility for agriculture applications (section 1.4).

1.2.2 Limitations

Despite VIs being widely used, these indices reach a saturation level in high-density biomass [41, 94]. Saturation is primarily caused by reflectance in the red band as vegetation canopy closure increases. As the upper layers of vegetation absorb most of the red light, additional leaves have minimal impact on red reflectance. In contrast, NIR reflectance continues to increase beyond certain LAI values due to multiple scattering effects. This imbalance between the slight decrease in red reflectance and the continuous rise in NIR reflectance results in only slight changes in certain VIs (particularly NDVI) [95, 96, 43].

Over the years, various approaches (section 1.2) have been developed to mitigate the saturation effect of VIs [97, 98] proposed to adjust the NDVI by adding weighting factors to NIR reflectance to compensate for the minimal change in red reflectance. However, these weighting factors do not account for the influence of the soil background and alter the dynamic range of the NDVI [97]. Other studies focused on creating novel VIs that consider more spectral information from narrow hyperspectral bands. While these new indices achieve greater sensitivity in high biomass canopies [96], hyperspectral data comes with limitations in terms of cost, accessibility, computational demands, and complexity due to its high-dimensional nature.

Reflectance-based VIs are indirect measures of plant properties, producing relative values that require additional equations to link them to physical units. Similarly, VIs primarily indicate potential photosynthetic activity by assessing green leaf area rather than directly measuring the activity of the photosynthetic

machinery, like electron transport following light absorption [99]. Therefore, most VIs are not sensitive enough to detect short-term dynamic changes (e.g., hourly variations) in the photosynthetic process [100, 101]. Plant photosynthesis is a dynamic process, and its efficiency is highly variable and sensitive to environmental conditions. It adapts to incident irradiance or stress factors such as water scarcity by altering leaf pigments, e.g., related to the xanthophyll cycle, often without any detectable changes in reflectance, but readily echoed in changes to the ChlF emissions [102] (section 1.3). Consequently, VIs are limited in capturing real-time vegetation responses to stress events (e.g., droughts)

While statistical approaches for crop trait retrieval are straightforward and fast in computation, they need a large amount of data for calibration and validation. This makes the empirical relationship constrained by the representativeness of the calibration dataset and sensitive to acquisition conditions and crop-specific variables. Consequently, these models have reduced transferability robustness to conditions other than those in which they were developed [6, 103].

RTMs appear to be useful to overcome some limitations of the statistical approaches for the retrieval of biophysical and biochemical variables. However, the use of RTMs is more complex and requires high computational cost in their calibration step [47]. Also, canopy structure presents challenges for RS data interpretation and radiative transfer model (RTM) parameterization. Factors such as leaf clustering and orientation can only be represented in 3D RTMs and require careful parameterization. A key limitation of physical methods is the potential for different RTM input parameter combinations to yield identical reflectance spectra, leading to ambiguity in estimating canopy properties from RS data.

1.3 Chlorophyll fluorescence (ChlF)

Chlorophyll fluorescence (ChlF) can be considered as a direct indicator of photosynthetic efficiency [104, 105, 106, 107]. The light energy absorbed by chlorophyll molecules undergo one of three main pathways: used to drive photosynthesis (photochemistry), dissipated as heat (non-photochemical quenching; NPQ), or re-emitted as fluorescence [108, 109]. Under optimal physiological conditions, the major part of the absorbed light (up to 80%) is used for electron transport in photosynthetic light reactions to generate energy carriers (ATP and NADPH), which are required to assimilate CO_2 in the carbon reduction cycle (Calvin-Benson cycle) [110, 111]. Meanwhile, the remaining absorbed light must be discharged to prevent overexcitation and potential damage to the photosynthetic apparatus. NPQ is a photoprotective mechanism in plants that regulates the distribution of excitation energy between reaction centers and antenna complexes. NPQ is regulated by the pH of the thylakoid lumen and the aggregation state of antenna

complexes. The xanthophyll cycle plays a crucial role in NPQ; under high light intensity, the electron transport chain saturates, and proton accumulation in the thylakoid lumen tends to decrease lumen pH. The drop of the pH activates the PsbS protein and triggers the violaxanthin de-epoxidase enzyme, which helps the conversion of violaxanthin to zeaxanthin (xanthophyll cycle). The binding of protons and zeaxanthin to light-harvesting antenna proteins causes conformational changes that result in quenching and heat dissipation [112, 113, 114]. The xanthophyll cycle is the only NPQ mechanism that is related to pigment changes. Thus, it can measured remotely using the PRI. PRI is sensitive to changes in xanthophyll cycle pigments, reflecting the de-epoxidation state of these pigments [69].

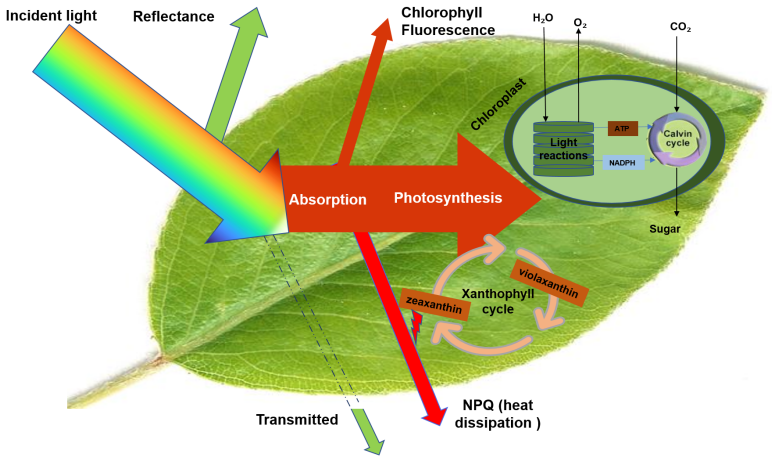

Figure 1.2: Distribution of absorbed light energy in leaves under steady-state conditions

Accordingly, ChlF is the re-emission of the absorbed light at a longer wavelength compared to the excitation wavelength [109, 115]. The full emission of the ChlF spectrum covers the wavelengths ranging between visible to NIR spectrum of 640–800 nm, with two peaks: one in the red spectral region around 685 nm and the other in the far-red around 740 nm. Two photosystems are involved: photosystem II (PS II) contributes to the ChlF emission in red and far-red spectrum regions, whereas photosystem I (PS I) contributes mainly to the far-red spectral region [102, 31, 116, 110]. Abiotic and biotic stress factors impact the photosynthetic reactions and trigger the dynamic regulation of the two photosystems. Between the two, PS II response is particularly more dynamic, and changes in the functional status of PS II are directly and mechanistically reflected in changes in the emission of ChlF signal [31]. Compared to far-red ChlF, red ChlF is more strongly correlated to PS II activity and, consequently, to plant photosynthetic activity. Red ChlF is subject to stronger reabsorption within leaves and canopies [117]. The reabsorption is caused by the overlapping of the shorter wavelengths

of the ChlF emission spectrum and the longer wavelengths of the chlorophyll absorption spectrum [110].

1.3.1 Connection between ChlF and photosynthesis

At the photosystem level, ChlF is directly connected to photosynthesis dynamic regulation. This relationship can be understood by looking into the mechanisms of quenching and non-quenching of excited chlorophyll [109]. With the other dissipative pathway, NPQ energy, ChlF competes with photosynthesis at the same excitation energy to use the absorbed light. Consequently, any increase in the efficiency of one mechanism will cause a decrease in the yield of the other two [102, 105, 109]. Generally, ChlF production is inversely related to photosynthesis, except in the presence of plant stress and high irradiance conditions. In such cases, ChlF and photosynthesis both tend to decline (positive correlation), where NPQ processes are triggered (thermal dissipation) to dissipate excess energy and prevent damage from harmful radicals formed in those conditions [118, 119, 112]. Hence, measuring the fluorescence emission efficiency can provide information about changes in the efficiency of photochemistry, as well as heat dissipation [109].

ChlF emitted from the core of photosynthetic machinery offers a more accurate carbon assimilation estimate and early stress detection rather than normal reflectance spectra and VIs [115, 102]. ChlF can be used to detect physiological strains early before a significant reduction in chlorophyll content and visible symptoms appear [115, 119]. Early detection allows remedial action before survival, growth, and productivity are restrained. However, as ChlF is affected by many factors, it cannot identify a particular stressor but only indicates evident physiological strain [119].

1.3.2 Measurements of ChlF

In 1834, the first recorded observation of chlorophyll fluorescence was made when Sir David Brewster, a Scottish preacher, discovered that passing a beam of sunlight through a green leaf extract of laurel leaves produced a brilliant red light [120]. He also observed that as the light passed the increasing thicknesses of the extract, the color of the emitted light changed from red to orange to yellow. This transition possibly represents the first recorded evidence of reabsorption by chlorophyll [121].

Changes in the yield of ChlF were first observed in 1960 by [122] and became known as the Kautsky effect, which describes the phenomena of variation in ChlF yield upon transferring photosynthetic cells from darkness to light. ChlF first increases rapidly to a maximum (in approx. 1 second) due to the saturation

of Photochemical quenching (PQ) (close the reaction centers of PSII). Subsequently, ChlF decreases to a steady state after a few minutes of illumination due to the trigger of NPQ to dissipate the absorbed excessive light energy until PQ is re-established. dissipation)[110]. Actively induced ChlF is the most widely used indicator of the functional status of PS II on the leaf level [112]. ChlF measurements made their move towards field applications with the development of pulse amplitude-modulated (PAM) fluorometry. PAM uses saturating pulses to close the PS II reaction centers and induce the max ChlF emission [123]. PAM fluorometry has facilitated the study of leaf photosynthesis and helped clarify the link between ChlF and photosynthetic CO_2 assimilation [107]. The handheld Mini-PAM device offers rapid leaf fluorescence assessments, while the stationary Monitoring-PAM enables continuous field measurements. However, upscaling this method from the leaf to canopy level is limited by the close range needed to apply the saturating flashes[124]. To address these challenges, the light-induced fluorescence transient instrument (LIFT) has emerged, allowing fluorescence measurements in terrestrial vegetation from several meters above the canopy (up to 50 m). LIFT uses a pulsed laser, and in later versions of LED, an excitation signal is applied with variable duty cycles, resulting in a fluorescence transient that is fitted with a model to extrapolate the maximum fluorescence [125, 126]. Lift is integrated into automated systems for phenotyping in high spatio-temporal resolution [127] to investigate the effect of elevated CO_2 on photosynthetic dynamics and growth patterns [128].

1.3.3 Remote sensing of SIF

RS of solar-induced chlorophyll fluorescence (SIF) is based on the passive measurement of ChlF induced by the absorption of sunlight. SIF is an innovative RS signal that can serve as a real-time proxy of photosynthetic activity and its dynamics under natural illumination at the leaf, canopy, ecosystem, or even global scale [107, 129]. However, measuring SIF is challenging as, under solar illumination, the SIF signal is always superimposed on the reflected light. Since the SIF emission contribution to the signal detected by a remote sensor is weak and typically constitutes 1–5% of the vegetation's reflected radiance in the near-infrared [102, 130, 131], the decoupling of the two signals is challenging. SIF can be detected passively by exploiting specific absorption features in the solar or the Earth's atmospheric spectrum, where irradiance transmission through the atmosphere is strongly reduced, and SIF contribution to reflected radiation is relatively stronger [102, 132, 129]. An important algorithm for measuring SIF is the Fraunhofer line discriminator/depth (FLD). The FLD relies on two flux measurements: incident solar irradiance and the apparent reflected radiance (termed "apparent" as it includes SIF) inside and outside of the absorption feature [116, 102, 133].

Typically, the solar Fraunhofer lines (SFL) Fe (758.8 nm) and KI (770.1nm)[134] or the Earth's two telluric oxygen absorption features O_2B (687–692 nm), and O_2A (759–770 nm) bands are used due to their spectral proximity to the SIF emission peaks [129]. The O_2 absorption bands were used more than the Fraunhofer lines feature because these bands are wider and deeper and do not require as high spectral resolution as SFLs (<0.1 nm). Nonetheless, SIF retrieval in the O_2 absorption bands is more complex than in the SFL, as atmospheric and surface factors significantly affect band depth. Atmospheric correction is necessary to separate the little contribution of SIF at the top of the atmosphere from these factors. In contrast to the O_2 bands, SFLs offer the advantage of being unaffected by terrestrial atmospheric absorption, allowing direct observation of fluorescence-induced filling-in without complex atmospheric corrections. [31, 135]. Most of the approaches in the literature on SIF retrieval are based on the principle of Fraunhofer Line Depth (FLD), proposed by [133]. Nevertheless, these FLD methods are different in their assumptions of the spectral behavior of the SIF and reflectance spectra and how they measure band depth. While the Simplified FLD assumes that reflectance and fluorescence are spectrally constant inside and outside the absorption band [133], the modified FLD (3FLD) supposes that they vary linearly [136]. The improved FLD (iFLD) assumes a non-linear relationship and uses interpolation (cubic or spline to estimate reflectance within the absorption band [137]. Spectral fitting methods (SFM) [138, 102], have been proposed for more robust and accurate retrieval, defined as methods in which both reflectance and fluorescence are determined by spectral curve fitting.

The advancement of passive RS technology and prototypes has made global retrievals of SIF achievable using different atmospheric chemistry satellites, such as the Greenhouse Gases Observing Satelite (GOSAT) [134], the Global Ozone Monitoring Experiment-2 satellite (GOME-2) and the Orbiting Carbon Observatory-2 (OCO-2) [139]. Most recently, moderate spatial resolution (3.5x7 km) SIF retrievals with a daily revisit time space were achieved with the TROPOspheric Monitoring Instrument (TROPOMI) onboard the Copernicus Sentinel-5P mission [140]. These studies have recognized the potential of satellite-based SIF to better understand the photosynthetic functioning of vegetation at a large scale. To further explore the potential of SIF, the European Space Agency plans to launch the FLuorescence EXplorer (FLEX) satellite in 2026. FLEX will be the first satellite mission dedicated to globally mapping vegetation fluorescence at an unprecedented spatial resolution of 300 m. It will allow the retrieval of the full spectrum of fluorescence with a moderate temporal and high spatial resolution globally available [111]. Complementing the satellite observations, airborne sensors, often imaging spectrometers, allow mapping SIF over plant canopies at local and regional scales with an intermediate spatial resolution [31]. The airborne SIF

measurements have also evolved as a key component of the calibration and validation of the spaceborne sensors[132]. Ground-based measurements provided the first concise comparison of fluorescence emissions across a range of temporal scales and diverse plant functional types[141]. They are essential for scaling up and understanding energy-matter interactions from leaves to top of canopy levels (TOC) and calibration and validation of airborne and UAV observations [142, 132]. In addition, the combination of flux observations and SIF on towers plays a crucial role in the accurate estimation of biosphere-atmosphere CO_2 exchange within the global carbon cycle.

1.3.4 Challenges

The technology to measure SIF and data availability far outpaces the growth in mechanistic understanding of SIF dynamics and their relationships with photosynthesis and our capacity to interpret the acquired data in meaningful applications. These issues are due to different challenges, which can be summarized into three main factors: measurement instrumentation limitations, scaling issues, and interpretation complexities [116, 143].

There is currently no orbiting satellite designed explicitly to measure SIF from space directly until FLEX is launched. In the meantime, satellite SIF has been retrieved from other instruments designed for atmospheric chemistry studies and recently from TROPOMI. Existing SIF products are restricted to either low spatial resolution, incomplete global coverage, low temporal resolution, short temporal coverage, high-precision errors, or a combination of these. This makes them inadequate for addressing the information needs of most agricultural and forestry management or long-term monitoring and quantifying the global gross primary productivity of global ecosystem production (GPP) and carbon budget [111, 144, 143].

Despite the widespread use of satellite-derived SIF to investigate GPP, there is still a gap in understanding the SIF-GPP relationships at different spatial and temporal scales, which hinders the use of SIF to assist in estimating GPP on large scales. Validating the SIF derived from satellites with eddy covariance (EC) based GPP measurements is challenging due to the inconsistencies in the footprint coverage. Existing satellite SIF products spatial resolution ($\geq 7\,\mathrm{km}^2$) does not match with the EC towers footprints of around 0.5 to 1 km. Therefore, obtaining high-resolution SIF data is imperative for studying the relationship between satellite SIF and tower-based GPP [145, 146].

At the field and landscape scale, airborne imaging spectrometers [147, 148] offer intermediate-scale observations bridging the SIF measurement from small-scale field to satellite observations. However, validating airborne SIF products is vital. Ground-based SIF systems aid in validation, but comparing them to

airborne SIF is challenging due to footprint differences [149, 150]. Also, periodic and campaign-based use of airborne sensors is costly, limiting their applicability for large-scale or continuous SIF mapping [132]. Although airborne sensors, e.g., HyPlant, enable SIF observations with pixel sizes of approximately 1 m, finer spatial resolution is required for studying the impact of vegetation structure on the spatial heterogeneity and angular anisotropy of the SIF signal. Ground-based setups offer small field-of-view (FOV) and limited spatial coverage due to their proximity to the measured targets (0.1 -10 m above the canopy). They can only monitor SIF signals from a few individual plants, requiring upscaling schemes for use on larger scales [150, 151]. In addition, proximal point measurements have limited suitability when investigating different canopy structures, where the signal is always an integration of the FOV. The interpretation of SIF signals into meaningful information and new applications require a fundamental understanding and a quantitative description of the processes linking measured chlorophyll fluorescence with photosynthesis. Although the relationship between fluorescence and photosynthesis at the leaf level is well understood using active fluorescence techniques[107, 105], the relationship between passive fluorescence and photosynthesis at the canopy level is more complex [149]. SIF observed at TOC is affected by canopy structure, biochemical properties, viewing geometry, and within-canopy light level [152, 131, 153]. TOC SIF is only a portion of the total emitted SIF from individual leaves due to reabsorption and scattering and the interactions of the incident photosynthetically active radiation (PAR) with canopy elements and soil. SIF at 760 nm (far-red SIF) is scattered more and reabsorbed less than SIF at 687 nm (red SIF) (overlap with a wavelength range of the ChlF absorption spectrum). Thus, the portion of SIF reaching the sensor is higher for far-red SIF than for red SIF [154]. Likewise, variability of surface illumination within the canopy affects retrieved SIF, such that sun-exposed leaves produce higher SIF due to increased incident radiance compared to shaded leaves under diffuse illumination [131, 153].

As a result, SIF measured at the TOC SIF is different from SIF measured at the leaf level and cannot be directly used to detect variations in plant physiology and make comparisons of SIF acquired by different sensors at varying scales challenging. In an attempt to solve the ChlF scaling issue from leaf to canopy scale, [155] tackled the canopy structure interference and introduced the fluorescence escape fraction (F_{escape}) as the ratio of apparent SIF at the canopy level to SIF at the leaf level.

Recent approaches utilize canopy reflectance data acquired under identical conditions of the SIF measurements to explore the F_{760} scattering based on the spectral invariant theory [156]. [152] developed a method to correct the F_{760} for scattering effect by defining F_{escape} as the ratio of NIR TOC reflectance to canopy

interception. Building on this, the authors [157] developed the near-infrared reflectance of vegetation (NIRv) index as NIR reflectance multiplied by NDVI and uses the fraction of absorbed photosynthetically active radiation (fAPAR) as a proxy for canopy interception. NIRv ($F_{escape} = R_{NIR} \cdot \frac{NDVI}{f_{APAR}}$) is used as a proxy of the fraction of photons that escape from the canopy in near-infrared wavelengths. However, this approach is not universally valid as it is not fully consistent with radiative transfer theory in certain estimation steps. Following a similar concept, the authors [156] proposed the fluorescence correction vegetation index (FCVI), calculated as the difference between NIR reflectance at 770 nm and the average VIS reflectance. Normalizing TOC F_{760} by FCVI and PAR is an estimate of F_{760} emission efficiency. The FCVI showed consistency with spectral invariant radiative transfer theory. Nevertheless, FCVI is unsuitable for very sparse vegetation canopies as it underestimates the soil contribution.

Recent advancements in radiative transfer modeling (RTMs) have demonstrated the potential to study light-canopy interactions and to resolve the leaf-to-canopy SIF scaling issues [118, 152, 158]. RTMs provide a way to predict scattering if the canopy biochemical and biophysical variables are predefined. However, these models require in-situ measured data for validation and as input for parameterization.

1.4 Uncrewed Aerial Vehicles (UAVs): Enhancing remote sensing capabilities

Initially, UAVs were used for hobby model pilots and military and civil surveillance roles; however, in the last 15 years, their use has rapidly expanded to other applications (commercial, scientific, agricultural, etc.). In the early 2000s, the advent of digital technologies and advanced sensors enabled a broader adoption of drones for agricultural use. Modern drones are capable of collecting high-resolution data on various aspects of crop management [159, 160].

UAVs are now very commonly used in RS applications for PA, offering high spatial and temporal resolution and broader coverage of the field, which enable crop monitoring, yield estimation, early disease and pest detection, weed management, and water stress assessment [161, 160]. Machine learning is often used in UAV-based applications in PA, mainly for prediction and/or identification purposes due to its capability to address linear and nonlinear problems and handle large amounts of data. Both unsupervised and supervised learning techniques are being exploited via clustering, classification, and regression methods [162, 163]. Classification methods are widely used for weed mapping and stress detection. The most popular and precise classification technique used for this purpose is

Convolutional Neural Networks (CNNs) [164], with some studies reporting up to 98% mean accuracy in the detection of broadleaf and grass weeds among soil and soybean using RGB imagery acquired from the Phantom DJI 3 [165] and accuracy rates exceeding 90% in detection the grape disease and infected areas in vineyards using RGB images. Regression methods and statistical models are employed to estimate VIs from UAV-based data and use them to predict/estimate features like nitrogen content, LAI, and biomass[32]. [166] found that the Random Forests algorithm has shown very good performance in estimating leaf nitrogen content (R^2 up to 0.79) from different winter wheat varieties using images acquired using the five-band multispectral camera.

Not only can UAVs be used for monitoring and detection purposes but also in direct interventions on crops, including precision spraying, fertilizer applications, and pesticide and herbicide spraying [160]. Studies have shown that drone-based spraying offers significant advantages over traditional methods, including reduced fertilizer and pesticide consumption and enhanced application precision, allowing for more uniform and targeted nutrient distribution. This increased precision translates into better nutrient absorption by plants and reduced fertilizer leaching [167, 168].

In agriculture applications, various types of sensors can be mounted on UAVs. The main on-board sensors are visible light sensors (RGB), multispectral sensors, hyperspectral sensors, LIDAR, and thermal sensors [169]. However, the need for low payload capacity and the utilization of small platforms pose several limitations to the selection of the sensor(s) to be used. Sensors must meet key criteria, including low weight, low energy consumption, and small size [170]. Thermal imaging provides canopy temperatures that can reveal variations in stomatal conductance as an indicator of the plant response to the water availability and transpiration rate. Thermal RS has proven a reliable way of detecting the physiological status of plants under different biotic and/or abiotic stresses, yet data interpretation is affected by environmental conditions [171]. Over the past years, a variety of lightweight hyperspectral sensors for UAVs, including both pushbroom and snapshot types, have been developed and placed on the market, along with some developed research initiatives and projects [172]. Hyperspectral sensors were utilized successfully in plant phenotyping to extract structural and physiological plant properties, crop disease pathology, plant stress, and yield prediction [173]. However, their application in UAV agriculture is still confined by the high cost of the lightweight hyperspectral sensors and challenging data processing to retrieve the desired products [174].

On the other hand, RGB sensors, commonly used in low-cost drones and cameras due to their lightweight and affordability, are typically employed to visually inspect crop health and detect any obvious issues, such as pests or diseases,

due to their superior spatial resolution. RGB is the most used sensor in image-based precision phenotyping to retrieve plant heights and assess plant number or density, estimate field emergence, and yield prediction [173]. However, RGB is limited in its ability to detect changes in vegetation health and productivity due to the lack of spectral range [175]. LIDAR has also achieved good results in estimating geometric properties like height and biomass. The application of LIDAR is limited by a large amount of data processing[175].

In contrast, multispectral sensors have emerged as a persuasive tool that strikes a delicate balance between applicability and affordability. These sensors can provide multiple spectral bands from visible to NIR with centimeter-level spatial resolution. In addition, their low cost, compact dimensions, and fast frame imaging make them well-suited for UAV applications [176, 177, 178]. Analysis of UAV-based multispectral data has shown to be successful in estimating LAI, nutrient uptake, chlorophyll content, yield prediction, and early detection of crop stress and diseases [24, 12].

UAVs can also be equipped with passive sensors designed to measure SIF. To our knowledge, only a few studies have demonstrated the retrieval of SIF using UAV platforms, which will be discussed in section 3.1.

Raw snapshot image data taken by UAV platforms are not ready to extract crop physiological properties. While standardized workflows are still evolving, a general approach to process imagery acquired by multispectral sensors mounted on drones typically involves the following key steps:

1. Preprocessing of raw images mainly includes sensor-related corrections (noise correction, vignetting correction, and lens distortion correction) to extract geometrically consistent at-sensor data from the raw data. Radiometric correction is used to convert the raw sensor digital numbers (DN) into spectral radiance or reflectance [176].

2. Image stitching and 3D reconstruction: The most common method employs photogrammetric techniques, following these steps [179, 180, 32]:

   (a) Image alignment: match and align preprocessed images using advanced computer vision and photogrammetric algorithms. Aerial triangulation and camera calibration are initially performed to recover camera poses and scene structures. The most commonly used set of algorithms for this purpose is summarised under the term Structure from Motion (SFM). The main advantage of SfM is that it does not require initial values of camera poses or information regarding the scene structures [181]

   (b) 3D point cloud generation: Creation of a dense 3D point cloud representation of the surface.

(c) Mesh and Digital Elevation Model (DEM) creation: Generation of 3D mesh models and DEMs, including Digital Terrain Models (DTMs) or Digital Surface Models (DSMs).

(d) Orthomosaic production: Creation of geometrically corrected aerial images with uniform scale using the 3D models.

Specialized software tools have been developed to enable faster data processing. For example, Agisoft Metashape (Agisoft LLC, St. Petersburg, Russia) and Pix4D (Pix4D, Prilly, Switzerland) are commonly used for processing and fusing multispectral data to create 3D models and orthomosaics.

1.5 Research objectives and thesis structure

The main objective of this thesis is to extend the application of optical UAV-based remote sensing in precision agriculture and plant monitoring. The research focuses on developing novel workflows to create high spatial resolution maps for detecting changes in crop performance and physiological status using both UAV-based multispectral and solar-induced fluorescence (SIF) imaging sensors. More specifically, the research objectives were formulated as follows:

1. To assess the potential of a high-resolution DJI Phantom 4 multispectral UAV-based imaging system in detecting and quantifying the short-term impacts of biochar treatments on spelt crop performance at various growth stages, and developing a comprehensive data processing workflow from raw imagery to reflectance maps and vegetation indices (VIs) (chapter 2).

2. To develop and validate an optimized workflow for processing data from the SIFcam, a novel UAV-based SIF imaging system, to generate centimeter resolution maps of far-red solar-induced chlorophyll fluorescence (F_{760}) on the field scale. This includes assessing the accuracy, stability, and comparability of the retrieved F_{760} maps with the ground and airborne-based F_{760} while quantifying associated uncertainties and evaluating the system's performance on a moving UAV platform (Chapter 3).

3. Evaluating the robustness and plausibility of SIFcam's processing chain under different canopy structures by comparing two types of winter wheat varieties that were bred before and after the green revolution in terms of their ChlF and spectral data (Chapter 4).

Chapter 2

Reflectance-based vegetation indices from a low-cost multispectral sensor

This chapter is partially based on the author's published article:

S. Salattna, J. Bendig, C. Kuchendorf, C. Jedmowski, and U. Rascher, "Monitoring Crop Seasonal Development under Biochar Treatment with Unmanned Aerial Vehicle (UAV)-based Multispectral Imagery," In Proceeding *Wissenschaftlich-Technische Jahrestagung der DGPF in Publikationen der DGPF Band 31*, München, Germany, 2023, DOI: https://doi.org/10.24407/KXP:1841079561 .

The table below indicates the origin of different sections within this chapter:

Newly added	Adapted †	Original
Figure 2.2, Figure 2.4,Figure 2.6, Figure 2.5 ,	section 2.1, subsection 2.2.6, section 2.3,section 2.4, Figure 2.3	everything else

2.1 Introduction (†)

In the context of mitigating climate change and adapting to the loss of soil fertility, there is a particular interest in assessing the impact of biochar-facilitated fertilizer application in agroecosystems [182]. Biochar is a black carbon-rich product obtained through the pyrolysis of various biomass, for example, wood, manure, or crop residues, under oxygen-free or oxygen-deficient conditions [183, 184]. Biochar ameliorates soil physical, chemical, and biological properties [185, 186, 187]. Biochar amending to soil has shown beneficial results in terms of enhancing soil fertility, structure, water holding capacity, water availability to plants, organic carbon content, and microbial performance [188, 187]. Consequently, biochar was reported to sustain crop productivity significantly [189, 190] by improving nutrient availability while simultaneously reducing leaching losses [191].

Biochar is recalcitrant carbon that degrades slowly in soils and can take thousands of years to be fully degraded [192]. Thus, biochar can serve as a long-term carbon sink that can contribute to soil C sequestration and reduce greenhouse gas emissions, which can mitigate the impact of climate change [191, 193]. Another reported benefit of biochar is its potential for the recuperation of degraded and contaminated soils through the long-term adsorption of heavy metals [194]. However, the final effect of biochar application is strongly dependent on the crop types, soil types, and biochar types, including feedstock sources, pyrolysis temperature, and the particle size of biochar [195, 196]. A large variation in plant productivity responses to biochar application in soil was documented in previous studies due to the high heterogeneity of biochar properties, soil conditions, experiment designs, and environmental conditions [197]. [198] documented that biochar likely improves crop production in highly degraded and nutrient-poor soils, while its application to fertile and healthy soils does not always increase crop yield.

Despite the growing literature investigating the effect of biochar on total crop productivity, the effects of biochar on crop development over the growing season have received much less attention. The spatio-temporal information provided by visible and NIR UAV images can reveal variability in crop performance due to the presence of biochar within the agricultural soils. So far, the authors [199, 200] conducted two studies that investigated the advanced perspectives of optical UAV (10 channel MicaSense RedEdge-M) RS in combination with in-situ ground measurements of crop traits for monitoring the crop growth dynamics affected by century-old biochar enrichment in PA. In the first study, he assessed chicory growth over 11 biochar-enriched patches and adjacent reference soils, finding that biochar significantly enhanced canopy cover and leaf lengths but negatively impacted plant greenness and increased crop stress without affecting yield.

In a second study focused on winter wheat, seven RGB and six multispectral flights revealed a significant positive effect of biochar on canopy cover (p-value = 0.00007) and early-season crop development (p-values < 0.01), although no impact was noted by the end of the season. Both studies highlighted that factors such as soil variations are more critical than biochar presence in influencing crop health and yield variability.

To date, short-term biochar effects on plant systems using high-resolution UAV-based data at the canopy level have yet to be addressed. Our study aimed to describe the ability to use the small-scale, high spatial-resolution UAV system to detect the differences between biochar fertilized fields and control fields and to investigate at which development stage those differences can be quantified or detected. Due to the high fertilization standard of the study field, the expected impact of biochar-facilitated fertilization on crop growth may be low but possibly detectable using high spatial-resolution UAV imagery. The available imagery source was VNIR multispectral data collected over one crop growth season. This study proposes a data processing workflow, from raw imagery to creating a reflectance map and extracting VIs. The main question the study aimed to answer is: Can the DJI P4MS-based VIs capture the impact of the short-term biochar treatments on spelt (*Triticum aestivum ssp. spelta L.*) crop performance at the canopy level?

2.1.1 Methods and tools

2.1.1.1 Site description

The study area was a farmer's field of approximately 21 hectares cultivated with spelt, located in Germany (latitude: 50° 58'55.1"N, and longitude: 6°25'50.4"E) (Figure 2.1). Spelt seeds were sown in December 2022. The Muencheberg soil quality rating (SQR) of the area is >85, Colluvisol over Chernozem-parabraunerde. Spelt development was monitored during the experiment from the Booting stage to the senescence. The experimental treatment consisted of three biochar-enriched stripes with a diameter of 6 m along the field's length. Each stripe was treated with 1 ton/ha of terra preta biochar and 180 kg nitrogen/ha, 90 kg N/ha, and 40 kg N/ha for stripes T1, T2, and T3, respectively. Apart from these biochar-enriched stripes, the experimental field was exposed to homogeneous agricultural practices, and the soil was treated with organic minerals of 180 kg N/ha, Figure 2.2. Three 3 $\times$100 m plots (red stripes in Figure 2.1) were selected inside the biochar-enriched stripes, at least 1.5 m from the border of each stripe, to avoid gradient effects at the edge of the treatments. Subsequently, three plots of 3 $\times$100 m (black stripes in Fig. 1) were selected as reference soil areas within a distance of approximately 3 m from the biochar-enriched stripes to ensure comparable soil

properties while preventing effects from mixing of biochar and reference soil particles. A set of ground control points (GCPs), consisting of five 0.3×0.3 m targets, were placed in the field for geo-referencing UAV images. GCP coordinates were measured with a real-time kinematic (RTK) global navigation satellite system (GNSS) (Hiper VR, Topcon Positioning Systems, Inc., Tokyo, Japan) with an overall accuracy of 0.01 m.

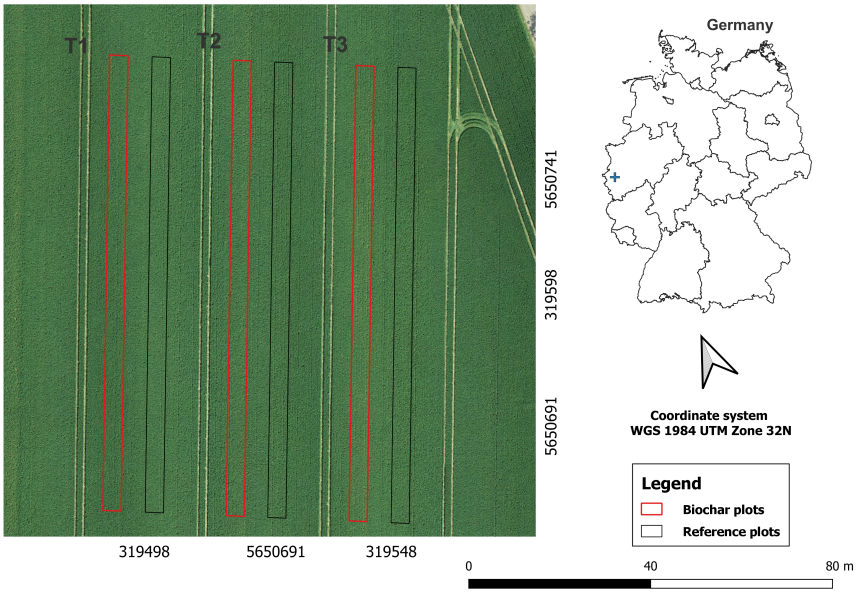

Figure 2.1: Map of the experimental pairs (reference vs biochar plots) in the spelt field in Ameln-Titz, Germany. Background image corresponds to the Red-Green-Blue (RGB) orthomosaic captured by UAV on 02 June 2022

Figure 2.2: Biochar-enriched soil strips in the field. The dark stripe: biochar-enriched. The lighter areas: no biochar (*)

2.1.1.2 Phantom 4 Multispectral

A multispectral RS dataset was acquired during the 2022 growing season using the multispectral camera mounted on the DJI Phantom 4 Multispectral (P4M). The P4M camera has six bands, including one RGB sensor and five monochrome sensors capturing blue (450 nm central wavelength), green (560 nm), red (650 nm), red-edge (730 nm), and near-infrared (840 nm). Each spectral sensor has a global shutter and 1600×1300 pixels image resolution. In addition, the P4M is equipped with a band-by-band incident light sensor, which allows the irradiance measurement for each band during flight. The P4M integrates a built-in DJI Onboard D-RTK module that provides real-time and centimeter-level positioning accuracy.

2.1.1.3 Data acquisition

The UAV was flown at 50 m above ground level (AGL) with an airspeed of 4.25 ms^{-1}. The forward and side image overlaps were 75% and 65%, resulting in a ground sampling distance (GSD) of 0.035 m. During data collection, six flights were performed between May and July 2022 in clear sky conditions and between 12:00 to 15:00 h local time. For each flight, a set of Lambertian reference panels with known hemispherical-conical reflectance factors was placed next to the field and recorded at flight altitude to enable the generation of reflectance maps in the postprocessing.

2.2 Data processing and analysis

The data processing workflow, including data processing and VIs extraction (Figure 2.3. First, the individual images were corrected for the vignetting effect (subsection 2.2.1). Then, raw digital numbers (DNs) were corrected for sensor gain and exposure time, yielding normalized DN values (subsection 2.2.2). These two steps were performed on the individual images using an in-house developed Python code. The corrected images were processed using the Metashape processing workflow (Agisoft LLC, St. Petersburg, Russia), which included GCPs for georeferencing orthomosaics as final products. The empirical line method (ELM) was applied for atmospheric correction and to create reflectance maps using a Python code (subsection 2.2.4). Several VIs were then calculated from the reflectance maps using the raster calculator tool in QGIS (subsection 2.2.5). In addition, a mask was applied to the VIs maps in QGIS to exclude soil pixels before conducting the statistical tests to examine the difference between the reference and biochar plots ,subsection 2.2.6.

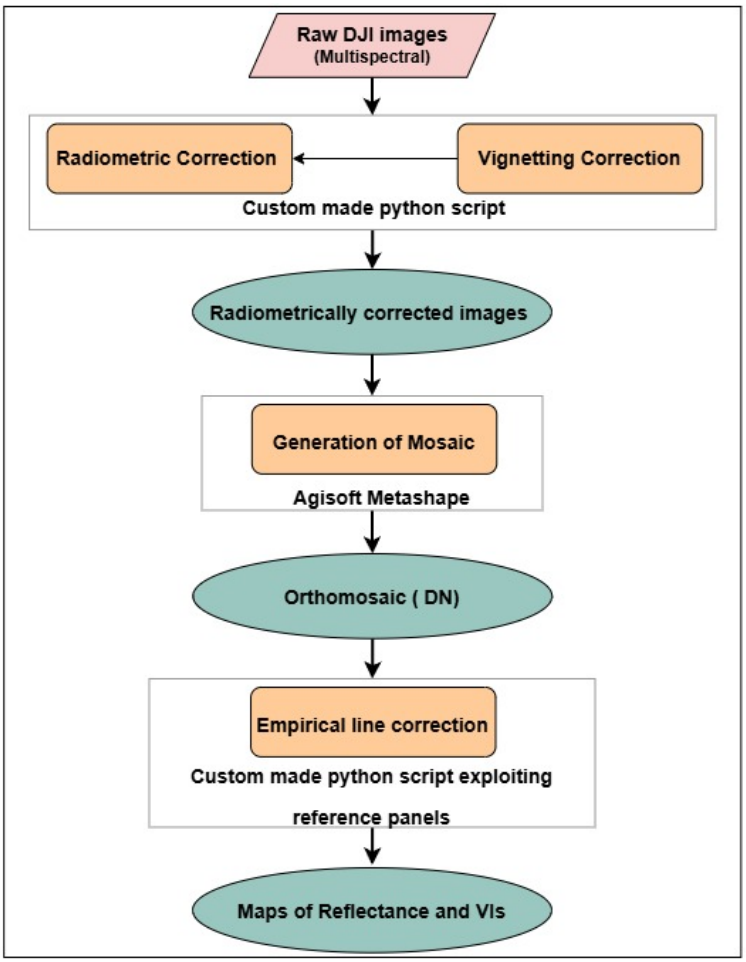

Figure 2.3: Overall multispectral UAV-image processing workflow (†)

2.2.1 Vignetting correction

Vignetting is the effect of the radial falloff in pixel values, which results in darker areas near the edges of images [201]. The vignetting effect, V(x, y), is typically modeled as a high-order polynomial (Equation 2.2). It assumes zero vignetting, V(x , y) = 1, at the image center:

$$r = \sqrt{(x - x_v)^2 + (y - y_v)^2} \tag{2.1}$$

$$V(x, y) = 1 + \alpha_1 r + \alpha_2 r^2 + \alpha_3 r^3 + \alpha_4 r^4 + \alpha_5 r^5 + \alpha_6 r^6 \tag{2.2}$$

Where r is the distance of the pixel (x, y) from the center of the vignette (x , y), which can be obtained by Equation 2.3, matrix shows the polynomial coefficients for the vignetting correction, which can be found in the EXIF/XMP metadata of the images.

$$I_{corrected}(x, y) = [I(x, y) - BL(x, y)] \times V(x, y) \tag{2.3}$$

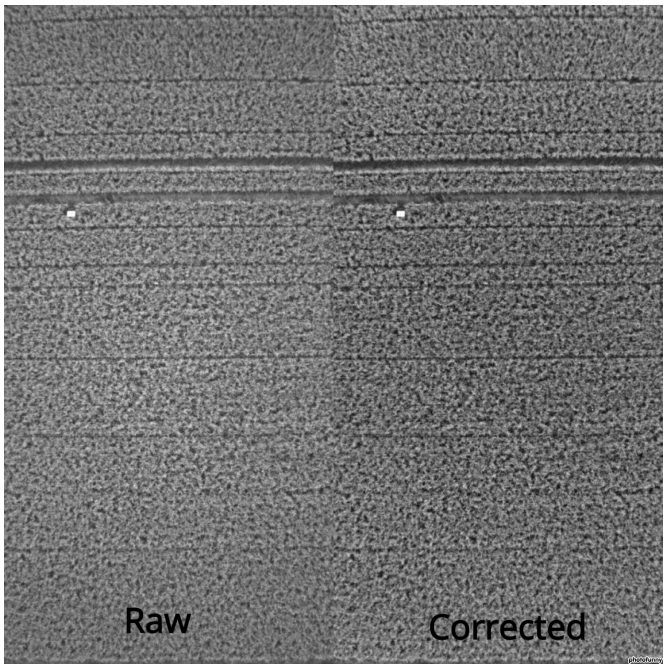

Figure 2.4: Comparison of raw (DN) and corrected ($DN_{corrected}$) imagery, displaying the effects of radiometric and vignetting corrections on image quality (*)

Where BL(x, y) is the normalized black level value, which can be found in EXIF/XMP metadata.

2.2.2 Radiometric correction (†)

The radiometric correction is a crucial step in the processing flow. When an image is captured, raw data are stored as DNs, representing the radiant energy received by each pixel. During radiometric calibration, DNs are converted to radiance and usually later the top of canopy reflectance to enable comparisons between datasets acquired under differing light conditions or with different sensors [202]. Radiance in absolute physical units cannot be calculated for DJI multispectral images as the sensor is not radiometrically calibrated by the manufacturer. Instead, normalized DNs are calculated using Equation 2.4, as described in the Multispectral Image Processing Guide provided by DJI [203]:

$$DN_{corrected} = \frac{(I_{corrected} \times 1e^6)}{\text{sensor gain} \times \text{camera exposure time}} \tag{2.4}$$

$DN_{corrected}$ is the normalized DN, and $I_{corrected}$ is the image intensity after corrections for vignetting and dark current, sensor gain, and the camera exposure time can be found in XMP/EXIF meta. Figure 2.4 clearly shows the enhanced contrast, uniform illumination, and overall data integrity achieved through vignetting and radiometric corrections.

2.2.3 Mosaic generation

The individual images, corrected as described in subsection 2.2.1 and subsection 2.2.2, were imported into Agisoft Metashape to automate the image post-processing and generate the mosaic. The software automatically recognized the characteristics of the used multispectral camera and made the necessary geometric corrections (e.g., lens distortion). As the next step, the GPS metadata of the GCPs was used for geo-positioning and photogrammetric reconstruction, and finally, the software generated the 5-band orthomosaic and digital surface model.

2.2.4 Reflectance

ELM is commonly used for atmospheric correction and for generating surface reflectance data. The method assumes a linear relationship between DNs or radiance values in an image and surface reflectance [204]. Therefore, one or more reflectance calibration panels of known reflectance and Lambertian properties must be visible in the aerial imagery to apply the method. The UAV data for this study was acquired simultaneously with nine standard reflectance panels (2%, 3%,4%,5%, 6%, 12%, 24%, 40%, and 63%). First, the reference panel ROIs were manually extracted from the central part of each panel in the orthomosaic for every flight in QGIS. Then, the reference panel measurements were obtained band by band using a Python script due to a displacement between the bands in the DJI P4 multispectral imageries. A mask was also applied for each orthomosaic within the Python script to mask out the saturated panels for each spectral band. Then, ELM was applied to the orthomosaic to create a reflectance map as described in [205].

2.2.5 Calculation of multispectral VIs

VIs allow monitoring spectral changes related to, e.g., crop structure, above-ground biomass, crop health, and weed presence [206]. The normalized difference vegetation index (NDVI) is a good indicator for green biomass, with the well-known shortcomings of saturating in closed canopies and being influenced by soil reflectance. The enhanced vegetation index (EVI) was proposed to address this issue by adjusting for atmospheric conditions and canopy background noise using a blue band. The normalized difference red edge index (NDRE) was identified as a good proxy of nitrogen concentration. The chlorophyll index red (CI-red) and the simplified canopy chlorophyll content index (s-CCCI) are often used to evaluate canopy chlorophyll and nitrogen content. The optimized soil-adjusted vegetation index (OSAVI) and chlorophyll vegetation index (CVI) are indicative of leaf chlorophyll content. Formulae and references are displayed in Table 2.1

Table 2.1: VIs used in this study and their Formulae

Index	Abbr.	Formulae	Reference
Normalized Difference Vegetation Index	NDVI	$\frac{\text{NIR} - \text{Red}}{\text{NIR} + \text{Red}}$	[207]
Normalized Difference Red Edge	NDRE	$\frac{\text{NIR} - \text{RE}}{\text{NIR} + \text{RedEdge}}$	[208]
Enhance Vegetation Index	EVI	$2.5 \times \frac{\text{NIR} - \text{Red}}{\text{NIR} + 6 \times \text{Red} - 7.1 \times \text{Blue} + 1}$	[209]
Optimized Soil Adjusted VI	OSAVI	$1.16 \times \frac{\text{NIR} - \text{Red}}{\text{NIR} + \text{Red} + 0.16}$	[210]
Chlorophyll Vegetation Index	CVI	$\frac{\text{NIR}}{\text{Green}} \times \frac{\text{Red}}{\text{Green}}$	[211]
Chlorophyll Index Red	CI-red	$\frac{\text{NIR}}{\text{Red}} - 1$	[212]
Simplified Canopy Chlorophyll Content Index	s-CCCI	$\frac{\text{NDRE}}{\text{NDVI}}$	[213]

2.2.6 Statistical Analysis (†)

A statistical analysis was performed to assess the differences between the spelt development across biochar-enriched and reference soil based on the estimated VIs. Pixel values were extracted from each treatment and its adjacent reference; see the figure for the treatments Figure 2.1 and references illustration. Given the large size of the treatment and reference patches, the number of observations (pixels) in each ROI was enormous. Therefore, traditional statistical methods could be overly sensitive to small differences. Analysis of Variance (ANOVA) and Tukey-Kramer post hoc test [214] were initially used and revealed, as expected, a significant difference at a very high level, which proved inconclusive due to the large sample size. Therefore, Cohen's d-effect size, a measure of standardized mean difference [215], was employed to quantify the magnitude of the differences between the biochar-enriched and reference plots. The effect size is interpreted using the classification developed by [215], Table 2.2

Effect size (D)	Interpretation
$0.00 \leq D < 0.20$	Ignored
$0.20 \leq D < 0.50$	Low
$0.50 \leq D < 0.80$	Medium
$0.80 \leq D < 1.30$	Large

Table 2.2: Interpretation of Effect Size (D)

2.3 Results and Discussion (†)

The EVI, serving as a proxy for vegetation health and vigor, effectively captured the temporal and spatial variations in spelt growth, development, and senescence from mid-May to mid-July 2021. The spatial maps (Figure 2.5) and boxplots (Figure 2.6) illustrate these patterns, providing comprehensive insights into the phenological development and the differential impacts of biochar and nitrogen treatments (T1, T2, T3) relative to references (R1, R2, R3) throughout the growing season.

The temporal trend of EVI aligns well with key phenological stages of spelt, including heading, flowering, grain filling, and ripening. EVI increased rapidly from mid-May to early June, corresponding to the heading stage, as the spelt head emerges and the plant reaches maximum height and leaf area. The peak EVI values observed in mid-June align with the flowering stage, as the spelt achieves maximum greenness and biomass. While EVI is expected to gradually decrease from mid-June to early July during the grain-filling stage, due to the senescence of lower leaves, EVI dropped sharply in late June. Inspection of RGB images revealed that the field was partially senescent by this time, with large portions of the spelt appearing almost yellow and dry, suggesting senescence and ripening in the field.

Visually observing Figure 2.5, treatment-related differences are most pronounced on May 15th and June 2nd. T1 consistently shows higher EVI values (green and yellow hue-red outline) compared to R1 (blue hue-white outline). T2 demonstrates lower values (blue hue-red outline), particularly on May 15th, compared to its reference (green hue-white outline). T3 exhibits consistently lower values (blue hue-red outline) than R3 (green hue-white outline). On June 14th, while differences are less pronounced, T3 still displays lower values.

The boxplots in Figure 2.6 corroborate these visual interpretations, providing a quantitative illustration of the distribution of EVI values across the biochar-enriched plots and their adjacent references. On each date except July 14th, T1 (biochar + 180kg N/ha) consistently exhibited higher EVI values compared not only to its adjacent reference (180 kg N/ha) plot but also to other treatments and

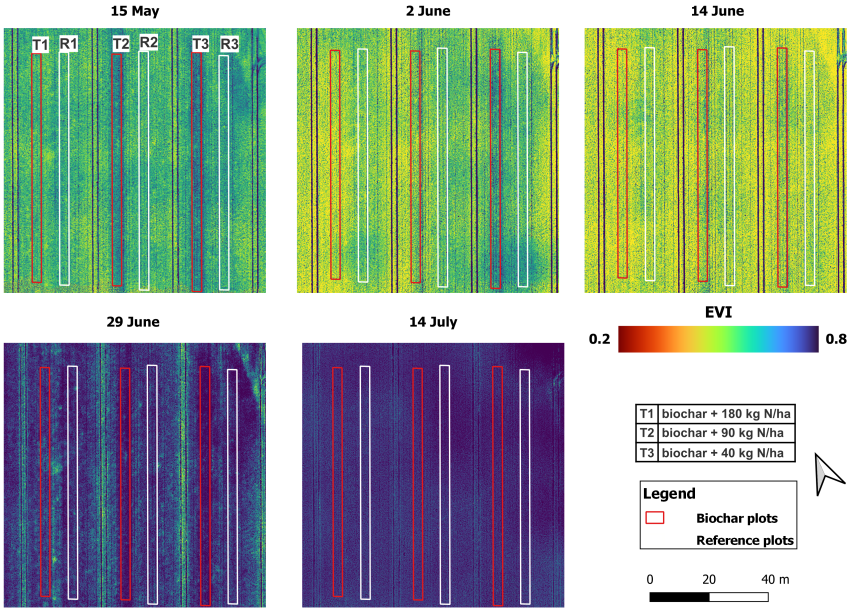

Figure 2.5: Time series of the spatial distribution of EVI in the field experiment area.

references, indicating improved crop performance with biochar and high nitrogen fertilization. Most pronounced on June 2nd, which corresponds to the early flowering emergence phase.

T2 (biochar + 90kg N/ha) revealed a variable pattern relative to R2, with lower EVI values than R2 on May 15th and June 29th, but higher on June 2nd and July 14th, and similar on June 14th. This variability suggests that biochar partially compensated for reduced nitrogen and maintained performance but not consistently throughout the growing season.

T3 (biochar + 40kg N/ha) consistently showed the lowest mean EVI values compared to all references and treatments, indicating that drastically reduced nitrogen levels negatively affect crop performance, and biochar alone is insufficient to mitigate this reduction.

The statistical analysis of VIs using Cohen's d-test effect size throughout the growing season revealed complex interactions between biochar application and nitrogen levels on spelt crop performance, as illustrated in Table 2.3. The differences between treatments and references vary over time, further indicating that the effects of biochar and nitrogen are not constant throughout the growing season. By mid-July, which corresponds to the senescence phase and occurs one day before the harvest, many of the differences between treatments had decreased, and the differences between biochar-enriched and references were negligible. This can be explained by the insensitivity of VIs to non-green vegetation (low chlorophyll content)

The comparisons between T1, T2, and T3 revealed the effects of biochar at different nitrogen levels on spelt performance. The differences between treat-

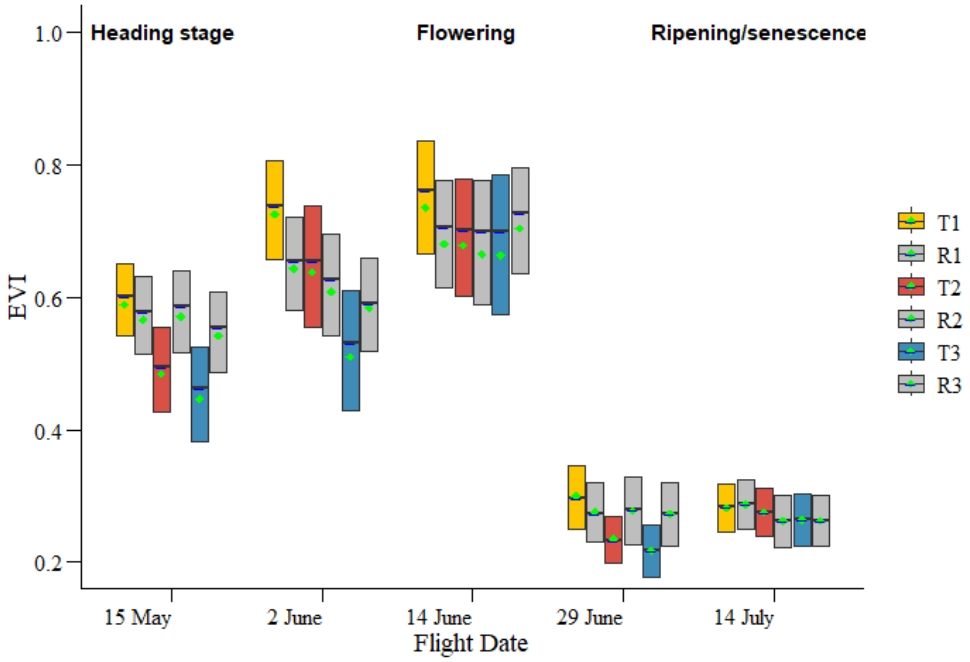

Figure 2.6: Boxplot of EVI values across the three biochar stripes versus the three reference stripes for each acquisition date. The boxes represent the interquartile range (IQR) from the 25th to 75th percentile. The black horizontal line indicates the median, while the red diamond represents the mean for each plot

ments (T1-T2-T3) were generally larger than those between treatments and reference plots, suggesting that nitrogen levels had a more pronounced effect on spelt growth than biochar alone. T1-T3 consistently demonstrated the most pronounced disparities, primarily due to the higher nitrogen fertilization in T1 compared to T3, despite both having the same biochar application. EVI exhibited the highest sensitivity to the differences between the treatments with a large effect size ($1.0 \leq d$) between T1-T3, followed closely by OSAVI. However, both indices showed weaker differentiation between the treatments on June 14th, which is apparent in Figure 2.6, with a low effect size. Interestingly, on this specific date, the indices sensitive to nitrogen content in crops, such as NDRE and s-CCCl, captured the differences between treatments with large effect sizes ($1.0 \leq d$) when the greenness indices were less sensitive. Clred and NDVI captured the strongest effect on June 2nd, revealing improved chlorophyll content of spelt in T1 (high nitrogen) compared to T3 (low nitrogen), likely during early flowering, when these indices are most sensitive to variations in canopy chlorophyll content before the potential saturation at full flowering as on 14th (maximum greenness)

Comparing biochar-enriched treatments with their respective references (T1-R1, T2-R2, T3-R3) provided insights into the effect of biochar at each nitrogen level. T1-R1 comparison showed low to medium effect sizes ($0.20 \leq d \leq 0.8$)

throughout the growing season, particularly for EVI, with T1 consistently outperforming R1. This suggests a positive effect on crop productivity even at optimal nitrogen levels. The yield data, as reported by the farmer, corroborates this finding, with T1 yielding 5% higher than the reference yield. The pronounced effect detected by EVI, followed by less significant responses from chlorophyll-related indices (such as CVI and ClRed), suggests that biochar had limited impact on chlorophyll content, potentially rather in LAI and FVC.

Interestingly, while T2 and R2 reported similar yields, suggesting biochar maintained yield with reduced nitrogen input (T2: 90 kg N/ha, R2: 180 kg N/ha), VIs revealed temporal differences between the treatments. EVI captured differences with large and medium effect sizes on May 15th and June 29th, respectively, when T2 underperformed R2, but a low effect size on June 2nd, when T2 outperformed R2. The larger effect in mid-May compared to the lower effect on June 2nd indicates that the reduced nitrogen input had a more pronounced and inverse effect on crop performance than initially assumed, and while biochar may have partially compensated for reduced nitrogen, it did not fully mitigate its impact throughout the growing season.

T3-R3 comparisons showed the largest differences between the treatments and references, further supporting the T1-T3 findings that low nitrogen in T3 led to decreased spelt development. EVI captured this lower performance on June 29th, with a large difference ($d \leq 0.8$). This finding aligns with the yield data, which indicated that T3 yielded 20% less than the reference.

2.4 Conclusion

A crucial aspect of this research was the establishment of a straightforward data processing workflow for the P4M imagery to convert raw DJI P4M image data (DN) into reflectance maps. These maps were subsequently used to estimate broadband VIs, which were employed to assess the spelt development during the growing season.

P4M-based VIs demonstrated potential in differentiating between biochar-fertilized and control patches and monitoring crop phenology throughout the growing season, as evidenced by EVI. The analysis of VIs revealed complex interactions between biochar application and nitrogen levels on spelt crop performance. Treatment 1 (biochar + 180 kg N/ha) consistently outperformed its reference, indicating a positive biochar impact at high nitrogen levels. Treatment 2 (biochar + 90 kg N/ha) showed variable performance, suggesting biochar partially compensated for reduced nitrogen input but not consistently. Treatment 3 (biochar + 40 kg N/ha) consistently underperformed its reference, demonstrating that biochar was insufficient to mitigate reduced nitrogen levels. Statistical

Index	Comparison	15 May	02 Jun	14 Jun	29 Jun	14 Jul
NDVI	T1 - T2	0.05	0.62	0.54	0.77	0.09
	T1 - T3	0.17	**1.44**	0.46	**0.98**	0.41
	T2 - T3	0.21	0.84	0.09	0.19	0.32
	T1 - R1	0.02	0.53	0.52	0.26	0.01
	T2 - R2	0.20	0.20	0.10	0.64	0.10
	T3 - R3	0.36	0.64	0.26	0.77	0.29
EVI	T1 - T2	**0.96**	0.63	0.49	**0.97**	0.13
	T1 - T3	**1.17**	**1.48**	0.32	**1.06**	0.26
	T2 - T3	0.19	0.76	0.16	0.11	0.14
	T1 - R1	0.21	0.66	0.48	0.40	0.02
	T2 - R2	0.86	0.25	0.09	0.74	0.11
	T3 - R3	0.73	0.42	0.11	**0.81**	0.02
OSAVI	T1 - T2	0.55	0.67	0.12	**1.02**	0.01
	T1 - T3	0.71	**1.18**	0.38	**1.19**	0.28
	T2 - T3	0.16	**0.84**	0.35	0.20	0.34
	T1 - R1	0.15	0.54	0.11	0.37	0.17
	T2 - R2	0.53	0.17	0.07	0.78	0.34
	T3 - R3	0.51	0.72	0.25	0.71	0.04
NDRE	T1 - T2	0.25	0.72	**0.81**	0.04	0.08
	T1 - T3	0.58	**1.01**	**0.91**	0.23	0.10
	T2 - T3	0.29	0.28	0.09	0.26	0.02
	T1 - R1	0.11	0.30	0.29	0.10	0.08
	T2 - R2	0.24	0.24	0.40	0.27	0.05
	T3 - R3	0.38	0.62	0.51	0.15	0.07
CIred	T1 - T2	0.09	0.58	0.52	0.73	0.08
	T1 - T3	0.15	**1.31**	0.42	**0.92**	0.31
	T2 - T3	0.26	0.78	0.11	0.18	0.22
	T1 - R1	0.02	0.53	0.48	0.27	0.03
	T2 - R2	0.19	0.18	0.12	0.60	0.08
	T3 - R3	0.36	0.60	0.29	0.73	0.22
CVI	T1 - T2	0.33	0.19	0.62	0.13	0.06
	T1 - T3	0.30	0.07	0.67	0.19	0.42
	T2 - T3	0.03	0.11	0.06	0.06	0.48
	T1 - R1	0.06	0.26	0.08	0.19	0.20
	T2 - R2	0.18	0.33	0.57	0.06	0.07
	T3 - R3	0.10	0.17	0.40	0.14	0.05
s-CCCI	T1 - T2	0.44	0.66	0.64	0.78	0.05
	T1 - T3	0.73	0.68	**0.83**	0.76	0.22
	T2 - T3	0.27	0.01	0.16	0.00	0.17
	T1 - R1	0.13	0.14	0.09	0.37	0.11
	T2 - R2	0.30	0.38	0.40	0.34	0.01
	T3 - R3	0.42	0.53	0.46	0.65	0.06

Table 2.3: Magnitude of difference between means for VIs comparing biochar-treated and reference plots, measured by Cohen's d; **Bold** values indicate large effects (D > 0.80) effects; Gray highlighting comparisons with the large differences mentioned in the text.

analysis and yield data corroborated these findings, showing that nitrogen levels had a more pronounced effect on spelt growth than biochar alone. The biochar

treatment showed the most indicative impact on spelt crops during the flowering emergence stage, from early to mid-June, as captured in the T1-R1 comparison. Among estimated VIs, EVI proved to be the most effective index for detecting differences between treatments and, particularly, for identifying the biochar impact at high nitrogen levels, as illustrated by the medium effect size observed between T1-R1 on June 2nd. However, the interpretation of the results could have been enhanced by incorporating additional field measurements such as yield, LAI, and chlorophyll content throughout the season.

Chapter 3

High spatial resolution imaging of solar-induced chlorophyll fluorescence (SIF) from an uncrewed aerial vehicle (UAV)

This chapter is based on the author's submitted article:

S. Salattna, J. Bendig, A. Elibol, B. Siegmann, C. Kneer, and U. Rascher, "High spatial resolution imaging of solar induced chlorophyll fluorescence (SIF) from an uncrewed aerial vehicle (UAV)," *IEEE Journal of Selected Topics in Applied Earth Observations and Remote Sensing*, submitted

The table below indicates the origin of different sections within this chapter:

Newly added (*)	**Adapted (†)**	**Original**
subsection 3.2.1, Figure 3.9, subsection 3.2.3	section 3.1, subsection 3.2.4	subsection 3.2.5 - section 3.5

3.1 Introduction (†)

The interpretation and validation of satellite and airborne-based SIF retrievals rely on the comparison with field measurements [216]. Yet, there is a scaling difference between these levels of observation that could be bridged by UAVs with sufficient signal-to-noise ratio (SNR) and geometric accuracy [217]. UAVs have the potential to acquire SIF data with high spatial and temporal resolution, recording data from 10 up to 120 m (AGL). In addition, UAVs serve as versatile and cost-effective platforms [218] at a small scale and give new avenues for further exploring the potential of SIF in precision agriculture and digital agriculture, particularly in plant phenotyping and breeding [219, 150].

To date, few studies have demonstrated the retrieval of SIF from UAV platforms. Early attempts by [220] utilized a fixed-wing UAV equipped with a thermal camera and micro-hyperspectral imager operating in push-broom mode with 30 cm spatial resolution, 1.85 nm spectral sampling interval, 6,4 nm full width at half maximum (FWHM) spectral resolution, and a wavelength range of 400-900 nm, to analyze crop water stress from orchard trees. The SIF retrieved from micro-hyperspectral significantly tracked the water stress levels, $R^2 = 0.66$ ($p < 0.001$) with water potential. However, the system had limitations due to the spectral resolution being too coarse to retrieve SIF quantitatively.

Few other studies have explored SIF retrieval using rotary-wing UAVs equipped with high spectral resolution non-imaging spectrometers. Among these, a study by [221] introduced the Piccolo-Doppio system- a dual field-of-view spectrometer system that enhances SIF retrieval with high spectral resolution (0.2 nm) and SNR (1000:1). The study described the instrument calibration procedures, and uncertainties related to SIF measurements.

Another study by [222] focused on the development and technical aspects of the HyUAS system, which utilizes a small rotary-wing UAV equipped with a non-imaging small hyperspectral (USB4000) to measure reflectance and SIF with an FWHM of 1.5 nm and spatial resolution from 0.5 to 12 m. F_{760} was estimated in this study through the 3FLD SIF retrieval method. Their study mainly tested the system, and the results showed a good agreement between HyUAS and ground-based spectral measurements for the investigated land cover.

The authors [154] conducted a comprehensive study to assess the potential of the AirSIF system, a dual-field-of-view spectroradiometer system (QE Pro) with a 1000:1 SNR and 0.8 nm FWHM, in measuring SIF from a multirotor UAV. The system performance was tested for Alfalfa (*Medicago sativa*) and grass canopies and validated against ground measurements using the same system. Sensor etaloning and platform motion correction were introduced to improve geolocation and shape reconstruction of the SIF measurements.

The innovative rotary-wing UAV system presented by [223] employs a non-imaging hyperspectral spectrometer operating (QE Pro) with 0.15 nm FWHM spectral resolution and a 1000:1 SNR for measuring F_{760}. This study focused on evaluating the system over a heterogeneous corn field and soybean/corn plots with varying nutrient treatments. The findings demonstrated the ability of the UAS-based F_{760} to distinguish plots with different crop yield potentials and showed a strong correlation ($R^2 = 0.81$) with data from a fixed SIF tower system.

The authors [150] introduced the FluorSpec system, which utilizes a non-imaging hyperspectral spectrometer (QE-Pro) operating with a spectral resolution of 0.3 nm to measure the F_{760} in the oxygen absorption bands. The system performance was tested over potato and sugar beet plants and validated against ground-based measurements. The study demonstrated the ability of the FluorSpec to measure F_{760} at ground and field levels reliably and to detect clear diurnal F_{760} patterns.

Although the non-imaging systems discussed above are able to collect high spectral resolution SIF information, the measurements are only representative of single points integrated over the canopy and do not provide information about the spatial variability of SIF. Available imaging instruments currently lack the optimal spectral resolution and SNR for SIF retrieval. Their very high spatial resolution can produce complex reflectance anisotropy patterns, complicating the interpretation of vegetation indicators [222]. Additionally, most available imaging SIF sensors are too heavy to be carried by UAVs for low-altitude flights, limiting the availability of high spatial resolution SIF measurements that can distinguish between sunlit and shaded pixels within a canopy and detect subtle variations in fractional vegetation cover [224].

Motivated by the lack of imaging UAV-based SIF systems [225] developed a novel imaging stereo-camera system (SIFcam) for the measurement of SIF in the far-red wavelength range (F_{760}) with centimeter ground sampling distance. [224] presented the first F_{760} datasets recorded by the SIFcam. The study focused on evaluating the system performance and analyzing the contribution of sunlit pixels to the F_{760} signal.

Building upon the initial methodology developed by [225], which had not yet been consolidated, this study presents two distinct workflows for the retrieval of F_{760} and generation of field-scale F_{760} maps. The first refines the previously developed approach, while the second introduces an innovative MATLAB-based method. These workflows aim to identify the method providing the best geometric and radiometric quality. To achieve this goal, the following research questions were addressed:

1. Do the developed workflows lead to F_{760} values within plausible ranges, and how comparable are these retrieved F_{760} maps with simultaneous observa-

tions recorded with reference instruments: the ground-based point spectrometer (FloX) and airborne imaging spectrometer (HyPlant)?

2. How can uncertainties in SIFcam data be measured, and how can bare soil pixels contribute to the uncertainty assessment?

3. How stable is the SIFcam when image data are acquired from a moving UAV platform?

4. How strongly is F_{760} affected by the georectification of the image data?

3.2 Materials

3.2.1 SIFcam (†)

The SIFcam system was built and developed by Forschungszentrum Jülich in cooperation with the University of Applied Science Koblenz and supported by the 'Strukturwandel- Projekt Bio¨okonomieREVIER,' which is funded by the German Federal Ministry of Education and Research. The system contains two 16-bit sCMOS cameras. Both cameras are equipped with ultra narrowband, high-quality optical filters to gain high background radiation suppression in the telluric oxygen absorption band at 760.7 nm and at 757.9 nm to measure the weak SIF signal. The cameras utilize 25 mm fixed focal length lenses that produce a field of view of approximately 41 degrees with f/1.8 aperture and near image-side telecentric properties. The system was built for ground- and drone-based field applications, featuring spatially high-resolution images and a lightweight setup. The system is described in detail in [225], where the applicability of the system was demonstrated in the lab and a controlled experimental setup. In this study, we systematically assessed the performance of the SIFcam under realistic field conditions for the first time. Figure 3.1 shows the SIFcam camera system mounted on a DJI Matrice 600 Pro UAV.

3.2.2 HyPlant(*)

HyPlant is a high-performance airborne imaging spectrometer designed specifically for vegetation monitoring and fluorescence retrieval in the atmospheric oxygen absorption bands. HyPlant was developed and built by Forschungszentrum Jülich in cooperation with Specim Spectral Imaging Ltd. (Finland). The instrument consists of two sensor modules. The DUAL module measures surface radiance in the spectral range from 380 to 2500 nm. The second module is the FLUO module, which is dedicated to retrieving SIF in the oxygen absorption bands. It acquires data in the spectral region of 670 to 780 nm with fine spectral

Figure 3.1: SIF dual-camera system mounted on a DJI Ronin MX gimbal

resolution (0.28 nm for O2-A and 0.29 nm for O2-B absorption features) and a high SNR (296 for O2-A; 442 for O2-B) [147, 148]. HyPlant enables SIF mapping at a high spatial resolution of approximately 1-4 m, which is sufficient to reveal the spatial variability between different vegetation types. HyPlant serves as the airborne demonstrator for the future FLEX satellite mission and has been used in many airborne surveys to exploit the potential of spatial SIF information for terrestrial and aquatic ecosystems.

3.2.3 FloX(*)

Spectrometer Fluorescence Box (FloX) is a hyperspectral field spectrometer system manufactured by JB Hyperspectral Device GmbH (Düsseldorf, Germany) that measures SIF under natural light conditions with a high SNR of 1000:1 [226]. The instrument consists of two spectrometers from Ocean Insight (Ocean Insight, Orlando, FL, USA): i) FLAME S, covering the full range of VNIR (400–900nm); ii) QEPro covering the red and NIR range (650–800 nm), with a higher spectral resolution (FWHM of 0.3 nm) enabling SIF retrieval in the oxygen absorption bands O_2B and O_2A, respectively. Each spectrometer consists of two fiber optics (downward and upward) to allow simultaneous measurements of the solar irradiance and target reflected radiance [226, 227, 228].

3.2.4 Data Acquisition

SIFcam data were collected on 13 June 2021 under clear sky conditions. The sun elevation angle was 38.5°, and the measured photosynthetic active radiation was 349 Wm^{-2}. The imagery was captured using a DJI Matrice Pro 600 drone equipped with a DJI Ronin MX gimbal from SZ DJI Technology Co., Ltd., Shenzhen, China. The drone followed a stop-and-go flight pattern to ensure sharp images for the 760 nm band camera. Flight settings are described in Table 3.1

Table 3.1: SIFcam setting in the field

Parameter	Value
Integration time for channel757	14 ms
Integration time for channel760	70 ms
Flight Altitude (AGL)	25 m
Ground sampling distance (GSD)	0.015 m
Side overlap	70 %
Forward overlap	80 %
Apertures focal length	f/8.0
Spatial Binning	2x2

Airborne imagery was recorded with the HyPlant imaging spectrometer [147] under clear sky conditions on June 13, 2021. The dataset was acquired at 13:46 (local time, UTC+2). The flight altitude was 350 m (AGL), which resulted in a spatial resolution of $1m \times 0.5m$ in the final maps. The HyPlant imagery was processed to derive the top of canopy F_{760} using a spectral fitting method outlined in [148].

Ground-based reference data were collected using a FloX point spectrometer (JB Hyperspectral Devices GmbH, Düsseldorf, Germany) at various locations within the field on June 13, 2021, between 10:11 and 10:46 (UTC) Figure 3.2. In total, we used ground data from 13 experimental plots (5: faba bean, 5: faba bean-spring wheat mixture, 2: spring wheat, and 2: bare soil). Three measurements were collected from each plot. Measurements were recorded at a height of 2 meters above the canopy with fibers attached to the FloX having a 25° field of view. F_{760} is referred to as "FloX-F_{760}" and was derived using the iFLD method [137]. The three measurements from each plot were averaged for further analysis.

3.2.5 Field Experiment

The research was completed at the agricultural research station Campus Klein-Altendorf in Bonn, Germany Figure 3.2. The experiment involved a field experiment of 72 plots, each plot measuring 1.5 by 3 m. These plots contained 1:1

mixtures of different spring wheat (*Triticum aestivum L.*) and faba bean (*Vicia faba L.*) varieties alongside monoculture plots of beans and wheat. Six different mixtures, including three wheat genotypes (Anabel, SU Ahab, and Sorbas) and two faba bean genotypes (Mallory and Fanfare), were compared to their corresponding single-crop plots. The objective of the experiment was to understand the contribution of the structural and functional mechanisms in the positive effects of crop mixtures [229].

3.3 Processing chain

The SIFcam generates 16-bit grayscale images in TIFF format. The proposed two distinct workflows Figure 3.3 are outlined in subsection 3.3.1 and subsection 3.3.2. The main difference between the two workflows is primarily in the sequence of image stitching relative to SIF calculation and the choice between utilizing Agisoft Metashape or an in-house mosaicking algorithm developed using MATLAB subsection 3.3.3 and subsection 3.3.4 describe the preprocessing steps, including flat field and dark-current corrections, radiometric calibration, and application of the Empirical Line Method (ELM) to convert the at-sensor radiance into Top-Of-Canopy (TOC) radiance and reflectance values. Since the SIFcam consists of two cameras with two ultra-narrowband interference filters, the acquired pair of images must be co-registered for SIF computation. Sections sub-

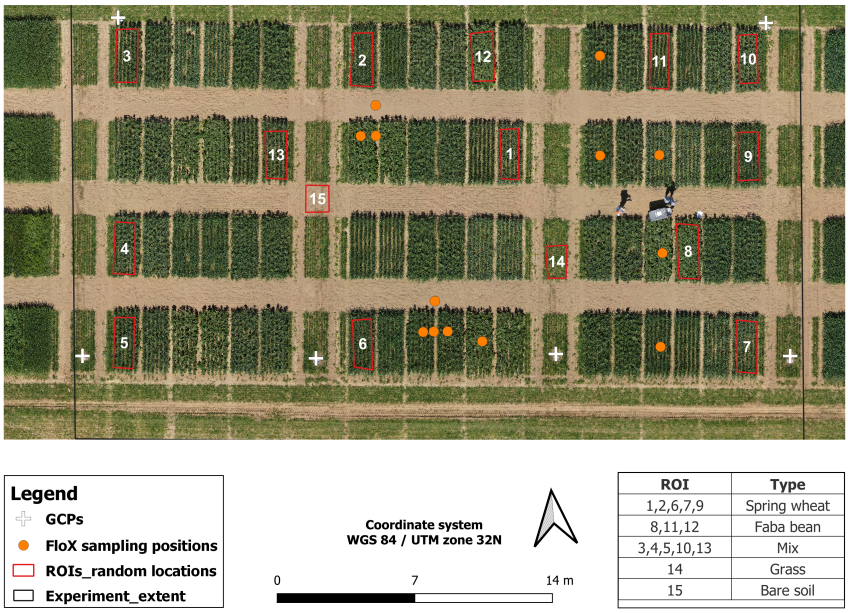

Figure 3.2: Map of the Mixed Crops experiment in Campus Klein Altendorf in Bonn, Germany. The background image corresponds to the RGB orthomosaic captured by UAV on June 14, 2021. The $\text{ROIs}_{\text{random}}$ locations (red rectangles) represent randomly selected spots for further analysis in subsection 3.4.4

section 3.3.5 and subsection 3.3.7 explain when and how both workflows perform the co-registration of the two channels and the generation of the mosaic (global alignment). subsection 3.3.6 describes SIF retrieval at 760 nm (F_{760}) using the standard Fraunhofer Line Discrimination (sFLD) method, while subsection 3.3.8 illustrates the georeferencing process.

3.3.1 Workflow 1

The first workflow (Figure 3.3) follows these steps to produce the F_{760} map :

1. Correcting the raw individual images from the two channels (C757, C760) for the dark current and flat field effect, subsection 3.3.3
2. Mosaicking the corrected images using Agisoft Metashape (1.8.1), subsection 3.3.7
3. Converting the corrected digital numbers (DN) values of the orthomosaic to at sensor radiance, subsection 3.3.3

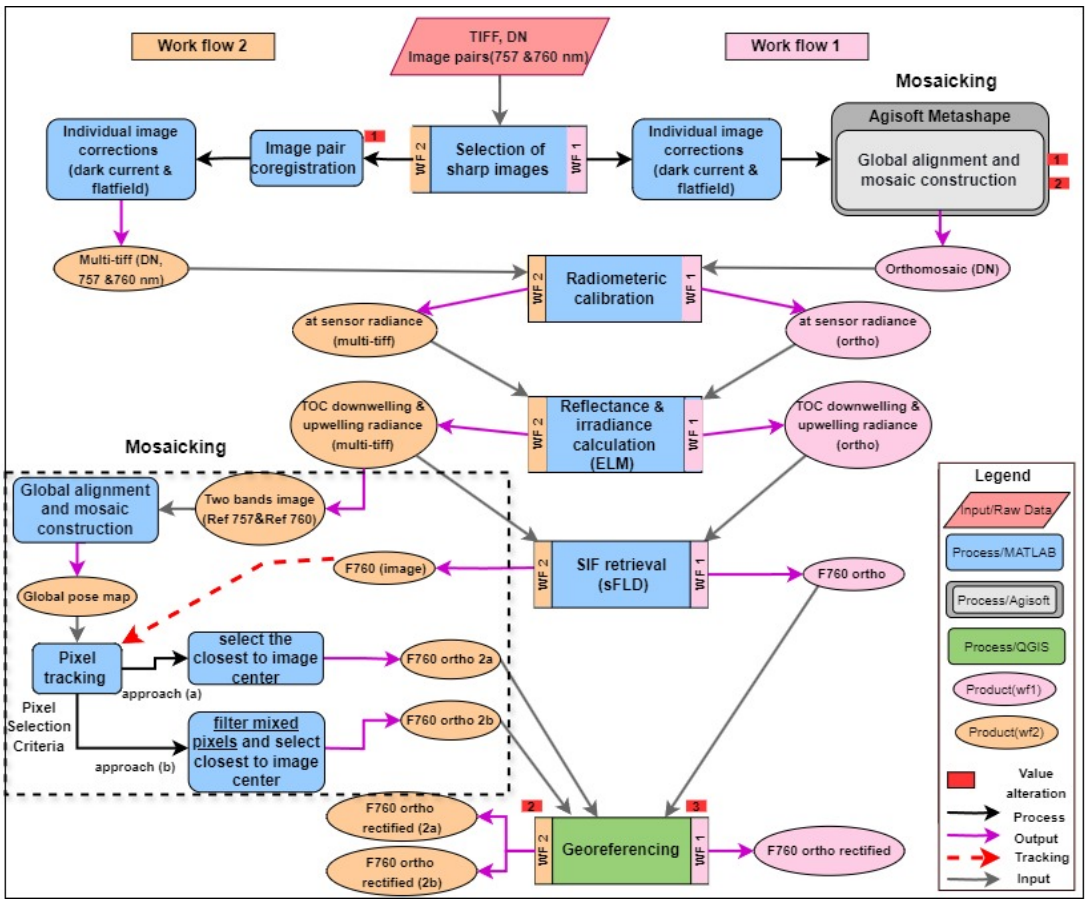

Figure 3.3: Flowchart of the SIFcam processing chain; DN: digital number, ELM: empirical line method, TOC: top of the canopy, Ortho: orthomosaic, Ref: reflectance, sFLD: standard Fraunhofer Line Discriminator

4. Computing irradiance and reflectance, subsection 3.3.4
5. Computing F_{760}, subsection 3.3.6. henceforth denoted as F_{760} mosaic 1
6. Georeferencing F_{760} mosaic 1, subsection 3.3.8

3.3.2 Workflow 2

To obtain precise F_{760} information for subsequent qualitative and quantitative analysis, we followed the image mosaicking pipeline workflow 2 (Figure 3.3) and made some modifications to compute F_{760} values at the pixel level within the final mosaic through the following steps:

1. Precise co-registration and warping of image pairs (C757, C760) to generate a single multi-TIFF image with two channels in DN, subsection 3.3.5
2. Applying the corrections outlined in subsection 3.3.3 to the individual paired images
3. Computing the radiance and reflectance at 757 nm and 760 nm for image pairs, subsection 3.3.4
4. Computing F_{760} images, subsection 3.3.6.
5. Mosaicking with an intermediate step including applying global alignment to two band images (757 nm and 760 nm reflectance), subsection 3.3.7, and using the result of this alignment, the global pose map, as a geometric framework to generate the F_{760} mosaic. Two mosaics are generated from the two used approaches (F_{760} ortho 2a and F_{760} ortho 2b).
6. Georeferencing the final mosaics, subsection 3.3.8.

3.3.3 Raw Data to At-Sensor Radiance

As SIF is measured in absolute radiance units, the first step in the processing chain involves converting the raw spectra DN to at-sensor radiance [150]. This is achieved by removing dark current (averaging dark images and then pixel-wise subtraction from the raw data), normalization by integration time, and multiplication by the radiometric calibration coefficient per wavelength. Additionally, the images were corrected for the flat field effect to reduce illumination inhomogeneities introduced by the lens, like vignetting and angle-dependent filter transmission equation (1).

$$L_{at\_sensor} = \frac{Raw_{DN}(\lambda) - Raw_{DC}(\lambda)}{IT} \times coeff_{rad}(\lambda) \times ff_{(x,y)} \tag{3.1}$$

Where L is the upwelling at-sensor radiance in mW m^{-2} sr^{-1} nm^{-1}, Raw_{DN} are DN of the raw data, Raw_{DC} is dark current, IT is integration time in ms, $coeff_{rad}$ is the radiometric calibration coefficient, and λ indicates the corresponding wavelength. Radiometric calibration data $coeff_{rad}$ was generated in the laboratory by taking images of an integrating sphere with a known, spatially homogeneous radiance output. $ff_{(x,y)}$ is the flatfield correction matrix for pixel location (x,y), also generated from the integrating sphere measurements.

3.3.4 Empirical Line Method for Radiance and Apparent Reflectance

One common approach for converting at-sensor radiance to TOC radiance (L↑ TOC) is the empirical line method (ELM) [230]. This method corrects spectral data for changes in illumination during flights as well as atmospheric effects [204]. It involves using at least two reference panels with known reflectance and Lambertian properties, which means the illumination angle does not affect the surface reflectance. A simple linear regression is established based on the average values of at-sensor radiance for pixels collected over the panel's area (ROIs) and the measured and resampled reflectance spectra of the panels obtained with a field spectrometers (ASD Fieldspec 4, Malvern Panalytical, UK). Subsequently, the linear equation determined for each wavelength (spectral band) is applied to convert the at-sensor radiance of the image pixels to reflectance. TOC irradiance (L↓ TOC) can then be calculated as TOC upwelling radiance (L↑ TOC) when reflectance equals to 1.

3.3.5 Image Registration

Image registration (or matching) is aligning the images from two or more image pairs of the same scene. It involves integrating images to create a composite view and extracting information that would be impossible to obtain from a single image. For this step is important to first co-register the two channels of the SIFcam into one single pair and then to align all the images into one higher-resolution image (mosaic image via global alignment).

In workflow 1, while Agisoft Metashape does not have a built-in function specifically for individual image pair registration, it recognizes the multispectral images as sets of inherently aligned bands captured simultaneously. Thus, the software assigns one spectral band as the master channel and uses it for global alignment, which is performed as follows:

1. Feature detection
2. Matching key points

3. Estimating camera positions.

Once this global alignment is complete, Metshape co-registers the other spectral bands using these estimated camera poses. The algorithms used for these processes are not disclosed to the public. The software allows users to control aspects of this process through limited settings like the key point limit and the tie point limit, which control the upper bound of features detected and matched to manage computational load and processing time. It also offers rapid, low-accuracy initial alignment using generic preselection to preselect likely image pairs before detailed matching. However, the exact thresholds used for considering two images as overlapping or for including an image in the alignment are inaccessible to the user. In our case, for the SIFcam data, we assigned channel 757 as the master channel because the images have more contrast than in channel 760. We performed the alignment with the highest accuracy using the default values of 40,000 and 4000 for the key and tie point limits.

In workflow 2, image registration was done using MATLAB(R20223a, Mathworks) functions from the image processing and computer vision toolboxes. We followed the conventional feature-based pairwise image registration methods that involve identifying corresponding points between two sets of local distinctive points (referred to as features) in images based on local pixel statistics or gradient differences (such as Scale-Invariant Feature Transform (SIFT) [231], Speeded Up Robust Features (SURF) [232]). This feature-based image registration was used to warp the image pairs (C757, C760) and to apply the global alignment subsection 3.3.7 including:

1. Feature detection and descriptor computation: we employed the SIFT algorithm to detect key points and create a robust representation for each.

2. Descriptor Matching: we used Euclidean distance to establish potential correspondences between the two images; matches are accepted if their Euclidean distance is less than 10% of the maximum possible distance.

3. Estimating planar transformation between image coordinate frames using the robust estimation method Random Sample Consensus (RANSAC) to minimize the impact of outliers.

The RANSAC algorithm [233] is a probabilistic method used for robust estimation of parameters. The descriptor-matching step frequently produces some mismatches. Robust estimation algorithms are used to estimate the dominant coordinate transformation, which agrees with the largest number of correspondences and rejects outliers. Outliers refer to matched point pairs that do not

conform to the transformation (relative motion of the robotic platform or camera) between the coordinate frames of overlapping images. The algorithm uses a threshold in order to decide whether a correspondence is an inlier or outlier. The threshold within our context is the distance between the corresponding feature positions when the estimated coordinate transformation is applied. In order to ensure the accurate matching between images, we use a pretty small threshold value ranging from 0.5 to 1.5 pixels.

3.3.6 Solar-Induced Chlorophyll Fluorescence Retrieval

The sFLD method for SIF retrieval relies on measuring the radiant flux at two distinct points: inside and outside a spectrally narrow absorption feature within the solar irradiance, for instance, the telluric oxygen absorption bands [133, 102]. The magnitude of SIF is determined by comparing the signal detected within the absorption feature (designated as λ_{in}, for instance, 760 nm for O_2A) with the signal recorded at a nearby wavelength (λ_{out}, for example, 757 nm), which encompasses the total solar background irradiance. This study implemented the sFLD method to retrieve the F_{760} at the O_2A band using the two wavelength bands λ_{in} and λ_{out} (760 and 757 nm, respectively).

$$SIF = \frac{Rad_{in} \times Irr_{out} - Rad_{out} \times Irr_{in}}{Irr_{out} - Irr_{in}} \tag{3.2}$$

where Irr is the incident solar irradiance, and Rad is the target radiance in λ_{in} and λ_{out} (the bottom and shoulder of the well). Equation Equation (3.2) is fulfilled if assuming that both reflectance inside ($Refl_{in}$) and outside ($Refl_{out}$) the absorption band, as well as the fluorescence inside (F_{in}) and outside (F_{out}) the band are equal Equation (3.3).

$$Refl_{in} = Refl_{out} \quad F_{in} = F_{out} \tag{3.3}$$

3.3.7 Mosaicking

A mosaic image is a composite image created by stitching images of an area of interest. Image mosaicking mainly consists of successive iterations of pairwise image matching and camera trajectory estimation (known as global alignment or registration) steps to find the transformation between every individual image coordinate frame and the selected common (or global) coordinate frame. During trajectory estimation, a predefined cost function (such as reprojection error [234], symmetric transfer error [235]) is minimized using feature point positions detected in overlapping image pairs resulting from pairwise image matching. Spatial relationships between images are crucial, constraining image positions when mapped

onto the global (or mosaic) frame. Efficiently establishing these relationships requires accurate trajectory estimation. A fundamental requirement for accurate trajectory estimation is linking the first and last images in the sequence, encompassing all intermediate images. The Initialization step is pivotal at this stage, focusing on assessing the similarity between image pairs and establishing connections among them [236]. In the mosaicking step (global alignment), the images are aligned to a unified coordinate frame. Often, in the absence of additional information, the coordinate system of the first image is used as a reference frame. In this step, pixel values are radiometrically altered, which includes resampling and interpolation to assign pixel values to the new grid location.

In workflow 1, the orthomosaic generation process in Metashape begins with the global alignment (subsection 3.3.5; once the images are aligned and co-registered, Metashape generates a dense point cloud using the depth information obtained from all spectral bands, which is later used to create the mesh. Metashape uses the camera poses derived from the master channel to project both spectral bands (757 and 760) onto the mesh surface. This step involves resampling and interpolation to adjust the pixel grid of the images to align with the geometry of the mesh, which can alter the original values. This process also involves blending images to smooth transitions between overlapping images for each spectral band, and for this, we used the average blending option. Additional geometric correction, including resampling, is performed in this step to account for any remaining misalignments between the two bands.

For workflow 2, we implemented a multi-step process in MATLAB to estimate the final image-to-map transformation to obtain a more radiometrically accurate mosaic, including:

1. Creating a two-channel image of reflectance at 760 nm and reflectance at 757 nm and converting the data to 8-bit unsigned integers (0-255 range), scaling the original values, which provides richer information for feature detection algorithms compared to Metashape, which uses one channel only. To ensure robust feature detection and matching, we established a minimum threshold of 200 detected features per image, automatically excluding any images from further analysis that did not meet this criterion.

2. Stitching the two-channel images - coarse-to-fine image matching was applied to identify overlapping image pairs, that are going to be used in employing a global alignment (subsection 3.3.7) resulting in the pose matrix, which refers to the position and orientation of the cameras in 3D space relative to a global coordinate system. This pose matrix (global pose) serves as an intermediate step for delineating overlap and geographic coordinates. The coarse-to-fine image matching initially applies image registration without RANSAC using a small number of randomly selected features, and the

image pairs that have more than 4 matched features are verified further by using RANSAC. The image pairs that have more than 14 matched features after RANSAC are used in the global alignment process, which is carried out by minimizing the symmetric transfer error over the detected feature positions.

3. Converting the pose back to 2D and using those 2D transformations to visualize the final F_{760} mosaic, while the values of the pixels in this mosaic are obtained by tracking each pixel in the global map to its corresponding location in the individual F_{760} images. Thus, the original F_{760} values were not altered in the mosaicking (due to the blending step) step because they were not used in the global alignment. Projecting the pixel coordinate on the map to the individual F_{760} images may yield multiple observations since the same real-world point might appear in different images (due to the overlap). To address multiple observations of the same pixel, we employed two distinct approaches to select one value per pixel in the final F_{760} mosaic while avoiding bending pixels and alternating original values:

   a) Approach 2a: the value in the final mosaic (F_{760} ortho 2a) is selected from the F_{760} image where the pixel's position is closest to the individual frame center. In our study, we decided to take the pixels closest to the center due to the higher spectral and radiometric quality of the inner core of the image [225].

   b) Approach 2b: This approach aims to filter out pixels that show inconsistent values across images, appearing as positive (vegetation) in some frames and negative (soil or shadow) in others due to changes in viewing angle, leaf orientation, or shading. Hence, we computed the maximum and minimum values of each pixel value across all F_{760} images where it appeared and selected the value of the pixel in the final mosaic (F_{760} ortho 2b) following this criterion:
   Pixels with maximum $F_{760} > 0$ and minimum $F_{760} > 0$ are identified as leaves or canopy and the final value was taken from the pixel closest to the center
   Pixels with maximum $F_{760} > 0$ and minimum $F_{760} < 0$ indicate a mixed pixel (leaves and soil); in this case, all the pixels with negative values were eliminated, and the pixel value closest to the frame center from the positive values was selected.
   Pixels with maximum $F_{760} < 0$ and minimum $F_{760} < 0$ are classified as soil, and the final value was taken from the pixel closest to the center.

3.3.8 Georeferencing

Sommer and Wade [237] define georeferencing as aligning geographic data to a known coordinate system, allowing it to be viewed, queried, and analyzed alongside other geographic data. A common method for georeferencing raster images is to use ground control points (GCPs) [238]. GCPs are landmarks located at well-known geographic coordinates that are used to align the raster to the coordinate system. As the SIFcam currently has no inbuilt global navigation satellite system (GNSS) sensor for geotagging, the resulting mosaic is not initially assigned to a geographic coordinate system. In our study, we employed 6 GCPs, measured with a real-time kinematic (RTK) GNSS with 10 mm horizontal and vertical accuracy for georeferencing. We applied the second-order polynomial transformation and nearest neighbor resampling using the Georeferencer tool in QGIS (3.28).

3.4 Results and Discussion

3.4.1 F_{760} Mosaics from Workflows 1 and 2

Figure 3.4 presents the three mosaics of F_{760}, labeled 1, 2a, and 2b, which give a visual impression of the results from processing the datasets with the two distinctive workflows (subsection 3.3.1 and subsection 3.3.2). The three mosaics reveal high spatial resolution F_{760} measurements with a ground sampling distance (GSD) of 1.5 cm and plausible F_{760} between 0 and 3 mW m^{-2} sr^{-1} nm^{-1}, as expected for the sFLD retrieval method. From the visual inspection, a clear spatial distribution pattern in F_{760} can be observed among the experimental plots and the rows in each mosaic, with certain rows appearing brighter, the plots in the bottom row of each mosaic reveal higher F_{760} than the third row. Also, F_{760} values varied between the three mosaics; Mosaic 2b shows a pattern of moderately higher F_{760} values than the others. Mosaic 1 exhibits the best geometric accuracy, allowing for the identification of single leaves. The rows in the mosaic appear to be consistently aligned across the images, with visible and smooth variations in pixel values. Nonetheless, noticeable striping artifacts are present in parts of the mosaic (white rectangle). While Mosaics 2a and 2b show higher value intensities compared to Mosaic 1, they reveal some artifacts and misalignments in some parts (red circles). The observed discrepancies between the three mosaics are likely due to the mosaic generation method employed. Mosaic 1 was generated with Metashape using the average blending mode, which smoothes all the pixels. Mosaic 2a and 2b were generated using the MATLAB algorithm with no blending but selecting one value for each pixel. This approach may lead to alignment issues, particularly at the edges of the mosaic, which likely originate from reduced image overlap at the experimental field margins.

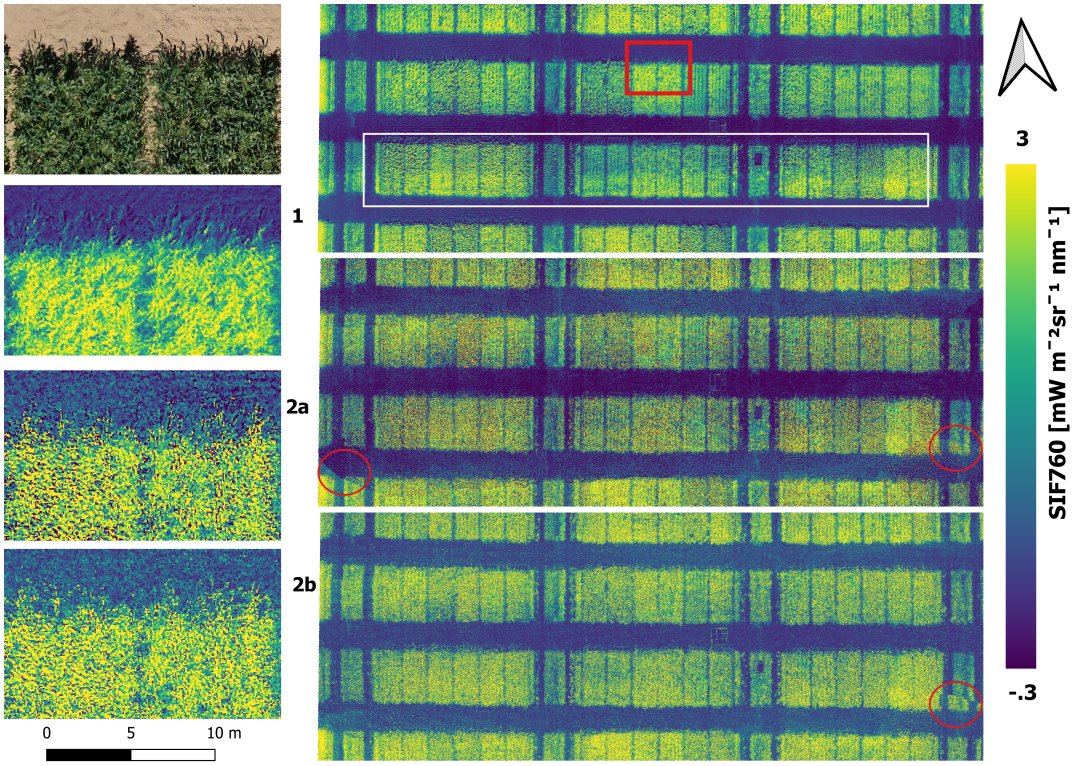

Figure 3.4: F_{760} Raster mosaics produced using different workflows. (1) Mosaic generated using workflow 1. (2a) Mosaic generated using workflow 2a. (2b) Mosaic generated using workflow 2b. The dataset presented in this figure was recorded on June 13, 2021, at 13:30 CET (solar noon), 25 m (AGL). The red rectangle in Mosaic A indicates the region selected for zooming in all three mosaics. Adjacent to each Mosaic, the corresponding zoomed-in image provides detailed views of the selected region, and on the top, a zoomed-in RGB for the same region

3.4.2 F_{760} Quality Assessment

To assess the uncertainty measurement of the F_{760} retrieval, we used the accuracy of the F_{760} retrieval of the bare soil as a reference as it is a non-fluorescent surface, with a theoretical fluorescence value of zero. We followed this approach due to the lack of known, stable F_{760} reference values similar to those of vegetation. Numerous bare soil pixels were selected and extracted from soil lines between the experimental plots from F_{760} mosaics generated using workflow 1 and workflow 2. Workflow 2b was excluded from this analysis because filtering out the mixed pixels would have significantly altered the data distribution, making it no longer normally distributed; thus, analysis using the statistical matrices could lead to biased or misleading interpretations. High positive and negative F_{760} values were observed in the soil pixels, which is likely due to the presence of small plants, such as grass, within the soil-selected area. The inclusion of these outliers would have introduced noise and potentially skewed the results. Therefore, a filtering process was applied to retain only the values within two standard deviations below

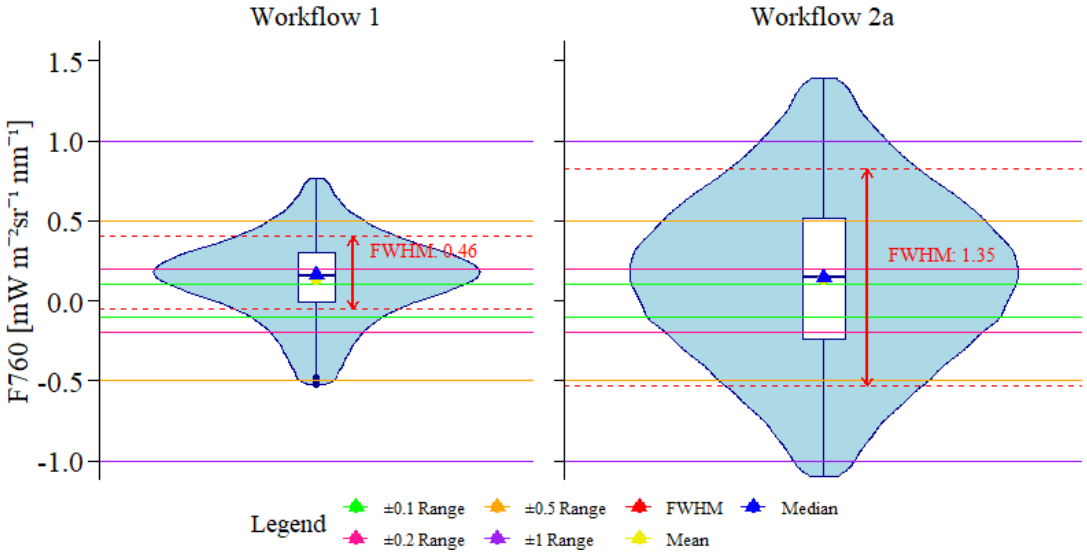

Figure 3.5: The violin plots represent the distribution of soil pixels retrieved F_{760} (mW m^{-2} sr^{-1} nm^{-1}) using workflow 1 and 2a. The boxplot overlay shows the interquartile range and the median. The mean and median values are highlighted with yellow and blue points, respectively. Horizontal lines represent deviations from 0: ±0.1 (green), ±0.2 (pink), ±0.5 (orange), and ±1.0 (purple) mW m^{-2} sr^{-1} nm^{-1}. The red arrow indicates the Full Width at Half Maximum (FWHM).

and above the mean for further analysis and visualization (Figure 3.5). Several statistical metrics were employed to assess and compare the uncertainty of the SIFcam measurements between the two developed workflows 1 and 2b, Table 3.2.

Workflow 1 violin plot with FWHM of 0.46 mW m^{-2}, sr^{-1} nm^{-1} reveals a narrow and concentrated distribution of the sensor measurements around the peak density. This observation aligns with the higher percentage of values clustered within tighter ranges around zero. The small mean positive value indicates that the sensor tends to overestimate the soil pixel values by 0.14 mW m^{-2} sr^{-1} nm^{-1}. The close values of mean and median suggest that the soil pixel values are normally distributed, as shown also by the small standard deviation (SD) and root means square error (RMSE). In contrast, the workflow 2a violin plot shows a wider spread of the data with FWHM of 1.36 mW m^{-2}, sr^{-1} nm^{-1}, consistent with lower percentages of the data points within the same ranges around zero. Still, the data is normally distributed, with the mean and median values being the same as workflow 1, but with higher variability and spread, attributed to the higher SD of 0.53 mW m^{-2}, sr^{-1} nm^{-1}. The RMSE of 0.55 mW m^{-2}, sr^{-1} nm^{-1} suggests a relatively high error, considering the theoretical value is 0. The close values of RMSE and SD indicate that the primary source of error is the variability in the sensor measurements rather than a large systematic bias. Thus, while there is some small bias (0.14), it is relatively small compared to the overall

Table 3.2: Descriptive statistics of soil pixels chosen for F_{760} quality assessment shown in Figure 3.5, RMSE: root mean square error, SD: standard deviation, MAE: mean absolute error, FWHM: full width at half maximum

Metric	Value of workflow 1	Value of workflow 2a
Median	0.16	0.15
Mean	0.14	0.14
RMSE	0.29	0.55
SD	0.26	0.53
MAE	0.28	0.45
FWHM	0.46	1.36
Percentage within ±0.1	23.24	13.54%
Percentage within ±0.2	47.08	26.86%
Percentage within ±0.5	92.53	61.38%
Percentage within ±1	100	93.51 %

error (RMSE) and not the dominant source of error. Overall, workflow 1 seems to perform better when considering a non-fluorescent surface as a reference, with almost half of the measurements being within ±0.2, which is considered to be the acceptable uncertainty for SIF measurements by the FLEX mission [111].

3.4.3 SIFcam Image Translation Stability

A crucial step in the established workflow 2 is the co-registration between each of the two corresponding grayscale images into a single pair image (subsection 3.3.5). The developed algorithm has to account for the shifts in the x and y directions and rotation differences between the images, using a transformation matrix calculated for each image pair. A transformation matrix includes tx and ty, which represent the translation distances in the x and y axes, respectively, required to move the object to a new position and the rotation angle (in degrees). To assess and evaluate the quality of this process, we derived the Tx, Ty, and rotation angle from each transformation matrix corresponding to each image pair and analyzed two aspects:

- What is the general offset between the cameras?
- How stable is this offset during data acquisition under field conditions?

From Figure 3.6, a relatively constant offset in the x and y directions between the two cameras can be seen with mean values of -17 and 25 pixels, respectively. This offset means that when warping image C760 to the master image C757, features within C760 need to be shifted on average to 17 pixels leftward and 25 pixels upward. The rotation angles fluctuate around a mean value of -0.24 degrees, so the cameras are also slightly rotated. The constant shift and rotation are intrinsic

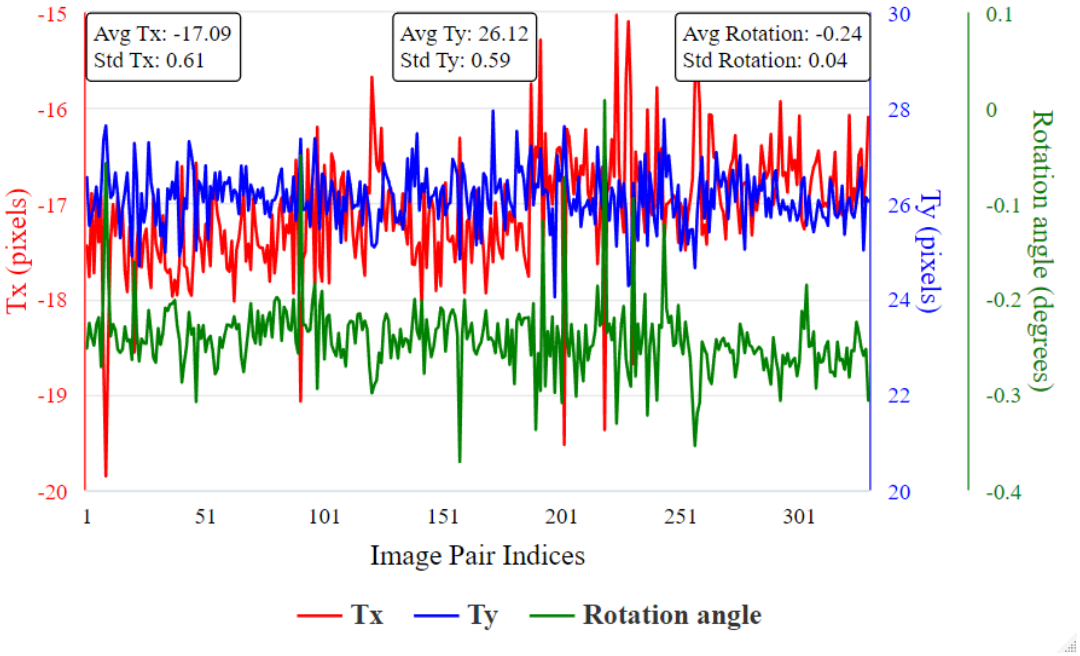

Figure 3.6: Spatial translations (in pixels) in the x and y axes and rotation angles (in degrees) derived from transformation matrices used for each image pair co-registration. The primary y-axis (red) shows the X translation, the secondary y-axis (blue) displays the Y translation, and the third y-axis(green) shows the rotation.

parameters of the dual camera array and are mostly related to manufacturing errors, such as inaccuracy in mounting the sensors onto the camera housing or inaccuracies in the machining of the frame, leading to misalignment of the sensors (not perfectly parallel). The SD was used to measure uncertainty and assess the stability of the SIFcam when mounted on a drone during flight operations in the field. The Tx and Ty fluctuate with an SD of 0.61 and 0.59 mW m^{-2}, sr^{-1} nm^{-1}, indicating small and similar instability and variation in the offset in both horizontal(left/right) and vertical(forward/backward) dimensions between the images. The rotation angle showed a minimal variation of 0.04 degrees, which can be considered negligible and unlikely to affect image alignment or analysis significantly. The observed slight instability is typically related to the altitude and movement (pitch, roll, and yaw) of the drone during data acquisition in the field. Also, the two sensors have different integration times; thus, they capture images at slightly different moments in time, leading to a minimal difference in image content for the same position. This discrepancy can lead to translation effects, where objects appear shifted or offset between images. The same results were observed over another two SIFcam flights from the same field at different heights (results not shown), which confirms that while the SIFcam has a constant shift and rotation, it is quite stable during the data acquisition over all the flight lines and that there is no bias or drift in the mounting of the single cameras in

the SIFcam frame. Extreme fluctuations or spikes can be observed at some image indices for Tx, Ty, and rotation angle, which are the images captured when the drone turns around to change the flight direction path and are not likely due to high camera vibration. The sharper peaks in the horizontal translation (Tx) compared to the vertical translation (Ty) assume higher movement of the drone around its longitudinal axis (roll) than its lateral axis (pitch) at the turning points.

3.4.4 Impact of Mosaic Georectification on F_{760} Retrieval

Georeferencing involves resampling the raster pixels to fit them into a geographic coordinate system. The pixel values are altered according to the interpolation method used and the geometric transformations performed to change the raster geometry to fit in the new coordinate system, such that the GCPs align with their true geographic locations.

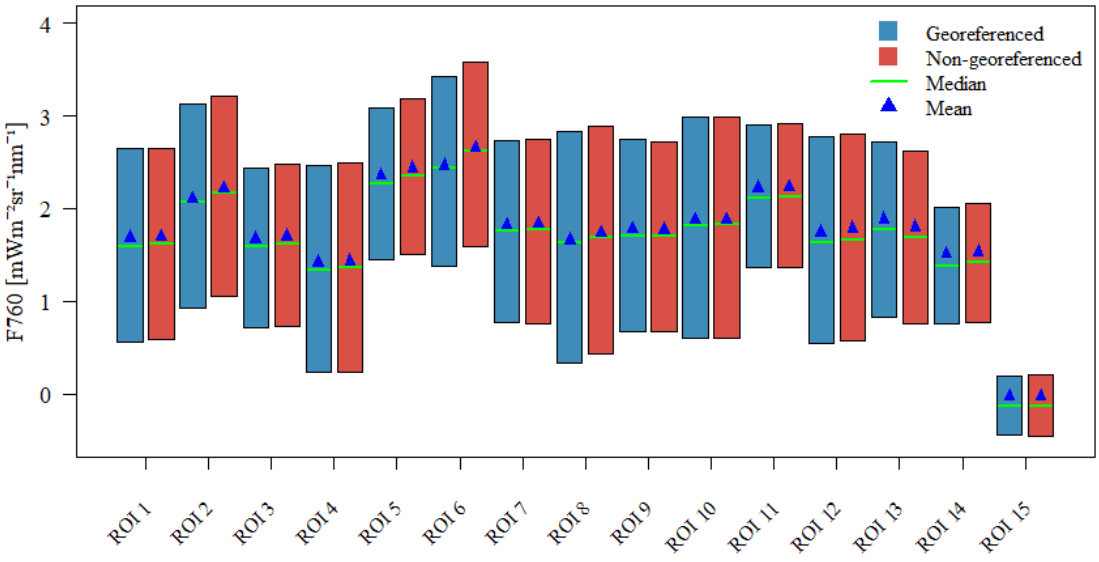

Figure 3.7: Comparison of the distribution of pixel F_{760} values in 15 ROIs (Figure 3.2) between the original raster (non-georeferenced) and the georeferenced raster from mosaic 2a. The dividing green line is the median, and the blue triangle is the mean.

To analyze and assess the impact and relevance of the georeferencing on the final F_{760} retrieval, 15 random ROIs were selected in the F_{760} mosaic 2a georeferenced and non-georeferenced. ROIs covered various crop varieties (1-13), grass (14), and bare soil (15); see Figure 3.2. The pixel values from each ROI were extracted using MATLAB. Figure 3.7 displays the distribution of the pixel values within each ROI. Visually, there is no substantial difference between the F_{760} values in the georeferenced and non-georeferenced rasters in most of the ROIs except in ROI 2,5 and 6. These ROIs cover different crop varieties and are located in different parts of the orthomosaic. Thus, no systematic pattern was observed

to elucidate the differences in these ROIs, which are possibly due to local distortions caused by the use of polynomial transformation, which anticipates a certain value alteration. Georeferencing might be less accurate in some areas because the allocation of GCPs was sparse and not evenly distributed; in particular, no GCPs were in the center of the experimental field. While Georeferencing has some effect on the F_{760} values, the effect is small and not the main driver of uncertainty, as the differences observed are smaller compared to the differences between the different ROIs (same color) due to the heterogeneity in the field, as explained in [224].

3.4.5 Validation of the Established Workflows

To evaluate and validate the accuracy and reliability of the final results of the established workflows, F_{760} derived from the three mosaics was compared against simultaneous observations by a ground-based FloX system and imagery acquired by airborne imaging sensor HyPlant.

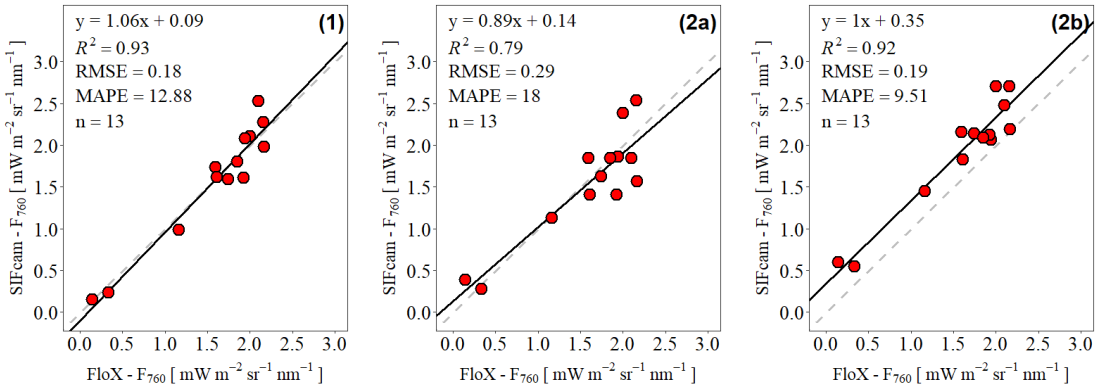

Figure 3.8: Comparison of drone-based SIFcam F_{760} against the ground-based FloX -derived F_{760}; results from 1) workflow 1 2a) workflow 2a 2b) workflow 2b. Each red dot represents the mean value of F_{760} in a 1.5 m sampling footprint. Each plot presents a linear regression analysis with the corresponding regression equation, coefficient of determination (R^2), root mean square error (RMSE), mean absolute percentage error (MAPE), and sample size (n).

In workflow 1 plot (Figure 3.8), the regression equation reveals a strong linear relationship between the SIFcam and FloX observations (R^2 =0.93). The RMSE and MAPE (0.18 and 12.88 mW m^{-2}, sr^{-1} nm^{-1}, respectively) suggest a relatively low error in the model. Workflow 2a shows a slightly weaker correlation (R^2 = 0.79) and higher RMSE and MAPE values (0.29 and 18 mW m^{-2}, sr^{-1} nm^{-1}, respectively), implying a more significant deviation from the FloX measurement. Compared to the other two workflows, workflow 2a underestimates and overestimates some of the higher SIF values, e.g., the two points at the top of the line are around 2 mW m^{-2}, sr^{-1} nm^{-1} for FloX and 2.5 mW m^{-2}, sr^{-1} nm^{-1} for SIFcam, whereas in the cluster of 8 points close by there is some underestimation, 1.5

mW m^{-2}, sr^{-1} nm^{-1} SIFcam vs 2 mW m^{-2}, sr^{-1} nm^{-1} FloX, so generally increased deviation for higher SIF values. In approach 2a (subsection 3.3.7), selecting the F_{760} value for each pixel from the closest to the center of all the images, regardless of the value of the pixel (negative or positive), might cause assigning a negative value to a canopy pixel (fluorescence pixel), which is likely explain the discrepancy in the results. The results of workflow 2b indicate a strong linear

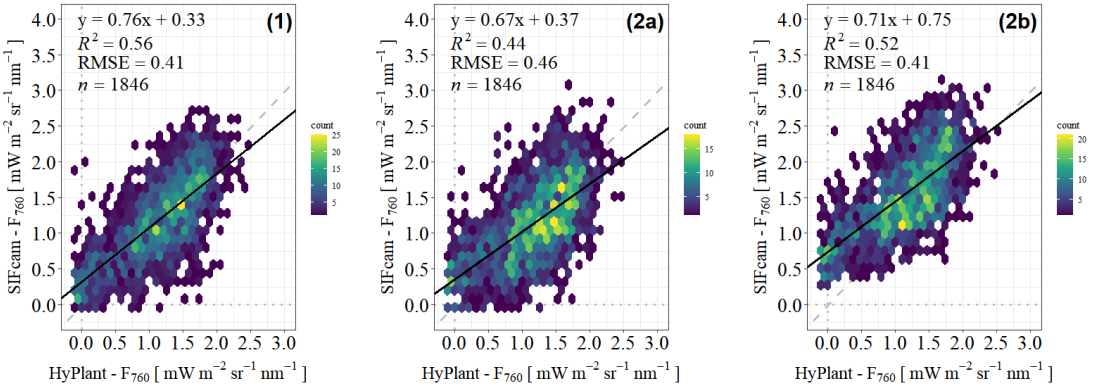

Figure 3.9: Comparison of drone-based SIFcam F_{760} against the airborne imaging spectrometer HyPlant; results from 1) workflow 1 2a) workflow 2a, 2b) workflow 2b

relationship with a slope close to 1 and (R^2 = 0.92) similar to the workflow 1 plot, albeit with a higher offset (0.35) and thus significantly biased and overestimating with the regression line above the 1:1 line. The RMSE is very close to workflow 1 (0.19 mW m^{-2}, sr^{-1} nm^{-1}) and MAPE (9.51 mW m^{-2}, sr^{-1} nm^{-1}) is lower compared to the other two workflows, revealing a higher accuracy and minimal average error of the model. The results indicate a strong influence of the pixel selection approach on analysis accuracy. The observed overestimation is likely due to masking out mixed and shaded pixels (omitting all negative values in mixed pixels, subsection 3.3.7). This is particularly evident when compared to FloX observations, where the signal is always an integration of the field of view of a 1.5 m footprint. Figure 3.9 compares F_{760} obtained from the SIFcam and the HyPlant sensor. The results from previous comparisons with FLoX align similarly here, where workflows 1 and 2b outperform workflow 2a. Workflow 2b exhibits a greater offset of 0.5 compared to workflow 1 and a tendency for overestimation. However, the correlation between F_{760} of HyPlant and SIFcam is moderate, with R^2= 0.56 and 0.52 for workflow 1 and 2b, respectively. The SIFcam map has a finer pixel resolution of 1.5 cm compared to the HyPlant maps 1 m resolution. Thus, to compare them, the SIFcam map has to be resampled and aggregated to the resolution of the HyPlant map, which alters the SIFcam original F_{760} values, particularly if the field is not homogeneous. In addition, high positional accuracy is vital for the sensor comparison to ensure that features in both datasets are correctly aligned. The HyPlant map has a precise internal image geometry and

a high absolute positional accuracy in real-world coordinates with deviations of less than 2 pixels [148], which is generally considered high for geospatial data. However, given the high spatial resolution of the SIFcam map, a 2-pixel deviation in the HyPlant might cause misalignment between the two maps, thus reducing the correlation between datasets as the features might not match up as expected, especially in this structured dataset containing small experimental plots. Further analysis was performed in QGIS to determine if there were any potential shifts or discrepancies between the SIFcam and HyPlant rasters after the resampling. Raster subtraction of the two datasets revealed that HyPlant F_{760} measurements were mostly lower compared to the SIFcam raster with a mean difference error and standard deviation of 0.1 and 0.45 mW m^{-2}, sr^{-1} nm^{-1}, respectively. The minimal mean difference error indicates that the rasters are well-aligned overall. Still, the variability (as noted in the standard deviation) can be attributed to different factors, including local misalignment between individual pixels and the noise of the SIFcam sensor. Additionally, the SIF retrieval method employed for SIFcam (sFLD) tends to overestimate SIF values [129], which can explain the higher SIFcam F_{760} compared to HyPlant (SfM SIF retrieval method).

3.5 Conclusion

This study introduced two workflows for the SIFcam dual camera system to measure F_{760} at a low flying altitude and compared their results against two other SIF-measuring systems (HyPlant and FloX). All workflows displayed statistically significant linear regressions with F_{760} measurements from both sensors, while workflows 1 and 2b performed better than 2a. Workflow 1 provided more reliable F_{760} measurements for the non-fluorescent bare soil, with values clustered closer around zero compared to workflow 2a. The observed small bias of the bare soil (mean of 0.14 mW m^{-2}, sr^{-1} nm^{-1}) in both workflows confirms SIFcam's capability of disentangling the fluorescence signal from canopy reflectance with a moderate level of accuracy and potential noise in the spectral measurements due to the high spatial resolution and thus lower signal-to-noise ratio. While workflow 1 provides less data variability than workflow 2, it uses Agisoft Metashape for mosaic generation. This powerful photogrammetry software can be considered somewhat of a black box mainly due to its limited transparency and automated processes. Metashape's internal algorithms and processing methods are not fully disclosed to users and offer limited adjustment. Meanwhile, workflow 2 employs the MATLAB computer vision toolbox, which provides a customizable photogrammetry solution in which the user has detailed insight into all the processes and decision-making methods. Our analysis revealed that in workflow 1, Metashape's approach introduces three instances of radiometric value alteration that happen during the

global alignment, mosaic generation, and georeferencing. In contrast, Workflow 2 demonstrated one less pixel value alteration by utilizing dual-band reflectance images for better accuracy global alignment and projecting the pixel coordinate on the pose map to the individual F_{760} images to get one value per pixel. Additionally, while in workflow 1 to resolve the overlapping images, the values were blended, which altered the DN values, consequently affecting the F_{760} calculation afterward, workflow 2 selected a one-pixel value for the overlapped F_{760} images and filtered the mixed pixels, thus reducing the complex reflectance anisotropy patterns (e.g., leaf orientation and shadows), which typically result from the very high spatial resolution. Our analysis showed that the georeferencing process has a small effect on the final F_{760} retrieval and is not a main driver in the measurement uncertainty. Incorporating geotagging into the camera system could eliminate this step, enhance global alignment, and further reduce the effects of georeferencing as a last processing step.

The SIFcam system mounted on a UAV showed adequate stability in collecting data on the field scale, with less than one-pixel variation in the horizontal and vertical directions, which makes the sensor a promising and well-suited tool for PA. However, it is recommended to allow for sufficient margins in flight planning to avoid limited image overlap at the edges of the area of interest. Additionally, the UAS turns at the end of the flight lines should be as smooth as possible to reduce the impact on image translation stability.

In conclusion, this study presented two image mosaicking workflows for generating F_{760} at a centimeter-level spatial scale from SIFcam imagery, attempting to fill the scale gap between the proximal and satellite measurements. SIFcam could support the calibration and validation activities of the forthcoming FLEX satellite mission as it can be deployed flexibly on the UAS while delivering unprecedented spatial details. Yet, more measurements are needed to improve the robustness of SIFcam observations and refine the developed processing chain to minimize the noise in the SIFcam mosaics.

Chapter 4

Assessing UAV-based far-red SIF and Multispectral VIs for Phenotyping different Winter Wheat Varieties

4.1 Intoduction

The Green Revolution, driven by the breeding of short-stalked dwarf genes and the substantial increase in grain yield, has fundamentally changed the cultivation of winter wheat since the 1960s [239, 240]. The consistent breeding efforts have resulted in new winter wheat cultivars with shorter plant heights, robust stems, and optimized morphological traits like more erect leaves (vertically oriented leaves), curved leaf positions, and larger flag leaves to improve light penetration in the stands of winter wheat, which improves photosynthesis and grain yield potential [241, 242]. Old tall cultivars with planophile leaves (horizontally positioned) have higher shading ability compared to the new cultivars even at the same LAI [243]. Over the past five decades, it was reported that new winter wheat cultivars exhibit better light interception and penetration deeper into the canopy, resulting in higher photosynthesis, greater crop growth, better resistance to lodging, improved nutrient utilization efficiency, and significant yield improvements [244, 245].

Previous research performed a comparative analysis of winter wheat cultivars bred before and after the Green Revolution (1950s and 2000s) using active fluorescence measurements (LIFT) throughout the growing season. This study has reported higher Fq/Fm values in the cultivars from the 2000s, named hereafter New, indicating potentially higher photosynthetic efficiency. Additionally, this

study observed higher yields and shorter plant heights in new cultivars compared to the cultivars from the 1950s, named hereafter Old. LAI measurements taken on June 2, 2021, revealed that old cultivars had higher LAI values than new cultivars [246].

Building on these findings, our study extends the application of UAV-based measurements in crop phenotyping by comparing new and old wheat cultivars through two complementary approaches. We utilize F_{760} obtained from the SIFcam alongside VIs derived from a UAV-Micasense multispectral camera system. Specifically, this study seeks to:

1. Assess the robustness and applicability of the F_{760} processing chain developed in Chapter 3 across diverse winter wheat structures.

2. Investigate the potential of SIFcam in capturing variability between new and old winter wheat cultivars through F_{760} measurements.

3. Evaluate the effectiveness of UAV-based VIs in detecting subtle differences in canopy structure and pigment content among these cultivars.

4. Compare F_{760} measurements and VIs in characterizing phenotypic variations between the old and new winter wheat cultivars.

4.2 Field experiment

This work was part of the Phenorob Central experiment, which was conducted at the experimental agricultural field station Campus Klein-Altendorf in Bonn, Germany (Latitude: 50.628122° N, Longitude: 6.9888° E). The site has an oceanic climate with an average temperature of 9.4°C and an average annual rainfall of 603 mm (Campus Klein Altendorf, n.d.). The site features an arable soil base and nutrient-rich parabrown soil with a soil number of 85-90. The experiment involved 42 winter wheat varieties. In our study, six different winter wheat varieties were investigated. Three new short-straw cultivars, namely Robigus (2003), Brompton (2005), and Alchemy (2006), and three old long-straw cultivars, namely Bersee (1951), Capelle disperse (1953), and Banco (1956). The short-straw cultivars have a more erectophile leaf position throughout the entire vegetation period, while the long-straw varieties are more planophile. Wheat was grown in four replicates in a semi-randomised block design. Each plot is 3 x 3 m and bordered on the long sides by the Julius variety. All plots were fertilized and treated with pesticides to the same extent. Figure 4.1 shows a schematic map of the experimental setup.

Nitrogen fertilization was applied using an ammonium nitrate-urea solution (AHL) with 30% nitrogen (N) three times between March and June 2021, and

Figure 4.1: Schematic structure of the winter wheat experiment in Campus Klein Altendorf in Bonn, Germany. The background image corresponds to the RGB orthomosaic captured by UAV on June 13, 2021

various plant protection measures were implemented at various stages of crop development throughout the growing season, including the application of herbicides, growth regulators, fungicides, and insecticides.

4.3 Methods and tools

4.3.1 UAVs-based data acquisition and processing

SIFcam data was collected on June 14, 2021, at 13:30 under clear sky conditions (subsection 3.2.1). Flight settings are the same as described in Table 3.1; however, the altitude for this flight was set at 20 m (AGL).

SIFcam data were processed following the established processing workflow outlined in subsection 3.3.2. However, after computing the F_{760} images generated as explained in subsection 3.3.6, stitching individual F_{760} images encountered significant misalignment issues, especially between different flight lines, indicating insufficient side overlap between images; although the flight was set to a 70% side overlap, the elimination of the blurry images compromised the overlap between the remaining sharp images. Several attempts were examined to mitigate this misalignment (subsection 3.3.7), including:

1. The reflectance of channel 757 was used for the SIFT features detection and image matching, as channel 760 was noisy.

2. In the intermediate step, the geometric frame (pose) was generated from stitching the 757 channel images, and a less strict threshold of 10 instead of 14 was used for the number of matched features between the images to be utilized in the global alignment

Nevertheless, misalignment and outliers persisted. Therefore, F_{760} was estimated for each variety from individual co-registered pair images, as outlined in workflow 2 image registration in subsection 3.3.5.

The multispectral RS imagery was acquired on June 14, 2021, using the MicaSense Dual camera system, consisting of two multichannel cameras - the MicaSense RedEdge-MX and the RedEdge-MX Blue (AgEagle Sensor Systems Inc., Wichita, KS, USA). The camera was mounted on a Ronin MX gimbal attached to a DJI Matrice Pro 600 (SZ DJI Technology Co., Ltd., Shenzhen, China). The cameras capture images synchronously across ten spectral bands, which are close to the corresponding bands of the Sentinel-2 satellite.

Table 4.1: MicaSense Dual camera system setting in the field

Parameter	Value
Flight Altitude (AGL)	20 m
Speed	7.2 km/h
Ground sampling distance (GSD)	0.014 m
Side overlap	60 %
Forward overlap	85 %
Focal length (each camera)	5.4 mm
Field of view (FOV)	47.2°

Image geotagging was achieved using a GNSS receiver on the UAV. The flight settings are outlined in Table 4.1. The flight was performed around solar noon at 13:30 (local time, UTC+2) under a cloud-free sky. A set of nine near-Lambertian panels (Mankiewicz Gebr. & Co. (GmbH & Co. KG), Hamburg, Germany) with known reflectance (ranging from dark (2%) to bright (63%)) were placed next to the field on bare soil and recorded at flight altitude to convert the radiance orthomosaic to the TOC reflectance maps during the post-processing (subsection 3.3.4).

The Raw MicaSense images (DNs) were converted to radiance as outlined in [205]. Radiance images were processed to generate an orthomosaic using Agisoft Metashape standard workflow and georectified using 7 GCPs distributed in the field. Orthomosaics were generated with mosaic default mode and exported with the highest spatial resolution (0.014 m). ELM (subsection 3.3.4) was used to convert the radiance values of the orthomosaic pixels to reflectance.

4.3.2 VIs estimation

For structural properties primarily related to LAI, EVI (listed in Table 2.1), MSR and MTVI2 were utilized. MSR offers enhanced linear relationships with vegetation biophysical properties and improved performance over NDVI in addressing saturation effects [247]. MTVI2 optimizes LAI estimation by minimizing chlorophyll content influence and has shown superior linearity with green LAI [64]. For pigment content, NDRE and the TCARI/OSAVI ratio were examined. The TCARI/OSAVI (Table 4.2) was selected for its proven accuracy in chlorophyll content estimation while maintaining relative insensitivity to canopy cover variations, even at low LAI values[248]. For pigment content, NDRE and the TCARI/OSAVI ratio were examined. The TCARI/OSAVI (Table 4.2) was selected for its proven accuracy in chlorophyll content estimation while maintaining relative insensitivity to canopy cover variations, even at low LAI values[248].

VIs were calculated from the reflectance maps using the raster calculator tool in QGIS. The band centers used in this study for computing the spectral indices were 475, 560, 668, 700, and 840 nm for the blue, green, red, red-edge, and NIR bands, respectively.

VI	Formula	Reference
TCARI/OSAVI	$TCARI = \frac{3[(R_{700} - R_{670}) - 0.2(R_{700} - R_{550})(\frac{R_{700}}{R_{670}})]}{OSAVI}$	[248]
MSR	$MSR = \frac{NIR/R - 1}{\sqrt{NIR/R} + 1}$	[249]
MTVI2	$MTVI2 = \frac{1.5[1.2(R_{800} - R_{550}) - 2.5(R_{670} - R_{550})]}{\sqrt{(2R_{800} + 1)^2 - (6R_{800} - 5\sqrt{R_{670}}) - 0.5}}$	[64]

Table 4.2: VIs used in this study. OSAVI is listed in Table 2.1

4.3.3 Field Measurements

LAI was measured non-destructively using the SunScan (Delta-T Devices, Cambridge, UK), a portable handheld device designed for measuring PAR. SunScan indirectly measures LAI in plant canopies by analyzing the transmission of PAR within the canopy. It operates based on key factors, including direct and diffuse incident light, leaf PAR absorption, canopy leaf angle distribution, solar zenith angle, and transmitted fraction of light. The Sunscan optical sensor is a light-sensitive "probe", one meter long, consisting of 64 photodiodes (PAR sensors). Whenever a reading is taken, the average PAR level from the Probe is read and

sent to a handheld PDA interface. Measurements were taken across 12 plots - third and fourth row of the experiment field (Figure 4.1) - six times in each plot on June 13, 2021. The SunScan rod was placed diagonally in the crop rows four times from the sides and parallel to the crop rows from the top and bottom. Readings were recorded from 12:30 to 12:51 local time.

Chlorophyll readings of the winter wheat varieties were made using a SPAD-502 (Konica-Minolta, Tokyo, Japan). SPAD provides a non-destructive method for indirectly estimating leaf chlorophyll content by estimating light transmittance through the leaf using two LED light sources centered at 650 nm and 940 nm, corresponding to chlorophyll absorption and non-absorption peaks, respectively. The device generates unitless SPAD readings based on the differential chlorophyll absorption of red and infrared light. SPAD readings were obtained from the same 12 plots where LAI measurements were conducted; six measurements were taken within each plot and averaged to derive a mean SPAD value. SPAD readings were converted to leaf chlorophyll content (LCC) (mass per unit leaf area, $\mu g \cdot cm^{-2}$) using the relationship proposed by [250]:

$$LCC = \frac{99 \cdot SPAD}{144 - SPAD} \tag{4.1}$$

4.3.4 Statistical Analysis

A statistical analysis was performed to assess the significance of the differences observed between old and new cultivars based on the calculated VIs and F_{760}. After extracting pixel values for each plot, the pixel data from replicates of each variety were combined into a single dataset. Given the large number of observations in each dataset, the non-parametric Wilcoxon rank sum test was employed to compare the old and new varieties; nine comparisons were performed. The p-value was adjusted using the Bonferroni method to reduce Type I error (false positives) for multiple comparisons [251]. The Bonferroni correction adjusts the significance level by dividing it by the number of comparisons performed [252] in our case ($0.05/9 = 0.00556$). This adjustment ensures that the significant results are true differences rather than statistical artifacts. Additionally, Cohen's d-effect size [215] was calculated to quantify the magnitude of the differences observed between the new and old varieties. The interpretation of effect size (D) is outlined in Table 2.2

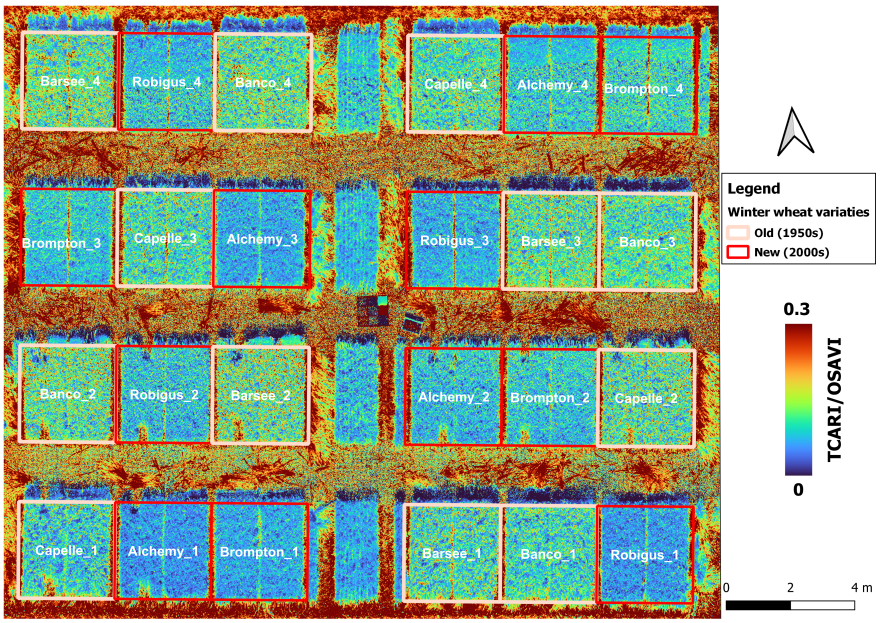

Figure 4.2: Spatial distribution of TCARI/OSAVI in the field experiment area. The dataset presented in this figure was recorded on June 14, 2021, at 13:30 CET, 20 m (AGL)

4.4 Results and Discussion

4.4.1 VIs

Figure 4.2 shows the variation of TCARI/OSAVI across the different winter wheat varieties with four replications each, arranged in experimental plots. The values range from 0 to 0.15, suggesting healthy crops with high chlorophyll content across all varieties with a distinct pattern between the winter wheat cultivars. The old varieties (Banco, Barsee, Capelle), which appear in cyan-green plots with yellow-orange patches, show higher values in all the replicates compared to the new varieties (Robigus, Alchemy, and Brompton).

The boxplots in Figure 4.4 illustrate the distribution of F_{760} values across six winter wheat varieties, categorized into new and old cultivars, revealing consistent results with the visual interpretation mentioned above. The new cultivars consistently show lower TCARI/OSAVI values (0.04-0.08) compared to the old cultivars (0.07-0.13). Given the inverse relationship between TCARI/OSAVI and chlorophyll content, this suggests enhanced chlorophyll content in the new cultivars. This observation is ascertained by the LCC measurements as shown in Figure 4.3. New varieties exhibited higher LCC values (49-53 µg·cm^{-2}) compared to old varieties (43-47 µg·cm^{-2}).

Distinct variations in data distribution and dispersion among the boxplots (Figure 4.4) can be observed, reflecting differences in canopy architecture. The canopy heterogeneity seems to be more pronounced in the old varieties, indicated

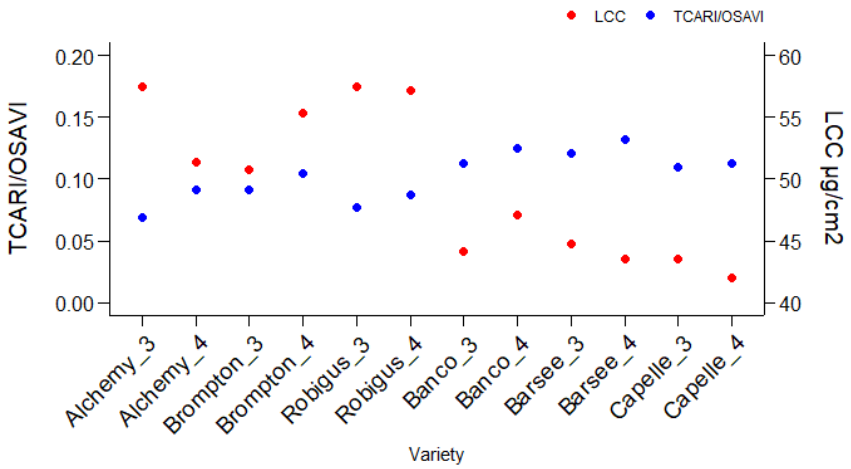

Figure 4.3: Sensitivity to chlorophyll variability of TCARI/OSAVI. Chlorophyll content was estimated from SPAD measurements conducted in the field on June 13, 2021

by larger interquartile ranges in the boxplots, which can be due to their taller statue and more diverse canopy structures; thus, spectral signatures contain a mixture of vegetation, shadows, and soil reflectance. In contrast, the new varieties cluster tightly (compact boxplots); their short straw, dense, and uniform canopy coverage explains these homogenous spectral values among the plots.

To gain insights into the structural differences between the varieties, MTVI2 was selected due to its best linear correlation with LAI ($R^2 = 0.83$) compared

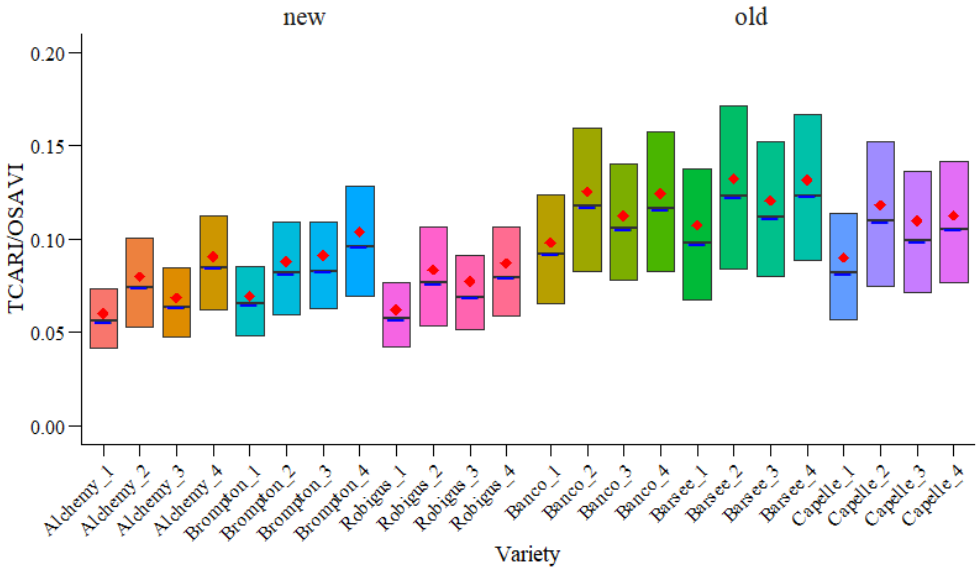

Figure 4.4: Boxplot of TCARI/OSAVI values across different winter wheat varieties. The boxes represent the interquartile range (IQR) from the 25th to 75th percentile. The blue horizontal line indicates the median, while the red diamond represents the mean for each variety.

Variety	$Brompton_3$	$Brompton_4$	$Alchemy_3$	$Alchemy_4$	$Robigus_3$	$Robigus_4$	$Barsee_3$	$Barsee_4$	$Capelle_3$	$Capelle_4$	$Banco_3$
LAI	6.33	7.3	7.63	7.38	6.8	7.1	7.38	7.72	7.43	8.83	7.18

Table 4.3: LAI of winter wheat cultivars measured in the field using SunScan on June 13, 2021

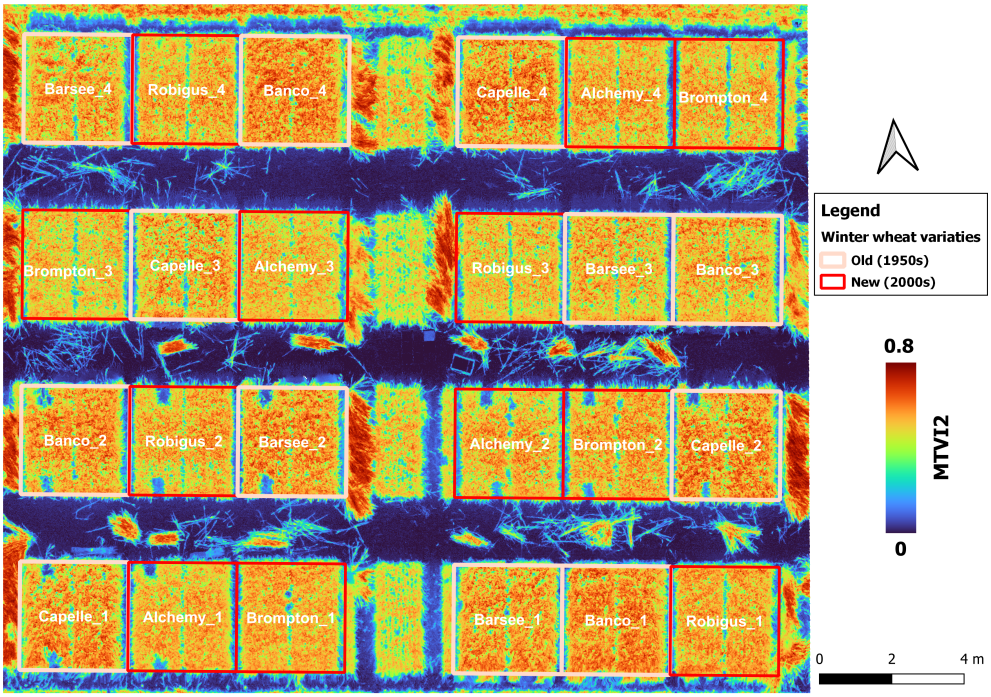

Figure 4.5: Spatial distribution of MTVI2 in the field experiment area. The dataset presented in this figure was recorded on June 14, 2021, at 13:30 CET, 20 m (AGL)

to other structure-related VIs (Figure 4.6). The spatial map (Figure 4.5) shows a less pronounced pattern, with all plots revealing high MTVI2 values (0.4-0.8) marked by yellow-orange color, implying robust vegetative growth across all varieties. Slightly higher values can be seen in the old varieties, with red-orange patches clearly visible in Banco and Capelle. The boxplot analysis (Figure 4.7) further elucidates these differences, showing higher MTVI2 values and greater heterogeneity in old cultivars (0.45-0.63) compared to new ones (0.45-0.6), suggesting higher LAI in the old cultivars. These findings align with previously reported higher LAI values in old winter wheat cultivars despite less pronounced variations in our in-situ LAI measurements.

The higher median values compared to the mean across all boxplots reflect uniform, dense canopy structure across most of the experimental plots areas with sparse areas with spectral signatures (low NIR reflectance or high red reflectance) likely due to less dense canopy or gaps —particularly apparent in old varieties, as mentioned before, due to their taller stems, resulting in the observed skew in the statistical distribution of values in the boxplot.

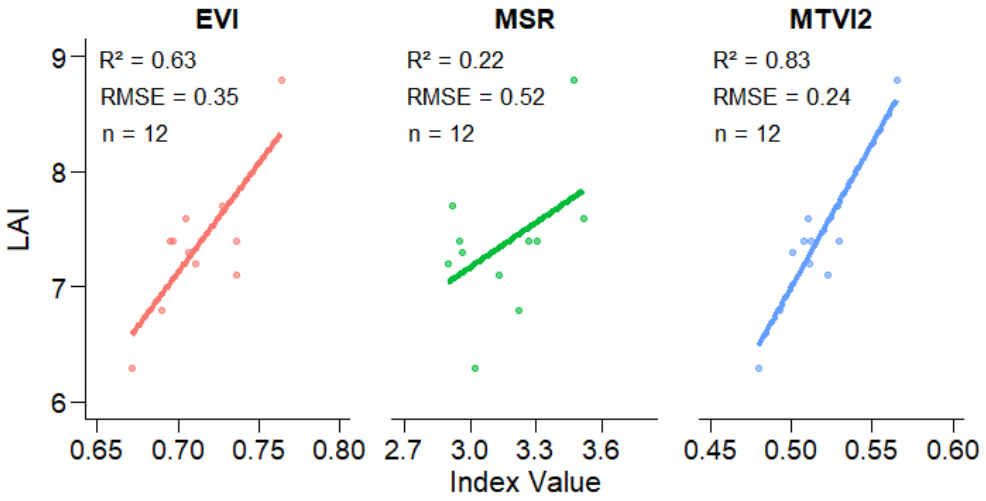

Figure 4.6: Relationship between in-situ measured and three structural-related VIs (EVI, MSR, MTVI2). Each plot presents a linear regression analysis with the corresponding regression equation, coefficient of determination (R^2), root mean square error (RMSE), and sample size (n)

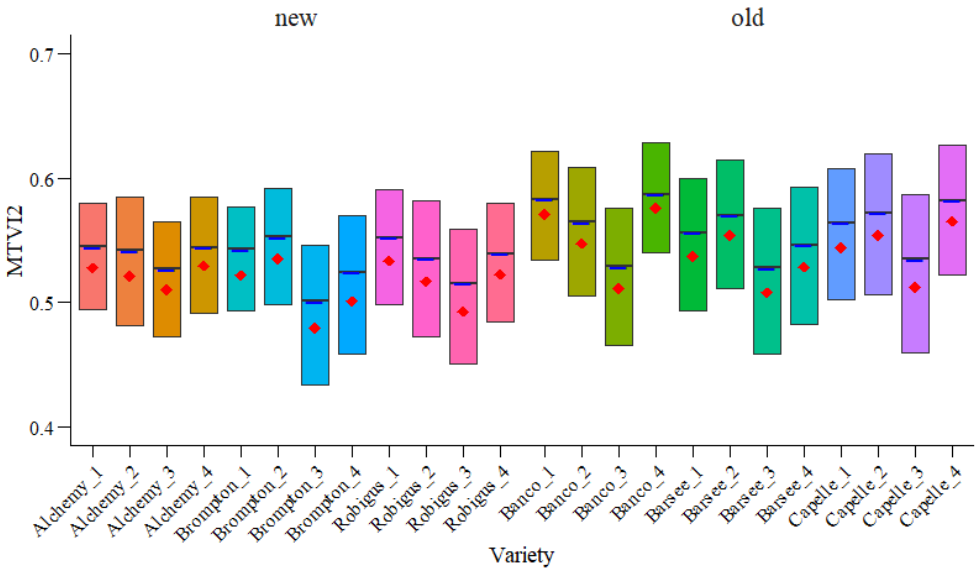

Figure 4.7: Boxplot of MTVI2 values across different winter wheat varieties. The boxes represent the interquartile range (IQR) from the 25th to 75th percentile. The blue horizontal line indicates the median, while the red diamond represents the mean for each variety.

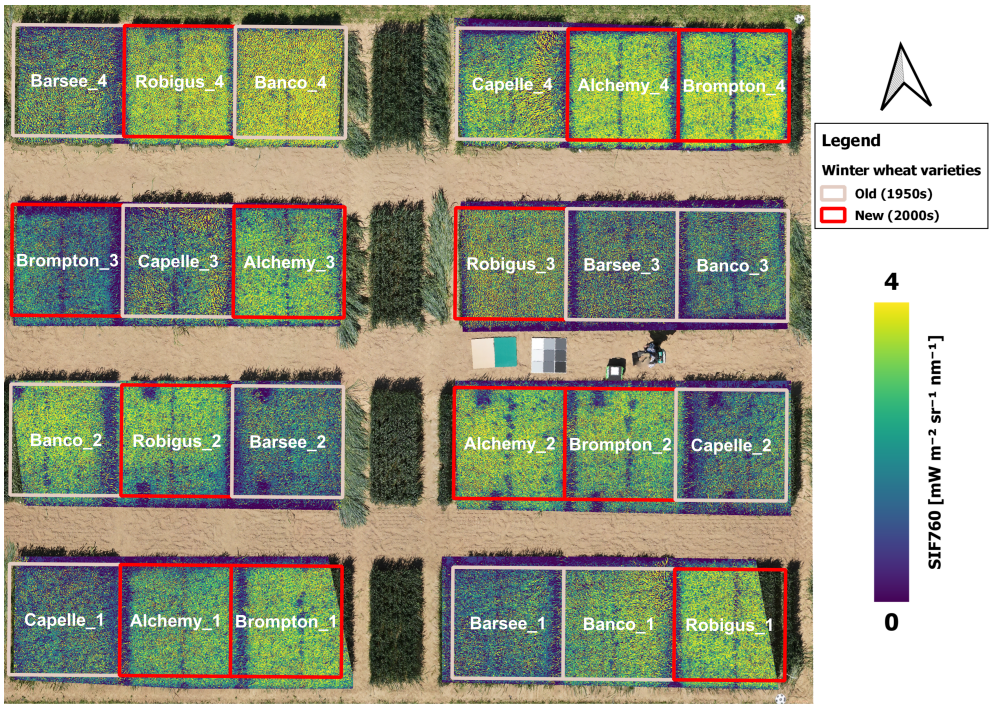

Figure 4.8: F_{760} individual rasters generated using workflow2. The dataset presented in this figure was recorded on June 14, 2021, at 13:30 CET (solar noon), 20 m (AGL). Background image corresponds to RGB orthomosaic of the experiment field (Figure 4.1)

4.4.2 F_{760}

Figure 4.8 display the spatial distribution of F_{760} measurements, with a wide value range (0-4 mW m^{-2}, sr^{-1} nm^{-1}), indicating significant heterogeneity in the fluorescence signal between the varieties in the field. Generally, new cultivars exhibited higher F_{760} (intense yellow plots, red outlines) relative to the old cultivars (blue hues, white outlines). Notable discrepancies were observed in the old cultivar Banco4, which showed high F_{760} compared to other old cultivars, and the new cultivars Robigus3 and Brompton3, which displayed comparatively lower F_{760} than other new cultivars.

The results in Figure 4.9 reveal distinct variability between and within these groups. New cultivars generally exhibit higher F_{760} values compared to the old cultivars Barsee and Cappelle, with notable variations among individual varieties and replicates. Among the new cultivars, Alchemy consistently shows the highest F_{760} values across all replicates, with mean values ranging from 2.3 to 2.5 mW m ^{2} sr ^{1} nm ^{1}. In contrast, Brompton and Robigus showed higher variability between the replicates, with Brompton3 and Robigus3 displaying the lowest values among the new cultivars, comparable to or lower than certain old cultivars. Among the old cultivars, Banco stands out with F_{760} comparable to or even exceeding some new cultivars, mostly pronounced in Banco4, with the highest mean value of 3.7 mW m ^{2} sr ^{1} nm ^{1} across all varieties.

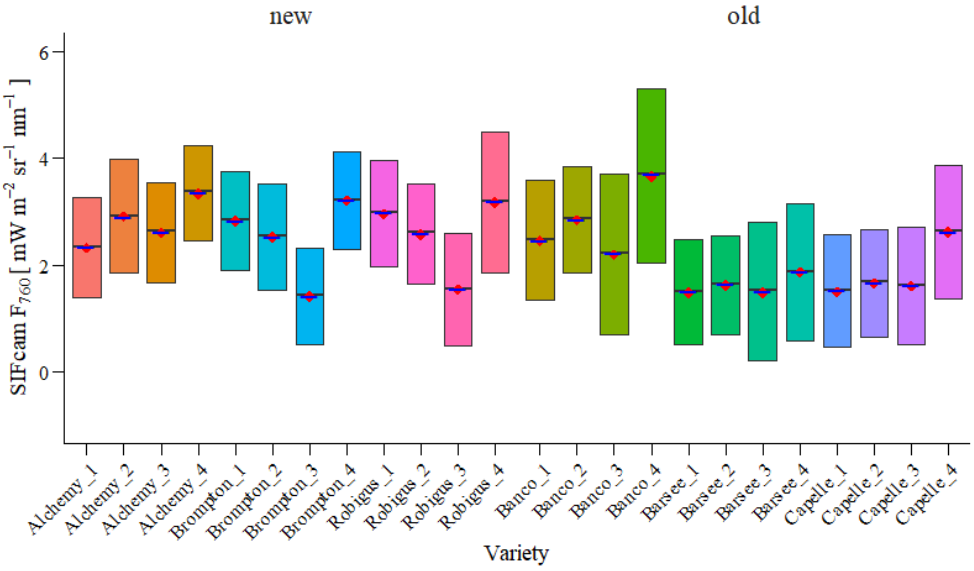

Figure 4.9: Boxplot of F_{760} values across different winter wheat varieties. The boxes represent the interquartile range (IQR) from the 25th to 75th percentile. The blue horizontal line indicates the median, while the red diamond represents the mean for each variety. F_{760} was filtered using $\pm$2SD to mask outliers.

The observed patterns in F_{760} emissions can be attributed to the interplay between chlorophyll content and canopy structure, specifically leaf angle orientation. New cultivars, characterized by higher chlorophyll content and erectophile leaf orientation, allow for better light penetration and distribution deeper into the canopy, resulting in higher photosynthetic efficiency and potentially higher SIF emission at the leaf level. However, erectophile leaf orientation increases the reabsorption of the emitted SIF within the canopy, reducing the probability of SIF escaping and potentially reducing the detected TOC SIF as in Robigus3, which demonstrates the lowest F_{760} values among new cultivars, despite having the highest chlorophyll content overall (see Figure 4.3)

Conversely, old cultivars with planophile leaves intercept more light at the top of the canopy and shade the lower leaves, leading to lower overall photosynthetic efficiency and lower SIF emission at the leaf level. Nevertheless, planophile leaves allow for a higher escape probability of SIF photons, potentially resulting in higher TOC SIF to be detected despite lower chlorophyll content. As pronounced in Banco4, which is likely due to the combined effect of its relatively high chlorophyll content (for an old cultivar, see Figure 4.3) and planophile leaf structure.

4.4.3 Statistical analysis

The statistical analysis using the Wilcoxon rank sum test with Bonferroni correction of VIs revealed significant differences ($p < 0.0056$) between old and new

New	Old	TCARI/OSAVI		NDRE		EVI		MSR		MTVI2		F_{760}	
		d	Effect	*d*	Effect	*d*	Effect	*d*	Effect	*d*	Effect	*d*	Effect
Alchemy	Capelle	0.73	**	0.59	**	0.13	-	0.13	-	0.24	*	0.60	**
Alchemy	Barsee	**1.0**	***	**0.99**	***	0.06	-	0.65	**	0.11	-	0.77	**
Alchemy	Banco	**0.89**	***	0.78	**	0.39	*	0.65	**	0.33	*	0.01	N/S
Brompton	Capelle	0.40	*	0.14	-	0.22	*	0.26	*	0.36	*	0.43	*
Brompton	Barsee	0.68	**	0.49	*	0.16	-	0.24	*	0.24	*	0.59	**
Brompton	Banco	0.56	**	0.30	*	0.46	*	0.24	*	0.45	*	0.14	-
Robigus	Capelle	0.64	**	0.40	*	0.12	-	0.14	-	0.29	*	0.43	*
Robigus	Barsee	**0.90**	***	0.76	**	0.05	-	0.36	*	0.17	-	0.58	**
Robigus	Banco	**0.80**	***	0.57	**	0.36	*	0.36	*	0.38	*	0.11	-

Table 4.4: Statistical differences between new and old winter wheat varieties based on VIs and F_{760} measurements. Values represent pairwise comparisons using Cohen's d effect sizes. Effect size interpretation: - (negligible), * (small), ** (medium), *** (large); N/S: not significant, **Bold** values indicate large effects (D > 0.80)

wheat cultivars (results not shown). Cohen's d effect size analysis of the observed variations between varieties varied considerably between the parameters (Table 4.4). TCARI/OSAVI and NDRE, both related to chlorophyll content, demonstrated the most pronounced differences between the new and old varieties. TCARI/OSAVI exhibited medium to large effect sizes (0.50 d 1.00), except for Brompton-Capelle, which showed a small effect size (d = 0.40); Alchemy-Barsee comparison revealed the largest effect (d = 1.00). NDRE followed a similar pattern, albeit with slightly weaker overall effects. The Alchemy-Barsee comparison again displayed the largest effect (d = 0.99), while the Brompton-Capelle comparison showed the lowest effect (d 0.20). In contrast, EVI comparisons, while statistically significant, showed weaker differentiation between new and old varieties. Effect sizes ranged from low to medium, with six comparisons showing negligible effects. This reduced sensitivity can be attributed to EVI being sensitive to both LAI and chlorophyll content, as evidenced by its moderate correlation with LAI ($R^2 = 0.63$) (Figure 4.6).

MSR showed improved results compared to EVI, but its sensitivity to chlorophyll content rather than LAI was evident in its weak correlation with LAI ($R^2 = 0.22$). The highest impact was observed in the same comparisons (Alchemy-Barsee and Alchemy-Banco) that showed the highest effect sizes in TCARI/OSAVI and NDRE, further confirming the sensitivity of MSR to chlorophyll content variations between varieties. MTVI2, while exhibiting smaller effect sizes compared to MSR, demonstrated a clear relationship to LAI rather than chlorophyll. This

was evidenced not only by its strong linear relationship with LAI ($R^2 = 0.83$) but also by its reduced variation in comparisons that showed high chlorophyll-related differences. These findings align with previous research indicating MTVI2's lower sensitivity to chlorophyll effects and enhanced linearity with LAI [64, 247].

Wilcoxon rank sum test For F_{760} revealed significant differences ($p < 0.0056$) in all comparisons between the varieties except between Alchemy and Banco. Moderate to large effect sizes were observed when comparing new cultivars to Barsee (d = 0.58-0.77) and Capelle (d = 0.43-0.60). These results align with differences in chlorophyll content as indicated by TCARI/OSAVI and NDRE indices, which showed larger effects between new cultivars and Barsee compared to those between new cultivars and Capelle. Interestingly, F_{760} exhibits negligible difference when comparing new cultivars with the old variety Banco (d = 0.01-0.14), an effect that is not observed when comparing chlorophyll content by means of TCARI/OSAVI. The MTVI2 analysis revealed the highest difference in canopy structure between Banco and new cultivars, indicating Banco's canopy structure differs more significantly from that of new cultivars compared to Barsee and Cappelle. This observation implies that the high F_{760} from Banco is related to its canopy structure specifically, demonstrating that additional information on plant productivity could be gained from F_{760} observations in this experiment.

Chapter 5

Discussion

Chapter 2 of this thesis focused on exploring the capabilities of a small-scale, high spatial-resolution UAV system, DJI Phantom 4 Multispectral (P4M), in monitoring short-term biochar effects on spelt crops throughout the growing season in terms of crop growth. A crucial aspect of this research was the establishment of a processing workflow for the P4M imagery, initiated by the lack of standardized processing tools for the non-radiometrically calibrated P4M system. The workflow integrated open-source Python codes for the pre-processing of raw images and post-processing of the mosaic (DN), which provided an accessible method to customize the processing pipeline, potentially benefiting other researchers encountering similar challenges. The workflow was successfully employed to convert raw DJI P4M image data (DN) into reflectance maps. These maps were subsequently used to derive broadband VIs, which were utilized to assess the vegetation development.

P4M-based VIs showed potential in differentiating between the spelt performance across biochar-fertilized and reference soil and monitoring crop phenology over the growing season. EVI proved to be the most effective index for detecting the impact of biochar treatment on spelt crops and was most evident during the flowering emergence stage. This observation aligns with findings by [200], who reported that the effect of biochar on crop development is most evident during the green-up phase. Higher EVI values in biochar-enriched plots with full fertilization (180 kg N/ha) indicated enhanced vegetative growth compared to the reference plot and likely increased leaf chlorophyll content and LAI. However, this effect was less pronounced or inconsistent at reduced nitrogen inputs. The moderate effect sizes of the differences observed likely indicate that the impact of biochar was attenuated due to the experiment being conducted on non-marginal soil under a common nitrogen fertilizer regime. This result corroborates the findings of [198], indicating that biochar likely improves crop production in highly degraded and nutrient-poor soils, while its application to fertile and healthy soils does not

always increase crop yield.

Nevertheless, the interpretation and comparative analysis of our results were constrained by the lack of UAV data from the early growth stages and field measurements. Therefore, to provide a more comprehensive dataset for analyzing biochar effects on crop development, allowing for better interpretation of UAV-derived VIs, it is recommended to:

1. Begin data acquisition in the green-up phase (late February to early March) for winter-sown spelt, with more frequent data acquisition (weekly or bi-weekly) to capture critical phenological stages and differences between treatments.

2. Optimize the experimental setup by implementing well-defined treatment areas, including pure biochar treatments at multiple rates (low, medium, high), control plots with no amendments, conventional fertilization, and combined biochar and fertilizer treatments.

3. Conduct additional quantitative field measurements through the growing season, including chlorophyll content, LAI, plant heights, and yield upon harvest.

The study revealed some challenges in DJI image processing due to spatial misregistration between the five spectral bands in the final mosaic, potentially arising from differences in sensor integration times, camera calibration issues, or multispectral image coregistration in Agisoft Metashape. However, developing a method to correct this misalignment was beyond the focus of our research, so we attempted to mitigate this issue by applying band-to-band ELM. Yet, [253] have also addressed the same spectral band misalignment issue in DJI P4M imagery processed with the Agisoft Metashape standard multispectral processing workflow where they found an average alignment error of 2.0–2.84 cm. They developed an alternative processing method that significantly improved alignment accuracy (average error: 0.2 -0.32 cm.). Their approach involves aligning images and camera calibration of each spectral band as separate chunks (which means processing images separately for each spectral band), merging all five spectral band chunks into a single chunk, performing camera re-optimization on the merged chunk, and then individually processing each chunk to generate five separate orthomosaics, and finally stacking the mosaics using ENVI software.

While the DJI P4M system offers accessibility and user-friendly features, its application in vegetation research is not highly recommended. The lack of radiometric calibration and the spectral band misalignment add extra processing, which can introduce significant uncertainties and complexity to the workflow and data analysis, potentially compromising the accuracy and reliability of VIs. [254]

reported that the P4M presents challenges regarding the radiometric correction process; the percentage error in P4M-based VIs ranged from 21.8% to 100.0% using the basic DJI Terra software v. 1.0 without radiometric calibration, compared to 11.9% to 29.5% with radiometric calibration using ELM and the calibration tool in DJI Terra software v. 2.0. He also reported that the best radiometric calibration achieved was using the ELM based on a set of reference panels acquired at the time of flight compared. A subsequent study by [255] further highlighted the P4M's limitations in deriving reliable reflectance values and NDVI. While reflectance differences between bands across orthomosaics from consecutive days were minor (up to 4%), NDVI discrepancies increased significantly (up to 15% mean difference and 7% standard deviation). Comparisons with the MicaSense Altum AL0 reference camera raised significant reliability concerns with NDVI differences as high as 47% on one day.

Chapter 3 focused on extending the application of the novel far-red SIF imaging sensor, SIFcam, to field-scale measurements. This study refined and built upon the newly established SIFcam methodology by [225] through a detailed description of a data processing workflow using the software Agisoft Metashape and introducing a new, fully customizable, approach for generating high spatial resolution F_{760} maps. The primary distinction between the two workflows lies in the timing of F_{760} calculation relative to image stitching and the software used for the stitching. This study addressed a critical aspect of high-resolution SIF imaging, focusing on the impact of image processing techniques and the effects of interpolation in mosaicking on the quality of F_{760} estimates. The method also considers the unavoidable interpolation step in registering spectral channels. By comparing the two workflows, limitations were identified in standard photogrammetry software Agisoft Metashape for F_{760} images stitching due to their low contrast. The low contrast constrained feature detection and image alignment. This approach enabled the estimate of F_{760} only after generating the mosaic from the preprocessed raw images (DN). This approach raised concerns about F_{760} quality, particularly regarding pixel interpolation in global alignment and blending during mosaic generation. Nevertheless, the analysis of soil pixels indicated less noise in the resulting orthomosaic compared to the MATLAB-based workflow.

The developed MATLAB-based workflow mitigated the concerns regarding interpolation and blending by estimating first F_{760} from co-registered individual images and generating an intermediate mosaic from enhanced contrast F_{760} images to serve as a geometric framework, and then tracking back the pixel values to the original F_{760} images. This approach not only preserved the F_{760} from further interpolation but also mitigated leaf shading effects by eliminating mixed pixels. While this approach is promising, it led to higher noise in soil pixels compared to the Agisoft Metashape orthomosaic. In addition, the MATLAB-based workflow

was developed on a single test dataset and was not optimized for high-throughput data processing. The workflow was initially developed and tested on crops with relatively uniform canopy structures across the field in the wheat and bean experiment. This motivated an evaluation of its robustness and applicability under more diverse crop conditions regarding canopy structure and chlorophyll pigment content. Also, processing a dataset of around 350 image pairs using this workflow requires around two days on a PC with AMD Ryzen Threadripper 3960X CPU with 24-Cores, 256 GB DDR4 SDRAM, base/boost clock speed of: 3.8 GHz/up to 4.5 GHz and Geekbench single-core CPU score of 1704. This limitation has prompted another ongoing project to translate the MATLAB codes into Python. This transition leverages Python's robust multiprocessing capabilities and parallelization that allow for the utilization of multiple or all available CPU cores to reduce the processing time.

Both workflows developed in this study demonstrated statistically significant linear regressions with F_{760} measurements from reference observations with independent measurements (FloX and HyPlant). However, to fully evaluate the performance of the SIFcam processing and improve the reliability and robustness of F_{760} estimates, future research should focus on conducting a comprehensive uncertainty assessment that focuses on the contribution of the processing steps to the final uncertainty budget for SIFcam processing, building upon the assessment introduced by [256]. In this context, all uncertainty sources, including instrumental effects, radiometric/spectral calibration, data processing assumptions, F_{760} retrieval algorithms, environmental factors, and uncertainty from drone operation, such as positioning error, should be identified and their uncertainties quantified. Error propagation techniques can then be applied to combine these individual uncertainties and determine their cumulative effect on the F_{760} estimates. This analysis will provide the measurement quality of SIFcam in terms of accuracy (systematic errors) and precision (random errors), ultimately enabling more informed conclusions regarding the most reliable processing chain.

The SIFcam demonstrated adequate stability in data collection at the field scale, with less than one pixel variation between spectral channels in both horizontal and vertical directions. The SIFcam has also shown its capability to effectively disentangle the fluorescence signal from canopy reflectance with a moderate level of accuracy. This performance can be attributed to the SIFcam's exceptionally high spatial resolution for F_{760} measurements that is currently unparalleled in the field. To date, only two other studies, both employed the ground-based, much larger HyScreen system, have reported SIF data at comparable spatial resolutions [131, 230]. However, the very high spatial resolution, while valuable, poses challenges in F_{760} interpretation due to revealing variation in canopy structure, which also enhances the influence of directional effects of SIF emission at

TOC (scattering, reabsorption, and sun-sensor geometries) resulting in complex anisotropic reflectance patterns. While the directionality effect on reflectance from UAV-based was addressed [257], such effects on the TOC SIF from high spatial resolution images have not been well studied and should be investigated in further studies.

Chapter 4 explored the synergistic potential of SIFcam F_{760} alongside UAV-based multispectral VIs to characterize and delineate differences among diverse new and old winter wheat cultivars. The genotypically determined morphological traits of the old and new winter wheat cultivars, specifically the plant height and leaf angle orientation, had formed a heterogeneous canopy structure within the experiment field. This diversity aimed to assess the robustness of the developed workflow under more complex field conditions. The study encountered methodological constraints stemming from insufficient side overlap exacerbated by the removal of so many blurry images, hindering the generation of a comprehensive final mosaic. This limitation subsequently hindered the evaluation of the robustness of the developed methodology. To mitigate these issues in future studies, we recommend 1) maintaining a minimum 75% side overlap between flight lines to ensure spatial coverage and 2) utilizing 4x4 spatial binning to reduce integration times by a factor of four with an adequate flight speed of approximately 2.5 m/s, thereby minimizing motion-induced blur.

Under the aforementioned limitations, F_{760} was successfully estimated for each variety from individual co-registered pair images. This approach demonstrated a notable potential of SIFcam in capturing the variability of F_{760} between wheat cultivars with structural and pigment differences.

New wheat cultivars generally revealed higher F_{760}, consistent with their higher chlorophyll content, yet old cultivar Banco indicated that canopy architecture could significantly modulate TOC F_{760}, with F_{760} values comparable to or even exceeding those of certain new cultivars. VIs outperformed F_{760} in detecting unique and consistent patterns between the new and old cultivars. A substantial variation in VIs' effectiveness was observed, mostly related to their sensitivities to chlorophyll content and LAI. TCARI/OSAVI proved to be the most effective index in distinguishing breeding-induced changes compared to other indices (Cohen's d >= 0.5).

The study demonstrated the complex interplay between the TOC F_{760}, canopy structure, chlorophyll content, and photosynthetic efficiency. While higher chlorophyll content enhances SIF emission at the leaf level, it increases reabsorption and potentially attenuates the TOC SIF signal. Erectophile leaves, common in new cultivars, improve light penetration and potential SIF emission, yet this vertical leaf arrangement prolongs the path for SIF photons to escape the canopy, further boosting reabsorption and likely reducing TOC SIF. Conversely, planophile leaf

orientation, observed in older cultivars, may result in lower overall SIF production due to reduced light penetration, yet their horizontal leaf arrangement promotes more photons to escape the canopy, thus higher TOC SIF despite lower leaf SIF production.

To further elucidate these complex relationships, additional measurements, such as leaf-level SIF measurements, active fluorescence measurements for quantifying photosynthetic activity, harvest data, and diurnal SIF measurements and flights across the growing season, could enhance the study.

The study findings highlight the importance of considering both physical and physiological factors when interpreting TOC F_{760} measurements. Therefore, future research should focus on developing methods to decouple the effects of leaf and canopy structure from physiological differences in the SIFcam TOC F_{760} emissions by calculating F_{760} efficiency or the F_{escape}, which describes the scattering of SIF in the viewing direction. This normalization could significantly enhance the interpretation of SIFcam data and minimize the directional effects, although it has not been attempted in the current study. A potential method for F_{760} normalization and downscaling can be derived from the basic equation of SIF downscaling presented by [156]

$$\epsilon_{F_{760}} = \frac{\pi F_{760}}{PAR \times FCVI} \tag{5.1}$$

$\epsilon_{F_{760}}$ is F_{760} efficiency in nm^{-1}. In this context, PAR could be obtained from ground-based measurements, such as weather stations or FloX systems. The VI could be calculated from multispectral data, with the FCVI being a potential candidate:

$$FCVI = R_{NIR} - R_{\overline{VIS}} \tag{5.2}$$

This requires acquiring the multispectral data simultaneously with SIF measurements to ensure the same shadow distribution in the canopy. Ideally, as [156] reported, these data would be collected by the same sensor to minimize discrepancies.

In addition, a sensitivity analysis using an RTM could enhance the development and validation of such a downscaling approach as well as enhance the SIFcam F_{760} data interpretation. RTMs offer a valuable way to investigate the effect of complex sources of variability related to leaf and canopy structure (e.g., leaf angle distribution, LAI), PAR absorption, and SIF scattering and re-absorption on the TOC SIF.

Additionally, future research should focus on disentangling shaded and sunlit pixels from the total canopy reflectance spectrum to promote further the application of the SIFcam-based F_{760} for plant physiological monitoring. One promising approach presented by [258] involves applying linear spectral unmixing methods

to the high-resolution SIFcam image to decompose the measured spectral reflectance into the soil, sunlit vegetation, and shaded vegetation components and retrieve the sunlit FVC (FVC_{sunlit}). In this context, several flights of the SIFcam should be conducted over selected targets representing pure samples of soil, sunlit vegetation, and shaded vegetation within a study area synchronized with ground-based spectral measurements for validation. The estimation of FVC_{sunlit} enables an estimate of the amount of light absorbed by photosynthetic plant pigments (green APAR), leading to a more precise estimation of $\epsilon_{F_{760}}$.

Chapter 6

Conclusion

This study has made a substantial contribution to the UAV-based remote sensing applications in crop monitoring on the field scale through three studies. The first study made advancements in multispectral UAV-based data processing with a low-cost, commercial sensor. The developed open-source Python-based workflow for the DJI P4M system addressed a critical gap in standardized processing tools for non-radiometrically calibrated systems, potentially benefiting researchers facing similar challenges. The study also uncovered the limitations of small-scale DJI systems in scientific vegetation analysis, particularly the constraints posed by the limited number of indices estimable from five broad spectral bands and the frequent saturation of some VIs-like NDVI in dense vegetation. Furthermore, the research contributed to the understanding of the impact of biochar on crop performance in the context of climate-smart agriculture. Biochar is more likely to benefit crop production in degraded, nutrient-poor soils rather than in fertile conditions.

The second study contributed to the development of robust processing protocols for the novel SIFcam prototype for imaging of F_{760} and enabled the generation of very high-spatial resolution F_{760} maps that are unparalleled on the field scale. The research tackled two distinct workflows: refining a previously developed methodology for generating orthomosaics and introducing an innovative MATLAB-based approach. The study revealed the trade-offs between high geometry mosaics obtained from traditional photogrammetric techniques and F_{760} radiometric quality. The research provided valuable insights into the methodological considerations essential for alternating the weak SIF signal in post-processing as little as possible while leveraging high spatial-resolution imagery with geometric integrity. SIFcam has demonstrated the potential to disentangle the fluorescence signal from canopy reflectance with moderate accuracy and adequate stability under field conditions. The study underscores SIFcam as a promising tool for agricultural applications and paves the way for detailed plant physiolog-

ical studies, bridging the scale gap between proximal and satellite measurements and potentially supporting calibration and validation activities for the upcoming FLEX satellite mission.

The third study marked a noteworthy leap in the application of the SIFcam system in field conditions, showcasing the potential of integrating SIFcam F_{760} and UAV-based multispectral VIs in characterizing diverse winter wheat cultivars. The challenges in generating the F_{760} map for the winter wheat field due to the insufficient overlap between flight lines stemming from data acquisition issues, rather than field heterogeneity, restricted the evaluation of the robustness of the developed methodology. Yet, the study yielded valuable insights. The research demonstrated the complex interplay between the TOC F_{760}, canopy structure, chlorophyll content, and photosynthetic efficiency. The comprehensive analysis of VIs provided valuable insights into the winter wheat properties most affected by breeding efforts. The ability of the SIFcam to detect fine-scale heterogeneity in F_{760} emissions proved to be a valuable tool for field plant phenotyping and potentially guiding breeding programs. F_{760} is affected by the directionality due to the canopy structure, sun sensor geometry, and scattering and reabsorption within the canopy. Downscaling of F_{760} will improve the interpretation of the F_{760} and boost its application in crop physiology monitoring.

Bibliography

[1] A. Mălinaş , R. Vidican ,I. Rotar, C. Mălinaş, C. M. Moldovan, and M. Proorocu, "Current Status and Future Prospective for Nitrogen Use Efficiency in Wheat (Triticum aestivum L.)," *Plants*, vol. 11, no. 2, 2022, DOI: 10.3390/plants11020217

[2] FAO, "The future of food and agriculture – Trends and challenges," Rome, 2017.

[3] T. Gomiero, D. Pimentel, and M. G. Paoletti, "Environmental Impact of Different Agricultural Management Practices: Conventional vs. Organic Agriculture," *Critical Reviews in Plant Sciences*, vol. 30, no. 1-2, pp. 95–124, 2011, DOI: 10.1080/07352689.2011.554355

[4] J. I. L. Morison, and R. B. Matthews (eds.), "Agriculture and forestry climate change impacts summary report, *Living With Environmental Change*,2016

[5] M. Alotaibi, "Climate change, its impact on crop production, challenges, and possible solutions," *Notulae Botanicae Horti Agrobotanici Cluj-Napoca*, vol. 51, no.1, 2023, pp. 13020, 2023, DOI: 10.15835/nbha51113020

[6] M. Weiss, F. Jacob, and G. Duveiller, "Remote sensing for agricultural applications: A meta-review," *Remote Sensing of Environment*, vol. 236, pp. 111402, 2020, DOI: 10.1016/j .rse.2019.111402

[7] R. Vidican , A. Mălinaș,O. Ranta, C. Moldovan ,O. Marian, A. Ghețe, C. R. Ghișe ,F. Popovici, and G. M. Cătunescu, "Using Remote Sensing Vegetation Indices for the Discrimination and Monitoring of Agricultural Crops: A Critical Review," *Agronomy*, vol. 13, no. 12, pp. 3040, 2023, DOI: 10.3390/agronomy13123040

[8] P. Karmakar, Sh. W. Teng, M. Murshed, Sh. Pang, Y. Li, and H. Lin, "Crop monitoring by multimodal remote sensing: A review," *Remote Sensing Applications: Society and Environment*, vol. 33, pp. 101093, 2024, DOI: 10.1016/j .rsase.2023.101093

[9] United Nations Framework Convention on Climate Change, "Technology Executive Committee: Technologies for Adaptation in the Agriculture Sector," TEC Brief 4, 2014.

[10] A. Gassner, R. Coe, and F. Sinclair, "Improving food security through increasing the precision of agricultural development," in *Precision Agriculture for Sustainability and Environmental Protection*, 1st ed., Routledge, 2013

[11] E. Omia, H. Bae, E. Park, M. S. Kim, I. Baek, I. Kabenge, and B-K Cho, "Remote Sensing in Field Crop Monitoring: A Comprehensive Review of Sensor Systems, Data Analyses and Recent Advances," *Remote Sensing*, vol. 15, no. 2, pp. 354, 2023, DOI: 10.3390/rs15020354

[12] M. Padhiary, D. Saha, R. Kumar, L. N. Sethi, and A. Kumar, "Enhancing precision agriculture: A comprehensive review of machine learning and AI vision applications in all-terrain vehicle for farm automation," *Smart Agricultural Technology*, vol. 8, pp. 100483, 2024, DOI: 10.1016/j .atech.2024.100483.

[13] U. Shafi, R. Mumtaz, J. García-Nieto, S. Ali Hassan, S. A. R. Zaidi, and N. Iqbal, "Precision Agriculture Techniques and Practices: From Considerations to Applications," *Sensors*, vol. 19, no. 17, pp. 3796, 2019, DOI: 10.3390/s19173796

[14] R. P. Sishodia, R. L. Ray, and S. K. Singh, "Applications of Remote Sensing in Precision Agriculture: A Review," *Remote Sensing*, vol. 12, no. 19, pp. 3136, 2020, DOI: 10.3390/rs12193136

[15] R. F. Kokaly, G. P. Asner, S. V. Ollinger, M. E. Martin, and C. A. Wessman, "Characterizing canopy biochemistry from imaging spectroscopy and its application to ecosystem studies," *Remote Sensing of Environment*, vol. 113, Supplement 1, pp. S78-S91, 2009, DOI: 10.1016/j

[16] D. J. Mulla, "Twenty five years of remote sensing in precision agriculture: Key advances and remaining knowledge gaps," *Biosystems Engineering*, vol. 114, no. 4, pp. 358-371, 2013, DOI: 10.1016/j .biosystemseng.2012.08.009

[17] S. V. Ollinger, "Sources of variability in canopy reflectance and the convergent properties of plants," *New Phytologist* , vol. 189, no. 2, pp. 375-394, 2010, DOI: 10.1111/j.1469-8137.2010.03536.x

[18] J. Xue, and B. Su, "Significant Remote Sensing Vegetation Indices: A Review of Developments and Applications," *Journal of Sensors*, vol. 2017, no. 1, pp. 1353691, 2017, DOI: 10.1155/2017/1353691

[19] B. Wu, M. Zhang, H. Zeng, F. Tian, A. B. Potgieter, X. Qin, N. Yan, Sh. Chang, Y. Zhao, Q. Dong, V. Boken, D. Plotnikov, H. Guo, F. Wu, H. Zhao, b. Deronde, L. Tits, and E. Loupian, "Challenges and opportunities in remote sensing-based crop monitoring: a review," *National Science Review*, vol. 10, no. 4, 2023, DOI: 10.1093/nsr/nwac290.biosystemseng.2012.08.009

[20] A. Bégué, D. Arvor, B. Bellon, J. Betbeder, D. De Abelleyra, R. P. D. Ferraz, V. Lebourgeois, C. Lelong, M. Simões, and S. R. Verón, "Remote Sensing and Cropping Practices: A Review," *Remote Sensing*, vol. 10, no. 1, pp. 99, 2018, DOI: 10.3390/rs10010099

[21] C. Huang, Q. Yang, Y. Guo, Y. Zhang, and L. Guo, "The pattern, change and driven factors of vegetation cover in the Qin Mountains region," *Scientific Reports*, vol. 10, no.1, pp. 20591, 2020, DOI: 10.1038/s41598-020-75845-5

[22] S. Khanal ,K. KCORCID, J. P. Fulton, S. Shearer, and E. Ozkan, "Remote Sensing in Agriculture—Accomplishments, Limitations, and Opportunities," *Remote Sensing*, vol. 12, no. 22, pp. 3783, 2020, DOI: 10.3390/rs12223783 .compag.2019.104943

[23] A. Walter, F. Liebisch, and A. Hund, "Plant phenotyping: from bean weighing to image analysis," *Plant Methods*, vol. 11, pp. 14, 2015, DOI: 10.1186/s13007-015-0056-8

[24] T. S. T. Tanaka, S. Wang, J. R. Jørgensen, M. Gentili, A. Zaragüeta Vidal, A. K. Mortensen, B. S. Acharya, B. D. Beck, and R. Gislum, "Review of Crop Phenotyping in Field Plot Experiments Using UAV-Mounted Sensors and Algorithms," *Drones*, vol. 8, no. 6, pp. 212, 2024, DOI: 10.3390/drones8060212

[25] L. S. Macarringue1, E. L. Bolfe, P. R. M. Pereira, "Developments in land use and land cover classification techniques in remote sensing: A review," *Journal of Geographic Information System*, vol. 14, no. 1, pp. 1-28, 2022, DOI: 10.4236/jgis.2022.141001

[26] X. Jin, Z. Li, H. Feng, Z. Ren, and S. Li, "Deep neural network algorithm for estimating maize biomass based on simulated Sentinel 2A vegetation indices and leaf area index," *The Crop Journal*, vol. 8, no. 1, pp. 87-97, 2020, DOI: 10.1016/j .cj.2019.06.005

[27] A. M. Ali, M. Abouelghar, A. A. Belal, N. Saleh, M. Yones, A. I. Selim, M. E.S. Amin, A. Elwesemy, D. E. Kucher, S. Maginan, and I Savin, "Crop Yield Prediction Using Multi Sensors Remote Sensing (Review Article)," *The Egyptian Journal of Remote Sensing and Space Science*, vol. 25, no. 3, pp. 711-716, 2022, DOI: 10.1016/j .ejrs.2022.04.006

[28] M. H. Sellami, R. Albrizio ,M. Čolović, M. Hamze, V. Cantore, M. Todorovic, L. Piscitelli, and A. M. Stellacci, "Selection of Hyperspectral Vegetation Indices for Monitoring Yield and Physiological Response in Sweet Maize under Different Water and Nitrogen Availability," *Agronomy*, vol. 12, no. 2, pp. 489, 2022, DOI: 10.3390/agronomy12020489

[29] I. Pôças, A. Calera, I. Campos, and M. Cunha, "Remote sensing for estimating and mapping single and basal crop coefficientes: A review on spectral vegetation indices approaches," *Agricultural Water Management*, vol. 233, pp. 106081, 2020, DOI: 10.1016/j .agwat.2020.106081.

[30] L. Homolová, Z. Malenovský, J. G. P. W. Clevers, G. García-Santos, and M. E. Schaepman, "Review of optical-based remote sensing for plant trait mapping," *Ecological Complexity*, vol. 15, pp. 1-16, 2013, DOI: 10.1016/j .ecocom.2013.06.003

[31] G. H. Mohammed, R. Colombo, E. M. Middleton, U. Rascher, C. van der Tol, L. Nedbal, Y. Goulas, O. Pérez-Priego, A. Damm, M. Meroni, J. Joiner, S. Cogliati, W. Verhoef, Z. Malenovský, J.-P. Gastellu-Etchegorry, J. R. Miller, L. Guanter, J. Moreno, I. Moya, J. A. Berry, C. Frankenberg, and P. J. Zarco-Tejada, "Remote Sensing of Solar-Induced Chlorophyll Fluorescence (SIF) in Vegetation: 50 Years of Progress," *Remote Sensing of Environment*, vol. 231, pp. 111177, 2019, DOI: 10.1016/j .rse.2019.04.030

[32] D. C. Tsouros, S. Bibi, and P. G. Sarigiannidis, "A Review on UAV-Based Applications for Precision Agriculture," *Information*, vol. 10, no. 11, pp. 349, 2019, DOI: 10.3390/info10110349

[33] S. C Chapman, T. Merz, A. Chan, P. Jackway, S. Hrabar, F. M. Dreccer, E. Holland, B. Zheng, T. J. Ling, and J. Jimenez-Berni, "Pheno-Copter: A Low-Altitude, Autonomous Remote-Sensing Robotic Helicopter for High-Throughput Field-Based Phenotyping," *Agronomy*, vol. 4, no. 2, pp. 279-301, 2014, DOI: 10.3390/agronomy4020279

[34] A. Ač, Z. Malenovský, J. Hanuš, I. Tomášková, O. Urban, and M. V. Marek, "Near-distance imaging spectroscopy investigating chlorophyll fluorescence and photosynthetic activity of grassland in the daily course," *Functional Plant Biology*, vol. 36, no. 11, pp. 1006-1015, 2009, DOI: 10.1071/FP09154

[35] D. M. Gates, ´´Physical and physiological properties of plants," pp. 224-52, 1970

[36] D. M. Gates, H. J. Keegan, J. C. Schleter, and V. R. Weidner, "Spectral Properties of Plants," *Applied Optics*, vol. 4, no. 1, pp. 11-20, 1965, DOI: 10.1364/AO.4.000011

[37] A. Bannari, D. Morin, and F. Bonn, "A Review of Vegetation Indices, " *Remote Sensing Reviews*, vol. 13, no. 1-2, pp. 95-120, 1995

[38] A. R. Heute, "Remote Sensing for Environmental Monitoring," *Environmental Monitoring and Characterization*, 2004, DOI: 10.1016/B978-012064477-3/50013-8

[39] N. Katsoulas, A. Elvanidi, K. P. Ferentinos, M. Kacira, Th. Bartzanas, and C. Kittas, "Crop reflectance monitoring as a tool for water stress detection in greenhouses: A review," *Biosystems Engineering*, vol. 151, pp.374-398, 2016, DOI: 10.1016/j .biosystemseng.2016.10.003

[40] Y. Zeng, D. Hao, A. Huete, B. Dechant, J. Berry, J. M. Chen, J. Joiner, Ch. Frankenberg, B. Bond-Lamberty, Y. Ryu, J. Xiao, Gh. R. Asrar, and M. Chen, " Optical vegetation indices for monitoring terrestrial ecosystems globally,"*Nature Reviews Earth and Environment*, vol. 3, pp. 477–493, 2022, DOI: 10.1038/s43017-022-00298-5

[41] W.A. Dorigo, R. Zurita-Milla, A.J.W. de Wit, J. Brazile, R. Singh, M.E. Schaepman, "A review on reflective remote sensing and data assimilation techniques for enhanced agroecosystem modeling," *International Journal of Applied Earth Observation and Geoinformation*, vol. 9, no. 2, pp. 165-193, 2007, DOI: 10.1016/j.jag.2006.05.003 .

[42] S. M. Kochubey, and T. A. Kazantsev, "Derivative vegetation indices as a new approach in remote sensing of vegetation, "*Frontiers of Earth Science*, vol. 6, no. 2, pp. 188–195,2012, DOI: 10.1007/s11707-012-0325-z

[43] S. Gao, R. Zhong, K. Yan, X. Ma, X. Chen, J. Pu, S. Gao, J. Qi, G. Yin, R. B. Myneni, "Evaluating the saturation effect of vegetation indices in forests using 3D radiative transfer simulations and satellite observations," *Remote Sensing of Environment*, vol. 295, pp. 113665, 2023, DOI: 10.1016/j .rse.2023.113665.

[44] R. D. Jackson, and A. R. Huete, "Interpreting vegetation indices,"*Preventive Veterinary Medicine*, vol. 11, no. 3–4, pp. 185-200, 1991, DOI: 10.1016/S0167-5877(05)80004-2

[45] E. P. Glenn, A. R. Huete, P. L. Nagler, and S. G. Nelson, "Relationship Between Remotely-sensed Vegetation Indices, Canopy Attributes and Plant Physiological Processes: What Vegetation Indices Can and Cannot Tell Us

About the Landscape," *Sensors*, vol. 8, no. 4, pp. 2136-2160, 2008, DOI: 10.3390/s8042136

[46] D. Radočaj, A. Šiljeg, R. Marinović, and M. Jurišić, "State of Major Vegetation Indices in Precision Agriculture Studies Indexed in Web of Science: A Review," *Agriculture*, vol. 13, no. 3, pp. 707, 2023, DOI: 10.3390/agriculture13030707

[47] C. Atzberger, K. Richter, F. Vuolo, R. Darvishzadeh, and M. Schlerf, "Why confining to vegetation indices? Exploiting the potential of improved spectral observations using radiative transfer models," in *Remote Sensing for Agriculture, Ecosystems, and Hydrology XIII*, vol. 8174, pp. 81740Q, International Society for Optics and Photonics, 2011, DOI: 10.1117/12.898479

[48] J. W. Rouse, R. H. Haas, J. A. Schell, and D. W. Deering, "Monitoring vegetation systems in the great plains with ERTS," in *Third ERTS-1 Symposium NASA*, pp. 309-317, 1974

[49] C. J. Tucker, "Red and photographic infrared linear combinations for monitoring vegetation,"*Remote Sensing of Environment*, vol. 8, no. 2, pp. 127-150, 1979, DOI: 10.1016/0034-4257(79)90013-0

[50] F. Maselli, M. Chiesi, L. Angeli, L. Fibbi, B. Rapi, M. Romani, F. Sabatini, P. Battista, An improved NDVI-based method to predict actual evapotranspiration of irrigated grasses and crops, Agricultural Water Management, Volume 233, 2020, 106077, DOI: 10.1016/j .agwat.2020.106077.

[51] A. Huete, K. Didan, T . Miura, E.P. Rodriguez, X. Gao, L.G. Ferreira, "Overview of the radiometric and biophysical performance of the MODIS vegetation indices," *Remote Sensing of Environment*, vol. 83, no. 1-2, pp. 195-213, 2002, DOI: 10.1016/S0034-4257(02)00096-2

[52] A. Huete, "A soil-adjusted vegetation index (SAVI)," *Remote sensing of environment*, vol. 25, no. 3, pp. 295-309, 1988, DOI: 10.1016/0034-4257(88)90106-X

[53] P. P. Rhyma, K. Norizah, O. Hamdan, I. Faridah-Hanum, and A. W. Zulfa, "Integration of normalised different vegetation index and Soil-Adjusted Vegetation Index for mangrove vegetation delineation," *Remote Sensing Applications: Society and Environment*, vol. 17, pp. 100280, 2020, DOI: 10.1016/j .rsase.2019.100280

[54] A. Huete, Ch. Justice, and W. Van Leeuwen, "MODIS vegetation index (MOD13) algorithm theoretical basis document, 1999

[55] M. Dallimer, Z. Tang, P. R. Bibby, P. Brindley, K. J. Gaston, and Z. G. Davies, "Temporal changes in greenspace in a highly urbanized region," *Biology letters*, vol. 7, no. 5, pp. 763–766, 2011, DOI: 10.1098/rsbl.2011.0025

[56] I. Filella and J. Penuelas, "The red edge position and shape as indicators of plant chlorophyll content, biomass and hydric status," *International Journal of Remote Sensing*, vol. 15, no. 7, pp. 1459-1470, 1994, DOI: 10.1080/01431169408954177

[57] J. Delegido, J. Verrelst, C.M. Meza, J.P. Rivera, L. Alonso, J. Moreno, "A red-edge spectral index for remote sensing estimation of green LAI over agroecosystems," *European Journal of Agronomy*, vol. 46, pp. 42-52, 2013, DOI: 10.1016/j .eja.2012.12.001

[58] J. Clevers, S. M. De Jong, G. F. Epema, F. D. Van Der Meer, W. H. Bakker, A. K Skidmore, and K. H. Scholte, "Derivation of the red edge index using the MERIS standard band setting," *International Journal of Remote Sensing*, vol. 23, no. 16, pp. 3169-3184, 2002, DOI: 10.1080/01431160110104647

[59] E. Zillmann, M. Schönert, H. Lilienthal, B. Siegmann, T. Jarmer, P. Rosso, and T. Weichelt, "Crop Ground Cover Fraction and Canopy Chlorophyll Content Mapping using RapidEye imagery," *ISPRS - International Archives of the Photogrammetry, Remote Sensing and Spatial Information Sciences*, vol. XL-7/W3, pp. 149-155, 2015, DOI: 10.5194/isprsarchives-XL-7-W3-149-2015

[60] D. Al-Shammari, B. M. Whelan, C. Wang, R. G. V. Bramley, and T. F. A. Bishop, "Assessment of red-edge based vegetation indices for crop yield prediction at the field scale across large regions in Australia," *European Journal of Agronomy*, vol. 164, pp. 127479, 2025, DOI: 10.1016/j .eja.2024.127479

[61] O. Mutanga, and A. K. Skidmore, "Narrow band vegetation indices overcome the saturation problem in biomass estimation," *International Journal of Remote Sensing*, vol. 25, no. 19, pp. 3999-4014, 2004, DOI: 10.1080/01431160310001654923

[62] A. A. Tesfaye and B. Gessesse Awoke, "Evaluation of the saturation property of vegetation indices derived from sentinel-2 in mixed crop-forest ecosystem," *Spatial Information Research*, vol. 29, pp. 109-121, 2021, DOI: 10.1007/s41324-020-00339-5

[63] D. A. Roberts, K. Roth, R. L. Perroy, "Hyperspectral Vegetation Indices, " in *Hyperspectral Remote Sensing of Vegetation*, pp. 309-327, Oct. 2011, DOI: 10.1201/b11222-20

[64] D. Haboudane, J. R. Miller, E. Pattey, P. J. Zarco-Tejada, and I. B. Strachan, "Hyperspectral vegetation indices and novel algorithms for predicting green LAI of crop canopies: Modeling and validation in the context of precision agriculture," *Remote Sensing of Environment*, vol. 90, no. 3, pp. 337-352, 2004, DOI: 10.1016/j .rse.2003.12.013

[65] M. S. Kim, C. S. T. Daughtry, E. W. Chappelle, J. E. McMurtrey, and C. L. Walthall, "The use of high spectral resolution bands for estimating absorbed photosynthetically active radiation (A par)," in *CNES, Proceedings of 6th International Symposium on Physical Measurements and Signatures in Remote Sensing*, no. GSFC-E-DAA-TN72921, 1994

[66] T. Fourty, F. Baret, S. Jacquemoud, G. Schmuck, and J. Verdebout, "Leaf optical properties with explicit description of its biochemical composition: Direct and inverse problems," *Remote Sensing of Environment*, vol. 56, no. 2, pp. 104-117, 1996, DOI: 10.1016/0034-4257(95)00234-0

[67] J. A. Gamon, J. Peñuelas, and C.B. Field, "A narrow-waveband spectral index that tracks diurnal changes in photosynthetic efficiency," *Remote Sensing of Environment*, vol. 41, no. 1, pp. 35-44, 1992, DOI: 10.1016/0034-4257(92)90059-S

[68] I. Filella, A. Porcar-Castell, S. Munné-Bosch, J. Bäck, M. F. Garbulsky, and J. Peñuelas, "PRI assessment of long-term changes in carotenoids/chlorophyll ratio and short-term changes in de-epoxidation state of the xanthophyll cycle," *International Journal of Remote Sensing*, vol. 30, no. 17, pp. 4443–4455, 2009, DOI: 10.1080/01431160802575661

[69] Y. Nakamura, K. Tsujimoto, T. Ogawa, H.M. Noda, and K. Hikosaka, "Correction of photochemical reflectance index (PRI) by optical indices to predict non-photochemical quenching (NPQ) across various species," *Remote Sensing of Environment*, vol. 305, pp. 114062, 2024, DOI: 10.1016/j .rse.2024.114062

[70] R. E. Baker, J-M Peña, J. Jayamohan, and A. Jérusalem, "Mechanistic models versus machine learning, a fight worth fighting for the biological community?," *Biology letters*, vol. 14, no. 5, pp. 20170660, 2018, DOI: 10.1098/rsbl.2017.0660

[71] J. Verrelst, G. Camps-Valls, J. Muñoz-Marí, J. P. Rivera, F. Veroustraete, J. G.P.W. Clevers, and J. Moreno, "Optical remote sensing and the retrieval of terrestrial vegetation bio-geophysical properties – A review," *ISPRS Journal of Photogrammetry and Remote Sensing*, vol. 108, pp. 273-290, 2015, DOI: 10.1016/j .isprsjprs.2015.05.005

[72] S. Jacquemoud, J. Verdebout, G. Schmuck, G. Andreoli, and B. Hosgood, "Investigation of leaf biochemistry by statistics," *Remote Sensing of Environment*, vol. 54, no. 3, pp. 180-188, 1995, DOI: 10.1016/0034-4257(95)00170-0

[73] Z. Huang, B. J. Turner, S. J. Dury, I. R. Wallis, and W. J. Foley, "Estimating foliage nitrogen concentration from HYMAP data using continuum removal analysis," *Remote Sensing of Environment*, vol. 93, no. 1-2, pp. 18-29, 2004, DOI: 10.1016/j .rse.2004.06.008

[74] C. Atzberger, "Object-based retrieval of biophysical canopy variables using artificial neural nets and radiative transfer models," *Remote Sensing of Environment*, vol. 93, no. 1-2, pp. 53-67, 2004, DOI: 10.1016/j .rse.2004.06.016

[75] B. Pinty, N. Gobron, J.-L. Widlowski, S. A. W. Gerstl, M. M. Verstraete, M. Antunes, C. Bacour, F. Gascon, J.-P. Gastellu, N. Goel, S. Jacquemoud, P. North, W. Qin, and R. Thompson, "Radiation transfer model intercomparison (RAMI) exercise," *Journal of Geophysical Research: Atmospheres*, vol. 106, no. D11, pp. 11937-11956, 2001, DOI: 10.1029/2000JD900493

[76] B. Kötz, M. Schaepman, F. Morsdorf, P. Bowyer, K. Itten, and B. Allgöwer, "Radiative transfer modeling within a heterogeneous canopy for estimation of forest fire fuel properties," *Remote Sensing of Environment*, vol. 92, no. 3, pp. 332-344, 2004, DOI: 10.1016/j.rse.2004.05.015

[77] J. Qi, D. Xie, D. Guo, and G. Yan, "A Large-Scale Emulation System for Realistic Three-Dimensional (3-D) Forest Simulation," *IEEE Journal of Selected Topics in Applied Earth Observations and Remote Sensing*, vol. 10, no. 11, pp. 4834-4843, 2017, DOI: 10.1109/JSTARS.2017.2714423

[78] J. R. Melendo-Vega, M. P. Martín, J. Pacheco-Labrador, R. González-Cascón, G. Moreno, F. Pérez, M. Migliavacca, M. García, P. North, and D. Riaño, "Improving the Performance of 3-D Radiative Transfer Model FLIGHT to Simulate Optical Properties of a Tree-Grass Ecosystem," *Remote Sensing*, vol. 10, no. 12, pp. 2061, 2018, DOI: 10.3390/rs10122061

[79] R. A. F. Ishaq, G. Zhou, C. Tian, Y. Tan, G. Jing, H. Jiang, and O. Rehman, "A Systematic Review of Radiative Transfer Models for Crop Yield Prediction and Crop Traits Retrieval," *Remote Sensing*, vol. 16, no. 1, pp. 121, 2024, DOI: 10.3390/rs16010121

[80] P. S. Thenkabail, R. B. Smith, and E. De Pauw, "Hyperspectral Vegetation Indices and Their Relationships with Agricultural Crop Characteristics," *Remote Sensing of Environment*, vol. 71, no. 2, pp. 158-182, 2000, DOI: 10.1016/S0034-4257(99)00067-X

[81] J. S. Pearlman, P. S. Barry, C. C. Segal, J. Shepanski, D. Beiso and S. L. Carman, "Hyperion, a space-based imaging spectrometer," *IEEE Transactions on Geoscience and Remote Sensing*, vol. 41, no. 6, pp. 1160-1173, 2003, DOI: 10.1109/TGRS.2003.815018

[82] M. J. Barnsley, J. J. Settle, M. A. Cutter, D. R. Lobb, and F. Teston, "The PROBA/CHRIS mission: a low-cost smallsat for hyperspectral multiangle observations of the Earth surface and atmosphere," *IEEE Transactions on Geoscience and Remote Sensing*, vol. 42, no. 7, pp. 1512-1520, 2004, DOI: 10.1109/TGRS.2004.827260

[83] Y. Guo, K. Mokany, C. Ong, P. Moghadam, S. Ferrier, and S. R. Levick, "Plant species richness prediction from DESIS hyperspectral data: A comparison study on feature extraction procedures and regression models," *ISPRS Journal of Photogrammetry and Remote Sensing*, vol. 196, pp. 120-133, 2023, DOI: 10.1016/j .isprsjprs.2022.12.028

[84] S. Cogliati, F. Sarti, L. Chiarantini, M. Cosi, R. Lorusso, E. Lopinto, F. Miglietta, L. Genesio, L. Guanter, A. Damm, S. Pérez-López, D. Scheffler, G. Tagliabue, C. Panigada, U. Rascher, T.P.F. Dowling, C. Giardino, and R. Colombo, "The PRISMA imaging spectroscopy mission: overview and first performance analysis," *Remote Sensing of Environment*, vol. 262, pp. 112499, 2021, DOI: 10.1016/j

[85] T. Storch, H.-P. Honold, S. Chabrillat, M. Habermeyer, P. Tucker, M. Brell, A. Ohndorf, K. Wirth, M. Betz, M. Kuchler, H. Mühle, E. Carmona, S. Baur, M. Mücke, S. Löw, D. Schulze, S. Zimmermann, C. Lenzen, S. Wiesner, S. Aida, R. Kahle, P. Willburger, S. Hartung, D. Dietrich, N. Plesia, M. Tegler, K. Schork, K. Alonso, D. Marshall, B. Gerasch, P. Schwind, M. Pato, M. Schneider, R. de los Reyes, M. Langheinrich, J. Wenzel, M. Bachmann, S. Holzwarth, N. Pinnel, L. Guanter, K. Segl, D. Scheffler, S. Foerster, N. Bohn, A. Bracher, M. A. Soppa, F. Gascon, R. Green, R. Kokaly, J. Moreno, C. Ong, M. Sornig, R. Wernitz, K. Bagschik, D. Reintsema, L. La Porta, A. Schickling, S. Fischer, "The EnMAP imaging spectroscopy mission towards operations," *Remote Sensing of Environment*, vol. 294, pp. 113632, 2023, DOI: 10.1016/j .rse.2023.113632

[86] M. Rast, J. Nieke, J. Adams, C. Isola, and F. Gascon, "Copernicus Hyperspectral Imaging Mission for the Environment (Chime)," in *2021 IEEE International Geoscience and Remote Sensing Symposium (IGARSS)*, Brussels, Belgium, 2021, pp. 108-111, DOI: 10.1109/IGARSS47720.2021.9553319

[87] M. Rast and T. H. Painter, "Earth Observation Imaging Spectroscopy for Terrestrial Systems: An Overview of Its History, Techniques, and Applications of Its Missions," *Surveys in Geophysics*, vol. 40, no. 3, pp. 303-331, 2019, DOI: 10.1007/s10712-019-09517-z

[88] B.G. Ram, P. Oduor, C. Igathinathane, K. Howatt, and X. Sun, "A systematic review of hyperspectral imaging in precision agriculture: Analysis of its current state and future prospects," *Computers and Electronics in Agriculture*, vol. 222, pp. 109037, 2024, DOI: 10.1016/j .compag.2024.109037

[89] B. Lu, P.D. Dao, J. Liu, Y. He, and J. Shang, "Recent Advances of Hyperspectral Imaging Technology and Applications in Agriculture," *Remote Sensing*, vol. 12, no. 16, pp. 2659, 2020, DOI: 10.3390/rs12162659

[90] F. López-Granados, "Weed detection for site-specific weed management: mapping and real-time approaches," *Weed Research*, vol. 51, no. 1, pp. 1-11, 2011, DOI: 10.1111/j.1365-3180.2010.00829.x

[91] L. Alparone, A. Arienzo, and A. Garzelli, "Spatial Resolution Enhancement of Vegetation Indexes via Fusion of Hyperspectral and Multispectral Satellite Data," *Remote Sensing*, vol. 16, no. 5, 875, 2024, DOI: 10.3390/rs16050875

[92] L. Alparone, A. Arienzo, and A. Garzelli, "Spatial Resolution Enhancement of Satellite Hyperspectral Data via Nested Hypersharpening With Sentinel-2 Multispectral Data," *IEEE Journal of Selected Topics in Applied Earth Observations and Remote Sensing*, vol. 17, pp. 10956-10966, 2024, DOI: 10.1109/JSTARS.2024.3406762

[93] L. Guanter, H. Kaufmann, K. Segl, S. Foerster, C. Rogass, S. Chabrillat, T. Kuester, A. Hollstein, G. Rossner, C. Chlebek, C. Straif, S. Fischer, S. Schrader, T. Storch, U. Heiden, A. Mueller, M. Bachmann, H. Mühle, R. Müller, and M. Habermeyer, "The EnMAP Spaceborne Imaging Spectroscopy Mission for Earth Observation," *Remote Sensing*, vol. 7, no. 7, pp. 8830-8857, 2015, DOI: 10.3390/rs70708830

[94] O. Mutanga, E. Adam, and M. A. Cho, "High density biomass estimation for wetland vegetation using WorldView-2 imagery and random forest regression algorithm," *International Journal of Applied Earth Observation and Geoinformation*, vol. 18, pp. 399-406, 2012, DOI: 10.1016/j.jag.2012.03.012

[95] A. R. Huete, H. Liu; W. J. D. van Leeuwen, "The use of vegetation indices in forested regions: issues of linearity and saturation," in *1997 IEEE International Geoscience and Remote Sensing Symposium Proceedings. Remote*

Sensing - A Scientific Vision for Sustainable Development, Singapore, vol. 4, pp. 1966-1968, 1997, DOI: 10.1109/IGARSS.1997.609169

[96] O. Mutanga, A. Masenyama, and M. Sibanda, "Spectral saturation in the remote sensing of high-density vegetation traits: A systematic review of progress, challenges, and prospects," *ISPRS Journal of Photogrammetry and Remote Sensing*, vol. 198, pp. 297-309, 2023, DOI: 10.1016/j .isprsjprs.2023.03.010

[97] A. A. Gitelson, "Wide Dynamic Range Vegetation Index for Remote Quantification of Biophysical Characteristics of Vegetation," *Journal of Plant Physiology*, vol. 161, no. 2, pp. 165-173, 2004, DOI: 10.1078/0176-1617-01176

[98] D. Vaiopoulos, G. A. Skianis, and K. Nikolakopoulos, "The contribution of probability theory in assessing the efficiency of two frequently used vegetation indices," *International Journal of Remote Sensing* , vol. 25, no. 20, pp. 4219-4236, 2004, DOI: 10.1080/01431160410001680464

[99] L. Guanter, L. Alonso, L. Gómez-Chova, M. Meroni, R. Preusker, J. Fischer, J. Moreno, "Developments for vegetation fluorescence retrieval from spaceborne high-resolution spectrometry in the O2-A and O2-B absorption bands," *Journal of Geophysical Research: Atmospheres*, vol. 115, 2010, DOI: 10.1029/2009JD013716

[100] F. Baret, and G. Guyot, "Potentials and limits of vegetation indices for LAI and APAR assessment," *Remote Sensing of Environment*, vol. 35, no. 2–3, pp. 161-173, 1991, DOI: 10.1016/0034-4257(91)90009-U

[101] S. Bandopadhyay, A. Rastogi, A. Cogliati, U. Rascher, M. Gąbka, and R. Juszczak, "Can Vegetation Indices Serve as Proxies for Potential Sun-Induced Fluorescence (SIF)? A Fuzzy Simulation Approach on Airborne Imaging Spectroscopy Data," *Remote Sensing*, vol. 13, no. 13, pp. 2545, 2021, DOI: 10.3390/rs13132545

[102] M. Meroni, M. Rossini, L. Guanter, L. Alonso, U. Rascher, R. Colombo, and J. Moreno, "Remote Sensing of Solar-Induced Chlorophyll Fluorescence: Review of Methods and Applications," *Remote Sensing of Environment*, vol. 113, no. 10, pp. 2037-2051, 2009, DOI: 10.1016/j .rse.2009.05.003

[103] M. Croci, G. Impollonia, A. Marcone, G. Antonucci, T. Letterio, M. Colauzzi, M. Vignudelli, F. Ventura, S. Anconelli, and S. Amaducci, "RTM Inversion through Predictive Equations for Multi-Crop LAI Retrieval Using Sentinel-2 Images," *Agronomy*, vol. 12, no. 11, pp. 2835, 2022, DOI: 10.3390/agronomy12112835

[104] G. H. Krause, and E. Weis, "Chlorophyll fluorescence as a tool in plant physiology," *Photosynth Research*, vol. 5, pp. 139–157, 1984, DOI: 10.1007/BF00028527

[105] N. Baker, "Chlorophyll Fluorescence: A Probe of Photosynthesis In Vivo," *Annual review of plant biology*, vol. 59, pp. 89-113, 2008, DOI: 10.1146/annurev.arplant.59.032607.092759

[106] K. J. Lees, T. Quaife, R. R.E. Artz, M. Khomik and J. M. Clark, "Potential for using remote sensing to estimate carbon fluxes across northern peatlands – A review," *Science of the Total Environment*, vol. 615, pp. 857-874, 2018, DOI: 10.1016/j .scitotenv.2017.09.103

[107] A. Porcar-Castell, E. Tyystjärvi, J. Atherton, Ch.Van Der Tol, J. Flexas, E. E Pfündel, J. Moreno, Ch. Frankenberg, and J.A Berry, "Linking chlorophyll a fluorescence to photosynthesis for remote sensing applications: Mechanisms and challenges," *Journal of Experimental Botany*, vol. 65, no. 15, pp. 4065-4095, 2014, DOI: 10.1093/jxb/eru191

[108] A. N. Misra, M. Misra, and R. Singh, "Chlorophyll Fluorescence in Plant Biology," in *Biophysics*, A. N. MISRA (eds.), IntechOpen, 2012, DOI: 10.5772/35111

[109] K. Maxwell, and G. N Johnson, "Chlorophyll fluorescence- a practical guide," *Joural of Experimental Botany*, vol. 51, no. 345, pp. 659-668, 2000, DOI: 10.1093/jxb/51.345.659

[110] C. Buschmann, "Variability and application of the chlorophyll fluorescence emission ratio red/far-red of leaves," *Photosynthesis Research*, vol. 92, pp. 261–271, 2007, DOI: 10.1007/s11120-007-9187-8

[111] M. Drusch, J. Moreno, U. Del Bello, R. Franco, Y. Goulas, A. Huth, S. Kraft, E. M. Middleton, F. Miglietta, G. Mohammed, L. Nedbal, U. Rascher, D. Schüttemeyer, and W. Verhoef, "The FLuorescence EXplorer Mission Concept—ESA's Earth Explorer 8," *IEEE Transactions on Geoscience and Remote Sensing*, vol. 55, no. 3, pp.1273-1284, 2017, DOI: 10.1109/TGRS.2016.2621820

[112] H. Krause,and E. Weis , "Chlorophyll fluorescence and photosynthesis–the basics," *Annu Rev Plant Physiol Plant Mol Biol*, vol.42, pp. 313–349, 1991

[113] E. Kress, and P. Jahns, "The Dynamics of Energy Dissipation and Xanthophyll Conversion in Arabidopsis Indicate an Indirect Photoprotective

Role of Zeaxanthin in Slowly Inducible and Relaxing Components of Non-photochemical Quenching of Excitation Energy," *Frontiers of plant science*, vol. 8, 2017, DOI: 10.3389/fpls.2017.02094

[114] J. Chauhan, M.D. Prathibha, P. Singh, P. Choyal, U.N. Mishra, D. Saha, R. Kumar, H. Anuragi, S. Pandey, B. Bose, B. Mehta, P. Dey, K.K. Dwivedi, N.K. Gupta, and R.K. Singhal, "Plant photosynthesis under abiotic stresses: Damages, adaptive, and signaling mechanisms," *Plant Stress*, vol. 10, pp. 100296, 2023, DOI: 10.1016/j.stress.2023.100296

[115] P. K. Entcheva Campbell, E. M. Middleton, L. A. Corp, and M. S. Kim, "Contribution of chlorophyll fluorescence to the apparent vegetation reflectance," *Science of the Total Environment*, vol. 404, no. 2-3, pp. 433-439, 2008, DOI: 10.1016/j . scitotenv.2007.11.004

[116] A. Porcar-Castell , Z. Malenovský , T. Magney , S. Van Wittenberghe , B. Fernández-Marín , F. Maignan , Y. Zhang , K. Maseyk , J. Atherton , L.P. Albert , T.M Robson , Feng Zhao , J.I . Garcia-Plazaola , I. Ensminger, P.A. Rajewicz, S. Grebe, M. Tikkanen, J.R. Kellner, J. Ihalainen, U. Rascher, and B. Logan, "Chlorophyll a fluorescence illuminates a path connecting plant molecular biology to Earth-system science," *Nature Plants*, vol. 7, pp. 998-1009, 2021, DOI: 10.1038/s41477-021-00980-4

[117] L. Wu, Y. Zhang, Z. Zhang, X. Zhang, Y. Wu, and J. M. Chen, "Deriving photosystem-level red chlorophyll fluorescence emission by combining leaf chlorophyll content and canopy far-red solar-induced fluorescence: Possibilities and challenges," *Remote Sensing of Environment*, vol. 304, pp. 114043, 2024, DOI: 10.1016/j .rse.2024.114043

[118] C. van der Tol, W. Verhoef, A. Rosema, "A model for chlorophyll fluorescence and photosynthesis at leaf scale," *Agricultural and Forest Meteorology*, vol. 149, no. 1, pp. 96-105, 2009, DOI: 10.1016/j .agrformet.2008.07.007

[119] R. Pedros, I. Moya, Y. Goulasb and S. Jacquemoud," Chlorophyll fluorescence emission spectrum inside a leaf," *Photochemical & Photobiological Sciences 7*, vol. 4, pp. 498–502, 2008, DOI: 10.1039/b719506k

[120] D. Brewster, "On the Colours of Natural Bodies," *Transactions of the Royal Society of Edinburgh*, vol. 12, no. 2, pp. 538-545, 1834, DOI: 10.1017/S0080456800031203

[121] G. Govindjee, "Sixty-three years since Kautsky: chlorophyll a fluorescence," *Australian Journal of Plant Physiology*, vol. 22, no. 2, pp. 131-160, 1995.

[122] H. Kautsky, W. Appel,and H. Amann,“ Chlorophyllfluorescenz und kohlensaureassimilation,” *Biochemische Zeitschrift*, vol. 332, pp. 277–292, 1960

[123] U. Schreiber, U. Schliwa, and W. Bilger, “Continuous recording of photochemical and non-photochemical chlorophyll fluorescence quenching with a new type of modulation fluorometer,” *Photosynthesis Research*, vol. 10, pp. 51–62, 1986, DOI: 10.1007/BF00024185

[124] S. Wieneke, A. Burkart, M.P. Cendrero-Mateo, T. Julitta, M. Rossini, A. Schickling, M. Schmidt, and U. Rascher, “Linking photosynthesis and sun-induced fluorescence at sub-daily to seasonal scales,” *Remote Sensing of Environment*, vol. 219, pp. 247-258, 2018, DOI: 10.1016/j .rse.2018.10.019

[125] Z. S. Kolber, O. Prášil, and P. G. Falkowski, “Measurements of variable chlorophyll fluorescence using fast repetition rate techniques: defining methodology and experimental protocols,” *Biochimica et Biophysica Acta (BBA) - Bioenergetic*, vol. 1367, no. 1-3 pp. 88-106, 1998, DOI: 10.1016/S0005-2728(98)00135-2

[126] Kolber, Z., Klimov, D., Ananyev, G. et al. “Measuring photosynthetic parameters at a distance: laser induced fluorescence transient (LIFT) method for remote measurements of photosynthesis in terrestrial vegetation,” *Photosynthesis Research*, vol. 84, pp.121–129,2005, DOI: 10.1007/s11120-005-5092-1

[127] A. R. Raesch, O. Muller, R. Pieruschka, and U. Rascher, “Field Observations with Laser-Induced Fluorescence Transient (LIFT) Method in Barley and Sugar Beet,” *Agriculture*, vol. 4, pp. 159-169, 2014, DOI: 10.3390/agriculture4020159

[128] O. Knopf, A. Castro, J. Bendig, R. Pude, E. Kleist, H. Poorter, U. Rascher, and O. Muller, “Field phenotyping of ten wheat cultivars under elevated CO2 shows seasonal differences in chlorophyll fluorescence, plant height and vegetation indices,” *Frontiers in Plant Science*, vol. 14, pp. 1304751, 2024, DOI: 10.3389/f pls.2023.1304751

[129] M. P. Cendrero-Mateo, S. Wieneke, A. Damm, L. Alonso, F. Pinto, J. Moreno, L. Guanter, M. Celesti, M. Rossini, N. Sabater, S. Cogliati, T. Julitta, U. Rascher, Y. Goulas, H. Aasen, J. Pacheco-Labrador, and A. M. Arthur, “Sun-Induced Chlorophyll Fluorescence III: Benchmarking Retrieval Methods and Sensor Characteristics for Proximal Sensing, ” *Remote Sensing*, vol. 11, no. 962, 2019, DOI: 10.3390/rs11080962

[130] T. Julitta, L. A. Corp, M. Rossini, A. Burkart, S. Cogliati, N. Davies, M. Hom, A. Mac Arthur, E. M. Middleton, U. Rascher, A. Schickling, and

R. Colombo, "Comparison of sun-induced chlorophyll fluorescence estimates obtained from four portable field spectroradiometers," *Remote Sensing*, vol. 8, no. 2, 2016, DOI: 10.3390/rs8020122

[131] F. Pinto, A. Damm, A. Schickling, C. Panigada, s. Cogliati, M. Müller-Linow, A. Ballvora, and U. Rascher, "Sun-induced chlorophyll fluorescence from high-resolution imaging spectroscopy data to quantify spatio-temporal patterns of photosynthetic function in crop canopies," *Plant, Cell and Environment*, vol. 39, pp. 1500–1512, 2016, DOI: 10.1111/pce.12710

[132] S. Bandopadhyay, A. Rastogi, and R. Juszcza, "Review of Top-of-Canopy Sun-Induced Fluorescence (SIF) Studies from Ground, UAV, Airborne to Spaceborne Observations," *Sensors*, vol. 20, no. 4, 2020, DOI: 10.3390/s20041144

[133] J. A. Plascyk and F. C. Gabriel, "The Fraunhofer Line Discriminator MKII-An Airborne Instrument for Precise and Standardized Ecological Luminescence Measurement," *IEEE Transactions on Instrumentation and Measurement*, vol. 24, no. 4, pp. 306-313, 1975, DOI: 10.1109/TIM.1975.4314448

[134] J. Joiner, Y. Yoshida, A. P. Vasilkov, Y. Yoshida, L. A. Corp, and E. M. Middleton, "First observations of global and seasonal terrestrial chlorophyll fluorescence from space," *Biogeosciences*, vol. 8, no. 3, pp. 637-651, 2011, DOI: 10.5194/bg-8-637-2011

[135] C. van der Tol, T. Julitta, P. Yang, N. Sabater, I. Reiter, M. Tudoroiu, D. Schuettemeyer, M. Drusch, "Retrieval of chlorophyll fluorescence from a large distance using oxygen absorption bands," *Remote Sensing of Environment*, vol. 284, pp. 113304, 2023, DOI: 10.1016/j .rse.2022.113304

[136] S. W. Maier, K. P. Günther and M. Stellmes, "Sun-induced fluorescence: a new tool for precision farming," in *American Society of Agronomy Special Publication*, vol. 66, pp. 209-222, 2003, DOI: 10.2134/ASASPECPUB66.C16

[137] L. Alonso, L. Gómez-Chova,J. Vila-Francés, J., Amorós-López, L. Guanter, J. Calpe, "Improved Fraunhofer Line Discrimination method for vegetation fluorescence Quantification," *IEEE Geoscience and Remote Sensing Letters*, vol. 5, no. 4, pp. 620–624, 2008, DOI: 10.1109/LGRS.2008.2001180

[138] S. Cogliati, M. Celeste, I. Cesana, F. Miglietta, L. Genesio, T. Julitta, D. Schuettemeyer, M. Drusch, U. Rascher, P. Jurado, and R. Colombo, "Retrieval of sun-induced fluorescence using advanced spectral fitting methods," *Remote Sensing of Environment*, vol. 169, pp. 344-357, 2015, DOI: 10.1016/j .rse.2015.08.022

[139] J. Joiner, L. Guanter, R. Lindstrot, M. Voigt, A. P. Vasilkov, E. M. Middleton, K. F. Huemmrich, Y. Yoshida, and C. Frankenberg, "Global monitoring of terrestrial chlorophyll fluorescence from moderate-spectral-resolution near-infrared satellite measurements: methodology, simulations, and application to GOME-2," *Atmospheric Measurement Techniques*, vol. 6, no. 10, pp. 2803-2823, 2013, DOI: 10.5194/amt-6-2803-2013

[140] L. Guanter, C. Bacour, A. Schneider, I. Aben, T. A. van Kempen, F. Maignan, Ch. Retscher, Ph. Köhler, Ch. Frankenberg, J. Joiner, and Y. Zhang, "The TROPOSIF global sun-induced fluorescence dataset from the Sentinel-5P TROPOMI mission," *Earth System Science Data*, vol. 13, no. 11, pp. 5423–5440, 2021, DOI: 10.5194/essd-13-5423-2021

[141] M. Rossini, M. Meroni, M. Celesti, S. Cogliati, T. Julitta, C. Panigada, U. Rascher, C. Van der Tol, and R. Colombo, "Analysis of Red and Far-Red Sun-Induced Chlorophyll Fluorescence and Their Ratio in Different Canopies Based on Observed and Modeled Data," *Remote Sensing*, vol. 8, no. 5, pp. 412, 2016, DOI: 10.3390/rs8050412

[142] E. J. Milton, M. E. Schaepman, K. Anderson, M. Kneubühler, and N. Fox, "Progress in field spectroscopy," *Remote Sensing of Environment*, vol. 113, pp. S92-S109, 2009, DOI: 10.1016/j .rse.2007.08.001

[143] Y. Sun, J. Wen, L. Gu, J. Joiner, C. Y. Chang, C. van der Tol, A. Porcar-Castell, T. Magney, L. Wang, L. Hu, U. Rascher, P. Zarco-Tejada, C. B. Barrett, J. Lai, J. Han, and Z. Luo, "From remotely-sensed solar-induced chlorophyll fluorescence to ecosystem structure, function, and service: Part II—Harnessing data," *Global Change Biology*, vol. 29, pp. 2893-2925, 2023, DOI: 10.1111/gcb.16646

[144] M. Pickering, A. Cescatti, G. Duveiller, "Sun-induced fluorescence as a proxy for primary productivity across vegetation types and climates," *Biogeosciences*, vol. 19, no. 20, pp. 4833-4864, 2022, DOI: 10.5194/bg-19-4833-2022

[145] B. Chen, N. C. Coops, D. Fu, H. A. Margolis, B. D. Amiro, T. A. Black, M. A. Arain, A. G. Barr, C. P.-A. Bourque, L. B. Flanagan, P. M. Lafleur, J. H. McCaughey, and S. C. Wofsy, "Characterizing spatial representativeness of flux tower eddy-covariance measurements across the Canadian Carbon Program Network using remote sensing and footprint analysis," *Remote Sensing of Environment*, vol. 124, pp. 742-755, 2012, DOI: 10.1016/j .rse.2012.06.007

[146] L. Zhao, R. Sun, J. Zhang, Z. Liu, and S. Li, "Matching Satellite Sun-Induced Chlorophyll Fluorescence to Flux Footprints Improves Its Relation-

ship with Gross Primary Productivity," *Remote Sensing*, vol. 16, no. 13, pp. 2388, 2024, DOI: 10.3390/rs16132388

[147] U. Rascher, L. Alonso, A. Burkart, C. Cilia, S. Cogliati, R. Colombo, A. Damm, M. Drusch, L. Guanter, J. Hanus, T. Hyvärinen, T. Julitta, J. Jussila, K. Kataja, P. Kokkalis, S. Kraft, T. Kraska, M. Matveeva, J. Moreno, O. Muller, C. Panigada, M. Pikl, F. Pinto, L. Prey, R. Pude, M. Rossini, A. Schickling, U. Schurr, D. Schüttemeyer, J. Verrelst, and F. Zemek, "Sun-induced fluorescence - a new probe of photosynthesis: First maps from the imaging spectrometer HyPlant," *Global Change Biology*, vol. 21, no. 12, pp. 4673-4684, 2012, DOI: 10.1111/gcb.13017

[148] B. Siegmann, L. Alonso, M. Celesti, S. Cogliati ,R. Colombo, A. Damm , S. Douglas, L. Guanter, J. Hanuš,K. Kataja, T. Kraska, M. Matveeva, Jóse Moreno 2 , O. Muller, M. Pikl, F. Pinto, J. Q Vargas , P. Rademske, F. Rodriguez-Morene, N. Sabater , A. Schickling, D. Schüttemeyer,F. Zemek, and U. Rascher, "The high-performance airborne imaging spectrometer HyPlant-from raw images to top-of-canopy reflectance and fluorescence products: Introduction of an automatized processing chain," *Remote Sensing*, vol. 11, no. 23, 2019, DOI: 10.3390/rs11232760

[149] G. Tagliabue, C. Panigada, B. Dechant, F. Baret, S. Cogliati, R. Colombo, M. Migliavacca, P. Rademske, A. Schickling, D. Schüttemeyer, J. Verrelst, U. Rascher, Y. Ryu, and M. Rossini, "Exploring the spatial relationship between airborne-derived red and far-red sun-induced fluorescence and process-based GPP estimates in a forest ecosystem," *Remote Sensing of Environment*, vol. 231, pp. 111272, 2019, DOI: 10.1016/j .rse.2019.111272

[150] N. Wang, J. Suomalainen, H. Bartholomeus, L. Kooistra, D. Masiliūnas, and J. G. P. W. Clevers, "Diurnal variation of sun-induced chlorophyll fluorescence of agricultural crops observed from a point-based spectrometer on a UAV," *International Journal of Applied Earth Observation and Geoinformation*, vol. 96, 2021, DOI: 10.1016/j.jag.2020.102276

[151] S. Cogliati, M. Rossini, T. Julitta, M. Meroni, A. Schickling, A. Burkart, F. Pinto, U. Rascher, and R. Colombo, "Continuous and long-term measurements of reflectance and sun-induced chlorophyll fluorescence by using novel automated field spectroscopy systems," *Remote Sensing of Environment*, vol. 164, pp. 270-281, 2015, DOI: 10.1016/j .rse.2015.03.027

[152] P. Yang, Ch. van der Tol, "Linking canopy scattering of far-red sun-induced chlorophyll fluorescence with reflectance," *Remote Sensing of Environment*, vol. 209, pp. 456-467, 2018, DOI: 10.1016/j .rse.2018.02.029

[153] P. J. Zarco-Tejada, A. Morales, L. Testi, and F. J. Villalobos, "Spatio-temporal patterns of chlorophyll fluorescence and physiological and structural indices acquired from hyperspectral imagery as compared with carbon fluxes measured with eddy covariance," *Remote Sensing of Environment*, vol. 133, pp. 102-115, 2013, DOI: 10.1016/j .rse.2013.02.003

[154] J. Bendig, Z. Malenovský, D. Gautam and A. Lucieer, "Solar-Induced Chlorophyll Fluorescence Measured From an Unmanned Aircraft System: Sensor Etaloning and Platform Motion Correction," *IEEE Transactions on Geoscience and Remote Sensing*, vol. 58, no. 5, pp. 3437-3444, 2020, DOI: 10.1109/TGRS.2019.2956194.rse.2017.08.029

[155] L. Guanter, Y. Zhang, M. Jung, J. Joiner, M. Voigt, J. A. Berry, C. Frankenberg, A. R. Huete, P. Zarco-Tejada, J.-E. Lee, M. S. Moran, G. Ponce-Campos, C. Beer, G. Camps-Valls, N. Buchmann, D. Gianelle, K. Klumpp, A. Cescatti, J. M. Baker, and T. J. Griffis, "Global and time-resolved monitoring of crop photosynthesis with chlorophyll fluorescence," *Proceedings of the National Academy of Sciences*, vol. 111, no. 14, pp. E1327-E1333, 2014, DOI: 10.1073/pnas.1320008111

[156] P. Yang, C. van der Tol, P. K. E. Campbell, and E. M. Middleton, "Fluorescence Correction Vegetation Index (FCVI): A physically based reflectance index to separate physiological and non-physiological information in far-red sun-induced chlorophyll fluorescence," *Remote Sensing of Environment*, vol. 240, pp. 111676, 2020, DOI: 10.1016/j .rse.2020.111676

[157] Y. Zeng, G. Badgley, B. Dechant, Y. Ryu, M. Chen, and J. A. Berry, "A practical approach for estimating the escape ratio of near-infrared solar-induced chlorophyll fluorescence," *Remote Sensing of Environment*, vol. 232, pp. 111209, 2019, DOI: 10.1016/j .rse.2019.05.028

[158] J. P. Gastellu-Etchegorry, N. Lauret, T. Yin, L. Landier, A. Kallel, Z. Malenovský, Z., A. Bitar, J.Aval, S. Benhmida, J. Qi, Gh. Medjdoub, J. Guilleux, E. Chavanon, B. Cook, D. Morton, N. Chrysoulakis, and Z. Mitraka, "DART: Recent Advances in Remote Sensing Data Modeling With Atmosphere, Polarization, and Chlorophyll Fluorescence," *IEEE Journal of Selected Topics in Applied Earth Observations and Remote Sensing*, vol. 10, no. 6, pp. 2640-2649, 2017, DOI: 10.1109/JSTARS.2017.2685528

[159] R. Shamshiri, C. Weltzien, I. Hameed, I. Yule, T. Grift, S. Balasundram, L. Pitonakova, D. Ahmad, and G. Chowdhary, "Research and development in agricultural robotics: A perspective of digital farming," *International Jour-*

nal of Agricultural and Biological Engineering, vol. 11, pp. 1-14, 2018, DOI: 10.25165/j .ijabe.20181104.4278

[160] R. Guebsi, S. Mami, and K. Chokmani, "Drones in Precision Agriculture: A Comprehensive Review of Applications, Technologies, and Challenges," *Drones*, vol. 8, no. 11, pp. 686, 2024, DOI: 10.3390/drones8110686

[161] P. Zambrano, F. Calderon, H. Villegas, J. Paillacho, D. Pazmiño, and M. Realpe, "UAV Remote Sensing applications and current trends in crop monitoring and diagnostics: A Systematic Literature Review," in *IEEE 13th International Conference on Pattern Recognition Systems (ICPRS)*, Guayaquil, Ecuador, pp. 1-9, 2023, DOI: 10.1109/ICPRS58416.2023.10179038

[162] R. Eskandari, M. Mahdianpari, F. Mohammadimanesh, B. Salehi, B. Brisco, and S. Homayouni, "Meta-analysis of Unmanned Aerial Vehicle (UAV) Imagery for Agro-environmental Monitoring Using Machine Learning and Statistical Models," *Remote Sensing*, vol. 12, no. 21, pp. 3511, 2020, DOI: 10.3390/rs12213511 .compag.2023.107698

[163] A. Rejeb, A. Abdollahi, K. Rejeb, and H. Treiblmaier, "Drones in agriculture: A review and bibliometric analysis," *Computers and Electronics in Agriculture*, vol. 198, pp.107017, 2022, DOI: 10.1016/j .compag.2022.107017

[164] N. Rai, Y. Zhang, B. G. Ram, L. Schumacher, R. K. Yellavajjala, S. Bajwa, X. Sun, "Applications of deep learning in precision weed management: A review," *Computers and Electronics in Agriculture*, vol. 206, 107698, 2023, DOI: 10.1016/j .compag.2023.107698

[165] A. dos Santos Ferreira, D. Matte Freitas, G. Gonçalves da Silva, H. Pistori, M. Theophilo Folhes, "Weed detection in soybean crops using ConvNets," *Computers and Electronics in Agriculture*, vol. 143, pp. 314-324, 2017, DOI: 10.1016/j .compag.2017.10.027

[166] H. Zheng, W. Li, J. Jiang, Y. Liu, T. Cheng, Y. Tian, Y. Zhu, W. Cao, Y. Zhang, X. Yao, "A Comparative Assessment of Different Modeling Algorithms for Estimating Leaf Nitrogen Content in Winter Wheat Using Multispectral Images from an Unmanned Aerial Vehicle," *Remote Sensing*, vol. 10, no. 12, pp. 2026, 2018, DOI: 10.3390/rs10122026 .ijabe.20181104.4278.

[167] G. Devi, N. Sowmiya, K. Yasoda, K. Muthulakshmi, and K. Balasubramanian, "REVIEW ON APPLICATION OF DRONES FOR CROP HEALTH MONITORING AND SPRAYING PESTICIDES AND FERTILIZER," *Journal of critical reviews*, vol. 7, no. 6, 2020, DOI: 10.31838/jcr.07.06.117

[168] S. Souvanhnakhoomman, "Review on Application of Drone in Spraying Pesticides and Fertilizers," *International Journal of Engineering Research & Technology (IJERT)*, vol. 10, no. 11, pp. 94-98, 2021, DOI: 10.17577/IJERTV10IS110034

[169] G. Yang, J. Liu, C. Zhao, Z. Li, Y. Huang, H. Yu, B. Xu, X. Yang, D. Zhu, X. Zhang, R. Zhang, H. Feng, X. Zhao, Z. Li, H. Li, and H. Yang, "Unmanned Aerial Vehicle Remote Sensing for Field-Based Crop Phenotyping: Current Status and Perspectives," *Frontiers in Plant Science*. vol. 8, 2017, DOI: 10.3389/fpls.2017.01111

[170] E. Balestrieri, P. Daponte ,L. De Vito, and F. Lamonaca, "Sensors and Measurements for Unmanned Systems: An Overview," *Sensors*, vol. 21, no. 4, pp. 1518, 2021, DOI: 10.3390/s21041518

[171] L. Li, Q. Zhang, and D. Huang, "A Review of Imaging Techniques for Plant Phenotyping," *Sensors*, vol. 14, no. 11, pp. 20078-20111, 2014, DOI: 10.3390/s141120078

[172] K. Uto, H. Seki, G. Saito, Y. Kosugi, and T. Komatsu, "Development of a Low-Cost, Lightweight Hyperspectral Imaging System Based on a Polygon Mirror and Compact Spectrometers," *IEEE Journal of Selected Topics in Applied Earth Observations and Remote Sensing*, vol. 9, no. 2, pp. 861-875, 2016, DOI: 10.1109/JSTARS.2015.2472293

[173] B. Gano, S. Bhadra, J. M. Vilbig, N. Ahmed, V. Sagan, and N. Shakoor, "Drone-based imaging sensors, techniques, and applications in plant phenotyping for crop breeding: A comprehensive review," *The Plant Phenome Journal*, vol. 7, no. 1, p. e20100, 2024, DOI: 10.1002/ppj2.20100

[174] L. Deng, Z. Mao, X. Li, Z. Hu, F. Duan, and Y. Yan, "UAV-based multispectral remote sensing for precision agriculture: A comparison between different cameras," *ISPRS Journal of Photogrammetry and Remote Sensing*, vol. 146, pp. 124-136, 2018, DOI: 10.1016/j .isprsjprs.2018.09.008

[175] L. Feng, S. Chen, C. Zhang, Y. Zhang, and Y. He, "A comprehensive review on recent applications of unmanned aerial vehicle remote sensing with various sensors for high-throughput plant phenotyping," *Computers and Electronics in Agriculture*, vol. 182, pp. 106033, 2021. DOI: 10.1016/j .compag.2021.106033

[176] J. Jiang, H. Zheng, X. Ji, T. Cheng, Y. Tian, Y. Zhu, W. Cao, R. Ehsani, and X. Yao, "Analysis and Evaluation of the Image Preprocessing Process of a Six-Band Multispectral Camera Mounted on an Unmanned Aerial Vehicle

for Winter Wheat Monitoring," *Sensors*, vol. 19, no. 3, pp. 747, 2019, DOI: 10.3390/s19030747

[177] D. O. Wasonga, A. Yaw, J. Kleemola, L. Alakukku, and P. S. A. Mäkelä, "Red-Green-Blue and Multispectral Imaging as Potential Tools for Estimating Growth and Nutritional Performance of Cassava under Deficit Irrigation and Potassium Fertigation," *Remote Sensing*, vol. 13, no. 4, pp. 598, 2021, DOI: 10.3390/rs13040598

[178] Z. Zhang, and L. Zhu, "A Review on Unmanned Aerial Vehicle Remote Sensing: Platforms, Sensors, Data Processing Methods, and Applications," *Drones*, vol. 7, no. 6, pp. 398, 2023, DOI: 10.3390/drones7060398

[179] F. Nex, and F. Remondino, "UAV for 3D mapping applications: a review," *Applied Geomatics*, vol. 6, pp. 1–15, 2014, DOI: 10.1007/s12518-013-0120-x

[180] S. Jiang, W. Jiang, and L. Wang, "Unmanned Aerial Vehicle-Based Photogrammetric 3D Mapping: A survey of techniques, applications, and challenges," *IEEE Geoscience and Remote Sensing Magazine*, vol. 10, no. 2, pp. 135-171, 2021, DOI: 10.1109/MGRS.2021.3122248

[181] M. J. Westoby, J. Brasington, N.F. Glasser, M.J. Hambrey, J.M. Reynolds, "Structure-from-Motion' photogrammetry: A low-cost, effective tool for geoscience applications," *Geomorphology*, vol. 179, pp. 300-314, 2012, DOI: 10.1016/j .geomorph.2012.08.021

[182] S. Jeffery, F. Verheijen, M. van der Velde, and A. C. Bastos, "A quantitative review of the effects of biochar application to soils on crop productivity using meta-analysis," *Agriculture, Ecosystems & Environment*, vol. 144, no. 1, pp. 175-187, 2011, DOI: 10.1016/j.agee.2011.08.015

[183] Sh. Gul, J. K. Whalen, B. W. Thomas, V. Sachdeva, and H. Deng, "Physico-chemical properties and microbial responses in biochar-amended soils: Mechanisms and future directions," *Agriculture, Ecosystems & Environment*, vol. 206, pp. 46-59, 2015, DOI: 10.1016/j.agee.2015.03.015

[184] N. L. Panwar, A. Pawar, and B. L. Salvi, "Comprehensive review on production and utilization of biochar," *SN Applied Sciences*, vol. 1, no. 168, pp. 1-9, 2019, DOI: 10.1007/s42452-019-0172-6

[185] J. Lehmann, j. Pereira da Silva Jr., Ch. Steiner, Th. Nehls, W. Zech, and B. Glaser, "Nutrient availability and leaching in an archaeological Anthrosol and a Ferralsol of the Central Amazon basin: fertilizer, manure and charcoal amendments," *Plant and Soil*, vol. 249, pp. 343–357, 2003, DOI: 10.1023/A:1022833116184

[186] S. Adhikari, W. Timms, M. A. Parvez Mahmud, "Optimising water holding capacity and hydrophobicity of biochar for soil amendment – A review," *Science of The Total Environment*, vol. 851, pp. 158043, 2022, DOI: 10.1016/j .scitotenv.2022.158043

[187] K. C. Niraj, and M. Bhimsen, "A Review Article on The Effect of Biochar on Soil Properties," *Journal of Wastes and Biomass Management*, vol. 6, pp. 77-81, 2024, DOI: 10.26480/jwbm.02.2024.77.81

[188] Z. Abideen, H.-W. Koyro, B. Huchzermeyer, R. Ansari, F. Zulfiqar, B. Gul, "Ameliorating effects of biochar on photosynthetic efficiency and antioxidant defence of Phragmites karka under drought stress," *Plant Biology*, vol. 22, no. 2, pp. 259-266, 2020, DOI: 10.1111/plb.13054

[189] J. Lehmann, and M. Rondon, "Bio-char soil management on highly weathered soils in the humid tropics," *Biological approaches to sustainable soil systems*, pp. 517–530 2006, DOI: 10.1201/9781420017113.ch36

[190] L. A. Biederman, W. Stanley Harpole, "Biochar and its effects on plant productivity and nutrient cycling: a meta-analysis," *GCB Bioenergy*, vol. 5, pp. 202-214, 2013, DOI: 10.1111/gcbb.12037

[191] A. A. Diatta, J. H. Fike, M. L. Battaglia, J. M. Galbraith, and M. B. Baig, "Effects of biochar on soil fertility and crop productivity in arid regions: a review," *Arabian Journal of Geoscience*, vol. 13, pp. 595, 2020, DOI: 10.1007/s12517-020-05586-2

[192] P. Pariyar, K. Kumari, M. K. Jain, and P. S. Jadhao, "Evaluation of change in biochar properties derived from different feedstock and pyrolysis temperature for environmental and agricultural application,"*Science of The Total Environment*, vol. 713, pp. 136433,2020, DOI: 10.1016/j .geomorph.2012.08.021

[193] C. E. Stewart, J. Zheng, J. Botte, and M. F. Cotrufo, "Co-generated fast pyrolysis biochar mitigates green-house gas emissions and increases carbon sequestration in temperate soils," *Gcb Bioenergy*, vol. 5, no. 2, pp. 153-164, 2013, DOI: 10.1111/gcbb.12001

[194] H. Alkharabsheh, M. Seleiman,M. L. Battaglia, A. Shami, R. S. Jalal, B. A. Alhammad, KH. F. Almutairi, and A. M. Al-Saif, "Biochar and Its Broad Impacts in Soil Quality and Fertility, Nutrient Leaching and Crop Productivity: A Review," *Agronomy*, vol. 11, pp. 993, 2021, DOI: 10.3390/agronomy11050993

[195] S. Gao, Th. H. DeLuca, "Influence of Biochar on Soil Nutrient Transformations, Nutrient Leaching, and Crop Yield," *Advances in Plants & Agriculture Research*, vol. 4, pp. 00150, 2016, DOI: 10.15406/apar.2016.04.00150

[196] D. L. Gelardi, and S, J. Parikh, "Soils and beyond: Optimizing sustainability opportunities for biochar," *Sustainability*, vol. 13, no. 18, pp. 10079, 2021, DOI: 10.3390/su131810079

[197] Y. Dai, H. Zheng, Z. Jiang, and B. Xing, "Combined effects of biochar properties and soil conditions on plant growth: A meta-analysis," *Science of The Total Environment*, vol. 713, pp. 136635, 2020, DOI: 10.1016/j .scitotenv.2020.136635

[198] M. Hussain, M. Farooq, A. Nawaz, A. M. Al-Sadi, Z. M. Solaiman, S. S. Alghamdi, U. Ammara, Y. S. Ok, and K. H. M. Siddique, "Biochar for crop production: potential benefits and risks," *Journal of Soils and Sediments*, vol. 17, pp. 685–716, 2017, DOI: 10.1007/s11368-016-1360-2

[199] R. H. Dehkordi ,V. Burgeon, J. Fouche ,E. P. Gomez, J.-T. Cornelis,F. Nguyen, A. Denis, and J. Meersmans, "Using UAV Collected RGB and Multispectral Images to Evaluate Winter Wheat Performance across a Site Characterized by Century-Old Biochar Patches in Belgium," *Remote Sensing*, vol. 12, no. 15, pp. 2504, 2020, DOI: 10.3390/rs12152504

[200] R. H. Dehkordi, A. Denis, J. Fouche, V. Burgeon, J.-T. Cornelis, B. Tychon, E. P. Gomez, and J. Meersmans, "Remotely-sensed assessment of the impact of century-old biochar on chicory crop growth using high-resolution UAV-based imagery," *International Journal of Applied Earth Observation and Geoinformation*, vol. 91, pp. 102147, 2020, DOI: 10.1016/j.jag.2020.102147

[201] D. B. Goldman, "Vignette and exposure calibration and compensation," *IEEE Transactions on Pattern Analysis and Machine Intelligence*, vol. 32, no. 12, pp. 2276-2288, 2010, DOI: 10.1109/TPAMI.2010.55

[202] R. Minařík, J. Langhammer, and J. Hanuš, "Radiometric and Atmospheric Corrections of Multispectral MCA Camera for UAV Spectroscopy," *Remote Sensing*, vol. 11, no. 20, pp. 2428, 2019, DOI: 10.3390/rs11202428

[203] DJI, "P4 Multispectral Image Processing Guide," 2020.

[204] G. M. Smith, and E. Milton, " The use of the empirical line method to calibrate remotely sensed data to reflectance," *International Journal of Remote Sensing*, vol. 20, no. 13, pp. 2653-2662, 1999, DOI: 10.1080/014311699211994

[205] E. Chakhvashvili, B. Siegmann, J. Bendig, and U. Rascher, "Comparison of Reflectance Calibration Workflows for a UAV-Mounted Multi-Camera Array System," in *2021 IEEE International Geoscience and Remote Sensing Symposium (IGARSS)*, Brussels, Belgium, pp. 8225-8228, 2021, DOI: 10.1109/IGARSS47720.2021.9555143

[206] J. Cuaran and J. Leon, "Crop Monitoring using Unmanned Aerial Vehicles: A Review," *Agricultural Reviews*, vol. 42, no. 2, pp. 121-132, 2021, DOI: 10.18805/ag.R-180

[207] C. Buschmann and E. Nagel, "In vivo spectroscopy and internal optics of leaves as basis for remote sensing of vegetation," *International Journal of Remote Sensing*, vol. 14, no. 4, pp. 711-722, 1993, DOI: 10.1080/01431169308904370

[208] A. Gitelson and M. N. Merzlyak, "Spectral Reflectance Changes Associated with Autumn Senescence of Aesculus hippocastanum L. and Acer platanoides L. Leaves. Spectral Features and Relation to Chlorophyll Estimation," *Journal of Plant Physiology*, vol. 143, no. 3, pp. 286-292, 1994, DOI: 10.1016/S0176-1617(11)81633-0

[209] X. Zhang, M. A. Friedl, and C. Schaaf, "Global vegetation phenology from Moderate Resolution Imaging Spectroradiometer (MODIS): Evaluation of global patterns and comparison with in situ measurements," *Journal of Geophysical Research Atmospheres*, vol. 111, 2006, DOI: 10.1029/2006JG000217

[210] F. J. Lima-Cueto, R. Blanco-Sepúlveda, M. L. Gómez-Moreno, and F. B. Galacho-Jiménez, "Using Vegetation Indices and a UAV Imaging Platform to Quantify the Density of Vegetation Ground Cover in Olive Groves (Olea Europaea L.) in Southern Spain," *Remote Sensing*, vol. 11, no. 21, pp. 2564, 2019, DOI: 10.3390/rs11212564

[211] M. Vincini, E. Frazzi, and P. D'Alessio, "A broad-band leaf chlorophyll vegetation index at the canopy scale," *Precis Agriculture*, vol. 9, pp. 303-319, 2008, DOI: 10.1007/s11119-008-9075-z

[212] A. A. Gitelson, Y. Gritz, and M. N. Merzlyak, "Relationships between leaf chlorophyll content and spectral reflectance and algorithms for non-destructive chlorophyll assessment in higher plant leaves," *Journal of Plant Physiology*, vol. 160, no. 3, pp. 271-282, 2003, DOI: 10.1078/0176-1617-00887

[213] G. J. Fitzgerald, D. Rodriguez, L. K. Christensen, R. Belford, V. O. Sadras, and T. R. Clarke, "Spectral and thermal sensing for nitrogen and water status

in rainfed and irrigated wheat environments," *Precision Agriculture*, vol. 7, no. 4, pp. 233-248, 2006, DOI: 10.1007/s11119-006-9011-z

[214] A. Nanda, A. Mahapatra, B. Mohapatra, and A. mahapatra, "Multiple comparison test by Tukey's honestly significant difference (HSD): Do the confident level control type I error," *International Journal of Applied Mathematics and Statistics*, vol. 6, no. 1, pp. 59-65, 2021, DOI: 10.22271/maths.2021.v6.i1a.636

[215] J. Cohen, *Statistical Power Analysis for the Behavioral Sciences*, 2nd ed. New York: Routledge Academic, 1988.

[216] Z. Ni, Z. Liu, ZL. Li, F. Nerry, H. Huo, R. Sun, P. Yang, and W. Zhang, "Investigation of atmospheric effects on retrieval of sun-induced fluorescence using hyperspectral imagery," *Sensors*, vol. 16, no. 4, pp. 480, 2016, DOI: 10.3390/s16040480

[217] J. Bendig, D. Gautam, Z. Malenovský, and A. Lucieer, "Influence of Cosine Corrector and Uas Platform Dynamics on Airborne Spectral Irradiance Measurements," in *2018 IEEE International Geoscience and Remote Sensing Symposium (IGARSS)*, Valencia, Spain, pp. 8822–8825, 2018, DOI: 10.1109/IGARSS.2018.8518864

[218] J. Atherton, A. MacArthur, T. Hakala, K. Maseyk, I. Robinson, W. Liu, E. Honkavaara, and A. Porcar-Castell, "Drone measurements of solar-induced chlorophyll fluorescence acquired with a low-weight DFOV spectrometer system," in *2018 IEEE International Geoscience and Remote Sensing Symposium (IGARSS)*, Valencia, Spain, pp. 8834-8836, 2018, DOI: 10.1109/IGARSS.2018.8517474

[219] C. Camino, V. Gonzalez-Dugo, P. Hernandez, and P.J Zarco-Tejada, "Radiative transfer Vcmax estimation from hyperspectral imagery and SIF retrievals to assess photosynthetic performance in rainfed and irrigated plant phenotyping trials," *Remote Sensing of Environment*, vol. 231, 2019, DOI: 10.1016/j .rse.2019.05.005

[220] P. J. Zarco-Tejada, V. González-Dugo, and J. A. J. Berni, "Fluorescence temperature and narrow-band indices acquired from a UAV platform for water stress detection using a micro-hyperspectral imager and a thermal camera," *Remote Sensing of Environment*, vol. 117, pp. 322-337, 2012, DOI: 10.1016/j .rse.2011.10.007

[221] A. MacArthur, I. Robinson, M. Rossini, N. Davis, and K. MacDonald, "A dual-field-of-view spectrometer system for reflectance and fluorescence mea-

surements (Piccolo Doppio) and correction of etaloning," in *Fifth International Workshop on Remote Sensing of Vegetation Fluorescence*, European Space Agency, Paris, France, 2014

[222] R.Garzonio, B. Di Mauro, R. Colombo, and S. Cogliati, "Surface Reflectance and Sun-Induced Fluorescence Spectroscopy Measurements Using a Small Hyperspectral UAS," *Remote Sensing*, vol. 9, no. 5, pp. 472, 2017, DOI: 10.3390/rs9050472

[223] Ch. Y. Chang, R. Zhou, O. Kira, S. Marri, J. Skovira, L. Gu, and Y. Sun, "An Unmanned Aerial System (UAS) for concurrent measurements of solar-induced chlorophyll fluorescence and hyperspectral reflectance toward improving crop monitoring," *Agricultural and Forest Meteorology*, vol, 294, 2020, DOI: 10.1016/j .agrformet.2020.108145

[224] J. Bendig, B. Siegmann, C. Kneer, E. Chakhvashvili, J. Kraemer, S. Choza-Farias, and U. Rascher, "Imaging Spatial Heterogeneity of Solar-Induced Chlorophyll Fluorescence (SIF) with Very High Spatial Resolution Drone Imagery," in *2023 IEEE International Geoscience and Remote Sensing Symposium (IGARSS)*, Pasadena, CA, USA, pp. 4654-4657, 2023, DOI: 10.1109/igarss52108.2023.10283066

[225] C. Kneer, A. Burkart, J. Bongartz, B. Siegmann, J. Bendig, A. Jenal, and U. Rascher, "A Snapshot Imaging System for the Measurement of Solar-Induced Chlorophyll Fluorescence-Addressing the Challenges of High-Performance Spectral Imaging," *IEEE Sensors Journal*, vol. 23, no. 19, pp. 23255-23269, 2023, DOI: 10.1109/JSEN.2023.3297054

[226] T. Julitta, A. Burkart, M. Rossini, A. Schickling, R. Colombo, R. Rascher, S. Cogliati, and M. Migliavacca, "FloX: a system for automatic long-term measurements of top of canopy sun induced chlorophyll fluorescence," in *FLEX 2017 Workshop*, ESA-ESRIN, Frascati, Italy, 2017

[227] P. K. Campbell, K. F. Huemmrich, E. M. Middleton, L. A. Ward, T. Julitta, C. S. Daughtry, A. Burkart, A. L. Russ, and W. P. Kustas, "Diurnal and seasonal variations in chlorophyll fluorescence associated with photosynthesis at leaf and canopy scales," *Remote Sensing*, vol. 11, no.5, pp.488, 2019, DOI: 10.3390/rs11050488

[228] J. Krämer, B. Siegmann, Th. Kraska, O. Muller, and U. Rascher, "The potential of spatial aggregation to extract remotely sensed sun-induced fluorescence (SIF) of small-sized experimental plots for applications in crop phenotyping," *International Journal of Applied Earth Observation and Geoinformation*, vol. 104, 2021, DOI: 10.1016/j.jag.2021.102565

[229] J. Krämer, B. Siegmann, A. O. Castro, O. Muller, R. Pude, Th. Döring, and U. Rascher, "Downscaling the full-spectrum solar-induced fluorescence emission signal of a mixed crop canopy to the photosystem level using the hybrid approach," Manuscript submitted to *Remote Sensing of Environment*, 2024.

[230] H. Peng , M.P Cendrero-Mateo, J. Bendig , B. Siegmann , K. Acebron ,C. Kneer, K. Kataja, O. Muller, and U. Rascher, "HyScreen: A Ground-Based Imaging System for High-Resolution Red and Far-Red Solar-Induced Chlorophyll Fluorescence," *Sensors*, vol. 22, no. 3, pp. 9443, 2022, DOI: 10.3390/s22239443

[231] D. G. Lowe, "Distinctive image features from scale-invariant keypoints," *International journal of computer vision*, vol. 60, no. 2, pp. 91-110, 2004, DOI: 10.1023/B: VISI.0000029664.99615.94

[232] H. Bay, E. Andreas, T. Tinne, and V. G. Luc, "Speeded-up robust features (SURF)," *Computer vision and image understanding*, vol. 110, no. 3, pp. 346-359, June. 2008, DOI: 10.1016/j .cviu.2007.09.014

[233] M. A. Fischler, and R. C. Bolles, " Random sample consensus: a paradigm for model fitting with applications to image analysis and automated cartography," *Communications of the ACM*, vol. 24, no. 6, pp. 381–395, 1981, DOI: 10.1145/358669.358692

[234] B. Triggs, P. F. McLauchlan, R. I. Hartley, and A. W Fitzgibbon, "Bundle adjustment — a modern synthesis," in *Vision Algorithms: Theory and Practice*, B. Triggs, A. Zisserman, and R. Szeliski (.eds), Springer, vol. 1883, pp. 298–372, 2000, DOI: 10.1007/3-540-44480-7 _21

[235] R. Hartley, and A. Zisserman, " Multiple View Geometry in Computer Vision (2nd ed)," Cambridge University Press, 2004, DOI: 10.1017/CBO9780511811685

[236] A. Elibol, N. Gracias, and R. Garcia, "Fast topology estimation for image mosaicing using adaptive information thresholding," *Robotics and Autonomous Systems*, vol. 61, no. 2, pp. 125–136, 2013, DOI: 10.1016/j.robot.2012.10.010

[237] Sh. Sommer and T. Wade, "A to Z GIS: an illustrated dictionary of geographic information systems, Esri Press, 2006.

[238] A. J. De Leeuw, L. M. M. Veugen and H. T. C. Van Stokkom, "Geometric correction of remotely-sensed imagery using ground control points and or-

thogonal polynomials," *International Journal of Remote Sensing*, vol. 9, no. 10-11, pp. 1751-1759, 1988, DOI: 10.1080/01431168808954975 .

[239] M. Mefleh, P. Conte, C. Fadda, F. Giunta, A. Piga, G. Hassoun, and R. Motzo, "From ancient to old and modern durum wheat varieties: interaction among cultivar traits, management, and technological quality," *Journal of the Science of Food and Agriculture*, vol. 99, 2018, DOI: 10.1002/jsfa.9388

[240] B. Shiferaw, M. Smale, H. J. Braun, M. Reynolds, and G. Muricho, "Crops that feed the world 10. Past successes and future challenges to the role played by wheat in global food security," *Food Security*, vol. 5, no. 3, pp. 291–317, 2013, DOI: 10.1007/s12571-013-0263-y

[241] M. A. J. Parry, M. Reynolds, M. E. Salvucci, C. Raines, P. J. Andralojc, X.-G. Zhu, G. D. Price, A. G. Condon, and R. T. Furbank, "Raising yield potential of wheat. II. Increasing photosynthetic capacity and efficiency," *Journal of Experimental Botany*, vol. 62, no. 2, pp. 453-467, 2011, DOI: 10.1093/jxb/erq304

[242] E. E. Rezaei, K. Hey, C. Münter, H. Hüging, T. Gaiser, and S. Siebert, "A tale of two eras: assessing the impact of breeding programs on historical and modern German wheat cultivars under distinct management," *European Journal of Agronomy*, vol. 156, pp. 127179, 2024, DOI: 10.1016/j .eja.2024.127179

[243] J. A. Eisele and U. Kopke, "Choice of Cultivars in Organic Farming: New Criteria for Winter Wheat Ideotypes. 1: Light Conditions in Stands of Winter Wheat Affected by Morphological Features of Different Varieties," *Pflanzenbauwissenschaften*, vol. 1, no. 1, pp. 19-24, 1997, ISSN 1431-8857

[244] Y. Wang, Y. Pan, F. Zhao, and X. Li, "Changes in the lodging resistance of winter wheat from 1950s to the 2020s in Henan Province of China," *BMC Plant Biology*, vol. 23, no. 442, 2023, DOI: 10.1186/s12870-023-04452-z

[245] P. Kumar, H. S. Gill, M. Singh, K. Kaur, D. Koupal, S. Talukder, A. Bernardo, P. St. Amand, G. Bai, and S. K. Sehgal, "Characterization of flag leaf morphology identifies a major genomic region controlling flag leaf angle in the US winter wheat (Triticum aestivum L.)," *Theoretical and Applied Genetics*, vol. 137, no. 205, 2024, DOI: 10.1007/s00122-024-04496-1

[246] M. Prinz, "Der Einfluss des Messabstandes und der Pflazenarchticktur auf LIF-Messungen bei verschieden Genotypen, Master thesis , not published , examiners U. Rascher, O. Muller, 2022, Bonn University, Germany

[247] N. Xing, W. Huang, Q. Xie, Y. Shi, H. Ye, Y. Dong, M. Wu, G. Sun, and Q. Jiao, "A Transformed Triangular Vegetation Index for Estimating Winter Wheat Leaf Area Index," *Remote Sensing*, vol. 12, no. 1, pp. 16, 2020, DOI: 10.3390/rs12010016

[248] D. Haboudane, J. R. Miller, N. Tremblay, P. J. Zarco-Tejada, and L. Dextraze, "Integrated narrow-band vegetation indices for prediction of crop chlorophyll content for application to precision agriculture," *Remote Sensing of Environment*, vol. 81, no. 2-3, pp. 416-426, 2002, DOI: 10.1016/S0034-4257(02)00018-4

[249] J. M. Chen, "Evaluation of Vegetation Indices and a Modified Simple Ratio for Boreal Applications," *Canadian Journal of Remote Sensing*, vol. 22, no. 3, pp. 229-242, 1996, DOI: 10.1080/07038992.1996.10855178

[250] Z. G. Cerovic, G. Masdoumier, N. Ben Ghozlen, and G. Latouche, "A new optical leaf-clip meter for simultaneous non-destructive assessment of leaf chlorophyll and epidermal flavonoids," *Physiologia Plantarum*, vol. 146, no. 3, pp. 251-260, 2012, DOI: 10.1111/j.1399-3054.2012.01639.x

[251] A. E. Doan, "Type I and Type II Error," in *Encyclopedia of Social Measurement*, K. Kempf-Leonard (ed), Elsevier, pp. 883-888, 2005, DOI: 10.1016/B0-12-369398-5/00110-9

[252] C. M. Teng, "Data, Data, Everywhere: Statistical Issues in Data Mining," in *Handbook of the Philosophy of Science, Philosophy of Statistics*, P. S. Bandyopadhyay and M. R. Forster (.eds)), North-Holland, vol. 7, pp. 1099-1117, 2011, DOI: 10.1016/B978-0-444-51862-0.50034-4

[253] T. Sakamoto, D. Ogawa, S. Hiura, and N. Iwasaki, "Alternative Procedure to Improve the Positioning Accuracy of Orthomosaic Images Acquired with Agisoft Metashape and DJI P4 Multispectral for Crop Growth Observation," *Photogrammetric Engineering & Remote Sensing*, vol. 88, no. 5, pp. 323-332, 2022, DOI: 10.14358/PERS.21-00064R2

[254] S. F. Di Gennaro, P. Toscano, M. Gatti, S. Poni, A. Berton, and A. Matese, "Spectral Comparison of UAV-Based Hyper and Multispectral Cameras for Precision Viticulture," *Remote Sensing*, vol. 14, no. 3, pp. 449, 2022, DOI:10.3390/rs14030449

[255] T. V. D. W. da Silva, L. Gomes Pereira, and B. R. F. Oliveira, "Assessing Geometric and Radiometric Accuracy of DJI P4 MS Imagery Processed with Agisoft Metashape for Shrubland Mapping," *Remote Sensing*, vol. 16, no. 24, pp. 4633, 2024, DOI: 10.3390/rs16244633

[256] B. Buman, A. Hueni, R. Colombo, S. Cogliati, M. Celesti, T. Julitta, A. Burkart, B. Siegmann, U. Rascher, M. Drusch, and A. Damm, "Towards consistent assessments of in situ radiometric measurements for the validation of fluorescence satellite missions," *Remote Sensing of Environment*, vol. 274, pp. 112984, 2022, DOI: 10.1016/j .rse.2022.112984

[257] D. Li, H. Zheng, X. Xu, N. Lu, X. Yao, and J. Jiang, X. Wang, Y. Tian, Y. Zhu, W. Cao, and T. Cheng, "BRDF Effect on the Estimation of Canopy Chlorophyll Content in Paddy Rice from UAV-Based Hyperspectral Imagery," *2018 IEEE International Geoscience and Remote Sensing Symposium (IGARSS)*, Valencia, Spain, pp. 6464-6467, 2018, DOI: 10.1109/IGARSS.2018.8517684

[258] A. Moncholi-Estornell, M. P. Cendrero-Mateo, M. Antala, S. Cogliati, J. Moreno, and Sh. Van Wittenberghe, "Enhancing Solar-Induced Fluorescence Interpretation: Quantifying Fractional Sunlit Vegetation Cover Using Linear Spectral Unmixing," *Remote Sensing*, vol. 15, no. 17, pp. 4274, 2023, DOI: 10.3390/rs15174274